DYNAMIC GEOMECHANICAL MODELING OF THE INDUCED MICROSEISMICITY DURING HYDRAULIC FRACTURING

A Dissertation

by

ZHENHUA HE

Submitted to the Office of Graduate and Professional Studies of
Texas A&M University
in partial fulfillment of the requirements for the degree of

DOCTOR OF PHILOSOPHY

Chair of Committee,	Benchun Duan
Committee Members,	Hiroko Kitajima
	Michael Pope
	Yuefeng Sun
	Peter Valko
Head of Department,	Michael Pope

December 2018

Major Subject: Geophysics

ABSTRACT

The activation of natural fractures and associated microseismicity generation and radiation during hydraulic fracturing treatments are dynamic processes. However, most of the current hydraulic fracturing models are based on a quasi-static framework. Then, how significant are the dynamic stress perturbations during hydraulic fracturing treatments? Can they induce the activation of the horizontal bedding planes (BPs), which could be the source of some specific patterns of microseismic events? What are the characteristics and the predominant frequencies of the induced microseismic signals during hydraulic fracturing? How is the geometry (i.e., orientation and length) of the induced microseismic clouds correlated with that of the hydraulic fracture (HF)? We apply a dynamic finite element geomechanics method to address these important questions.

We compare the dynamic and static stress perturbations and find the dynamic stress perturbations could cause more instability around a propagating HF. BPs could be more easily activated when the HF crosses them by a short distance compared with when the HF approaches them but is still a short distance away. Fracturing fluid penetration into BPs could weaken the BPs and facilitate the activation. The rupture propagates bilaterally along the BPs at different speeds. The study on the induced microseismicity during hydraulic fracturing in a fractured reservoir indicates that rupture patterns along the natural fractures (NFs) affect the signal spectrum. The spectrum could either have multiple predominant frequencies or be relatively flat over the investigated frequency range. Injection rate doesn’t affect the predominant frequencies obviously. A higher Young’s modulus could shift the predominant frequency higher. The correlation between the geometry of the hydraulic fracture and the induced microseismic cloud

depends on the inclination of the NFs with respect to the maximum horizontal principal stress direction. When the inclination is either high or low, not so many MS events would be generated, and they are close to the HF but quite asymmetric about the HF. The MS cloud has small discrepancy with the HF in length but large discrepancy in strike. It is the opposite when the NF inclination is nearly optimal.

DEDICATION

To my God for the unconditional love, salvation and guide to me.

ACKNOWLEDGEMENTS

First, I would like to thank my advisor and committee chair, Dr. Benchun Duan. He is the best advisor ever! And he is also my dear brother. My bachelor and master's degrees are both in petroleum engineering, and I have no background in geophysics when I started this research. Dr. Duan is patient and encourages me to study some fundamental courses such as Introduction to Earthquake Seismology, Geomechanics and Finite Element Method in Geophysics, which help a lot in this dissertation. He spent a lot of time talking with me about my research and guiding me in the right direction. This dissertation would not have been possible without his continuous help and unreserved knowledge sharing.

Second, I would like to thank my committee members, Dr. Hiroko Kitajima, Dr. Michael Pope, Dr. Yuefeng Sun, and Dr. Peter Valko, for their guidance and support throughout the course of this research.

Thanks also go to my friends and colleagues and the department faculty and staff for making my time at Texas A&M University a great experience and to the Crisman Institute and the Berg Hughes Center for their financial support during my PhD study.

Finally, thanks to my mother and father, my wife and son for their love and encouragement.

CONTRIBUTORS AND FUNDING SOURCES

This work was supported by a dissertation committee consisting of Dr. Benchun Duan, Dr. Hiroko Kitajima, Dr. Michael Pope and Dr. Yuefeng Sun of the Department of Geology and Geophysics and Dr. Peter Valko of the Department of Petroleum Engineering.

This research is based on our in-house finite element geomechanics code-EQdyna. The work conducted for the dissertation including but not limited to setting up and running models, analyzing results and writing manuscripts was completed by the student.

This graduate study was supported by the Chevron Graduate Fellowship, the Geology and Geophysics Fellowship, and the Crisman and Berg-Hughes Research Assistantship.

NOMENCLATURE

BP	Bedding Plane
FEM	Finite Element Method
ff	Failure Factor
HF	Hydraulic Fracture
MS	Microseismic
NF	Natural Fracture
OIS	Optimal Inclination Slope
PCA	Principal Component Analysis (Algorithm)
WP	Weak Plane
$\boldsymbol{\sigma}$	Stress tensor
$\boldsymbol{b}$	Body force vector
$\dot{\boldsymbol{v}}$	Acceleration
$\mathbf{M}$	Mass matrix
$\mathbf{C}$	Viscous damping matrix
$\mathbf{K}$	Stiffness matrix
$\mathbf{F}$	Vector of applied forces
$\mathbf{u}$	Displacement vector
$\mathbf{v}$	Velocity vector
$\mathbf{a}$	Acceleration vector
i	Injection rate
E	Young’s modulus

E'	Plane strain modulus
v	Poisson ratio
η	Fluid viscosity
h_f	Fracture height.
τ_c	Shear strength
τ	Shear traction
$\boldsymbol{\tau}$	Shear traction vector
$\dot{s}$	Slip velocity magnitude
$\dot{\boldsymbol{s}}$	Slip velocity vector
μ	Frictional coefficient
μ_s	Static frictional coefficient
μ_d	Dynamic frictional coefficient
l	Slip distance
d_0	Critical slip distance
σ_n	Normal stress
p	Pore pressure
c	Cohesion
T	Rock tensile strength
U_N	Relative displacement in the normal direction
B	Skempton coefficient
$\Delta\sigma_{xx}(\mathrm{t})$	Time-dependent normal stress components change in x-direction
$\Delta\sigma_{yy}(\mathrm{t})$	Time-dependent normal stress components change in y-direction

$\Delta\sigma_{zz}$(t)	Time-dependent normal stress components change in z-direction
ρ	Density
V_p	P wave velocity
V_s	S wave velocity
e_{ij}	Strains
λ, μ	Lame constants

TABLE OF CONTENTS

LIST OF FIGURES

LIST OF TABLES

Page

CHAPTER I

INTRODUCTION

Hydraulic fracturing has become a successful and widely used well stimulation method in the petroleum industry for several decades (Al-Muntasheri, 2014; Clark 1949; Grossman, 1951; Padgett, 1951). It can be applied for most unconventional reservoirs, and many conventional reservoirs as well (Warpinski et al. 2013). In hydraulic fracturing treatments, fracturing fluids are injected downhole under high pressure, creating fractures in reservoirs. The Perkins-Kern-Nordgren (PKN) and Kristianovich-Geertsma-deKlerk (KGD) models are widely used in petroleum industry to predict the hydraulic fracture (HF) propagation and geometry (Valko and Economides, 1995). The fractures can enhance the oil and gas fluid flow into the wellbore. In 2000, only 1% of the total gas production in the US was from shale reservoirs. However, in 2010, the percentage of shale gas in the total gas production had significantly risen to 20% (IHS CERA, 2010). Hydraulic fracturing technology makes great contributions as well as horizontal drilling (Van Der Baan et al., 2013). But the greatest problem is that we cannot really see the underground hydraulic fracturing process and the real-time and final fracture geometry (Warpinski et al., 2013). Microseismic (MS) monitoring brings us some hope.

MS monitoring started to attract great interest from the oil and gas industry over a decade ago and now is growing rapidly (Warpinski, 2009; Maxwell, 2010). It can be applied to detect the hydraulic fracturing process and estimate the fracture geometry by locating MS events. This technology has been used for a long time to monitor the underground mining (Gibowicz et al., 1994; Urbancic et al., 2000) and geothermal system stability (Häring et al., 2008). MS events are very tiny earthquakes mostly with negative moment magnitudes induced by stress changes and/or pore fluid pressure change underground (Van Der Baan et al., 2013). Most of them are caused by human activities, such as drilling, fracturing, mining, CO_2 capture and storage etc. (McGillivray, 2005; Maxwell et al., 2010; Verdon et al., 2010; Maxwell, 2011). Typical moment magnitudes of a MS event induced by hydraulic fracturing vary from -4 to -2, with some greater events reaching up to -1 (Warpinski et al. 2013). The goal of MS monitoring is to detect, locate and characterize the large-number cloud-like induced MS events (Van Der Baan et al. 2013). MS cloud formed by event locations can delineate the geometry of the fracture zone and dynamics of the fracturing process (Baig et al. 2010). There are two common acquisition techniques which are used in MS data monitoring: surface and downhole array. A typical layout for the downhole array case is shown in Figure 1.1 (Warpinski et al. 2009). The offset monitoring well is at some reasonable distance away from the treatment well. There is a limited capability of viewing/listening distance because the amplitude of the MS signals decay with distance primarily due to geometric spreading and secondarily attenuation. A receiver array is placed in the offset wellbore near the depth where the fracturing process occurs. The long-developed and tested earthquake seismology principles can be directly applied to the MS processing and strategy, so MS data processing and strategy should not be too difficult (Warpinski et al., 2009).

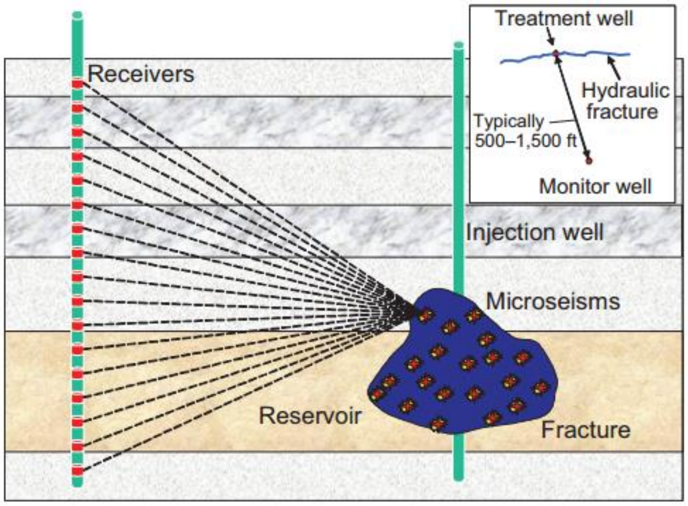

Figure 1.1 Side view of a typical microseismic monitoring layout (Reprinted from Warpinski et al., 2009).

Currently, many MS studies focus on event locations (e.g., Anikiev et al. 2013, Reys-Montes et al. 2014, Zhang et al. 2015, Jiang et al. 2016, Ry et al. 2017) and some focus on focal mechanism analysis (e.g., Li et al. 2011, Kuang et al. 2016, Kim et al. 2017). However, the source mechanisms and data interpretation of the microseismicity still remain ambiguous to some extent (Warpinski et al. 2013). Interpreting MS results and linking microseismicity to fracture behavior needs a good understanding of geomechanics during hydraulic fracturing (Warpinski et al. 2013). Meanwhile, activation of natural fractures (NFs) and microseismicity generation and radiation are dynamic processes. Therefore, dynamic geomechanical modeling is needed to accurately model hydraulic fracturing and associated processes such as microseismicity generation and radiation. However, not much effort is made on the dynamic geomechanical modeling of the induced microseismicity. In this dissertation, I focus on the research questions outlined below with our in-house dynamic finite element geomechanics code.

In Chapter II, the applied methodology in this dissertation is briefly introduced. We talk about the governing equations with the inertial terms and the finite element method (FEM) formulation. The HF propagation and the fluid net pressure follow the PKN model (Valko and Economides, 1995). The jump conditions for both shear sliding and opening motion along the planes in the models and how they are implemented by the traction-at-split-node (TSN) scheme (e.g., Day et al., 2005; Duan, 2016) are discussed. The media in the models is assumed to be undrained, fluid saturated and linearly elastic. The pore pressure is time-dependent. Its increment with time (Harris and Day, 1993) is added to the initial pore pressure to get the time-dependent pore pressure in the models.

In Chapter III, the significance of dynamic stress perturbations is investigated. We study the difference between the static and dynamic stress perturbations at a moment when a HF propagates to a certain length and how the stability around the HF is affected when dynamic stress perturbations are considered. The peak static and dynamic stress perturbations during the whole hydraulic fracturing process are also compared. In addition, we attempt to quantify the significance of the dynamic effects based on different injection rates or fracturing net pressure.

In Chapter IV, we apply our dynamic geomechanical models to study bedding-plane slip. Rutledge et al. (2013, 2015, and 2016) and some other researchers reported dip-slip or strike-slip mechanisms of some MS events induced by hydraulic fracturing, which revealed some shear planes aligned close to the principal stress direction. They proposed that these types of events could be generated by bedding-plane slip. However, a bedding-plane perpendicular to a principal direction is unlikely to be activated with simple geomechanical models (Zoback, 2010). Dynamic geomechanical models considers dynamic stress perturbations, which could cause more instability around a propagating HF and activate the bedding-planes. Different scenarios when a propagating HF meets a bedding-plane are investigated and analyzed.

In Chapter V, we study dynamic fracture interaction and the predominant frequency of the induced MS signals during hydraulic fracturing. The effect of activation of the NFs on the displacement and width profile of the HF is discussed. The microseismicity induced by different sources is investigated. We study different types of spectrums and the associated rupture patterns as well as the effect of injection rate and Young's modulus on the predominant frequencies.

In Chapter VI, the correlation between the geometry (i.e., orientation and length) of the HF and the induced MS cloud is studied. The primary goal of MS monitoring is to estimate the geometry of a HF. However, to our best knowledge, currently not much effort was made to discover the correlation. Liu et al. (2016) pointed out that it is still ambiguous if the MS cloud geometry could derive the correct or accurate HF geometry. In this chapter, we study the ratio between the MS cloud half-length and HF half-length as well as their strike difference in different scenarios with different directions of the maximum horizontal principal stress. The effect of some model parameters such as cohesion and HF length on the MS cloud also is discussed.

CHAPTER II

METHODOLOGY[1]

We use a dynamic finite element method (FEM) EQdynaFrac (Duan, 2016) to perform the numerical simulations in this research. EQdynaFrac is an extension of a dynamic FEM code EQdyna (Duan and Oglesby, 2006; Duan and Day, 2008; Duan, 2010; Duan, 2012) for rupture dynamics and seismic wave propagation. EQdyna was verified on various benchmark problems in a community-wide dynamic rupture code verification effort (Harris et al., 2009; 2011; 2018). As a FEM, EQdyna follows the standard FEM formulation for dynamic problems (e.g., Hughes, 2000). Fractures are treated as surfaces across which a discontinuity in the displacement vector is permitted. The traction-at-split-node (TSN) scheme (e.g., Day et al., 2005; Duan, 2016) is used to implement jump conditions at fractures. In the TSN scheme, a FEM node on a fracture is split into two halves, and the two halves of a split node interact through traction acting on the surface between them. Here we summarize the method below.

2.1 Governing equations and FEM formulation

The dynamic FEM solves the equations of motion

$$div(\boldsymbol{\sigma}) + \rho \boldsymbol{b} = \rho \dot{\boldsymbol{v}} \tag{2.1}$$

In the equations above, $\boldsymbol{\sigma}$ is the stress tensor, $\boldsymbol{b}$ is the body force vector, and $\dot{\boldsymbol{v}}$ is the acceleration. For the 2D models, the fixed-displacement condition is applied to the four outer model boundaries and the particle displacements and velocities in the entire model are set to be

---

[1] Reprinted with permission from Journal of Improved Oil and Gas Recovery Technology (JIOGRT), Vol 2, He, Z., and Duan, B. "Dynamic study on the fracture interaction and the predominant frequency of the induced microseismic signals during hydraulic fracturing" pp. 48-61 Copyright 2018 with permission from JIOGRT.

zero at the beginning of a simulation. Following the standard FEM procedure (e.g., Hughes, 2000), the governing equations (2.1) with the boundary conditions lead to a semi-discrete (time is left continuous) matrix equation

$$\boldsymbol{Ma} + \boldsymbol{Cv} + \boldsymbol{Ku} = \boldsymbol{F} \tag{2.2}$$

where **M** is the mass matrix, **C** is the viscous damping matrix, **K** is the stiffness matrix, **F** is the vector of applied forces, and **u**, **v**, **a** are the displacement, velocity and acceleration vectors, respectively. With the given initial conditions, equation (2.2) is solved by the central difference time integration method (e.g., Hughes, 2000).

2.2 The PKN model of the HF half-length and fluid net pressure

The opening and propagation of the HF in our models is the source of deformation. In this study, we do not aim to simulate the fluid flow and thus the spontaneous propagation of the HF. The HF propagation follows the PKN model (Valko and Economides, 1995), and the fluid net pressure from the model is added on the fracture surface. The formulas for the HF half-length and the fluid net pressure from the PKN model are

$$l_f(t) = \left(\frac{625}{512\pi^3}\right)^{1/5} \left(\frac{i^3 E'}{\eta h_f^4}\right)^{1/5} t^{4/5} \tag{2.3}$$

$$p_n(x,t) = \left(\frac{32\eta i}{\pi}\right)^{\frac{1}{4}} \frac{E'^{\frac{3}{4}}}{h_f} \left(l_f(t) - |x - x_0|\right)^{1/4}, for\ |x - x_0| \leq l_f(t) \tag{2.4}$$

Where i is the injection rate, $E'$is the plane strain modulus and calculated as E'=E/(1-v^2), E is the Young’s modulus, v is the Poisson ratio, η is the fluid viscosity, and $h_f$is the fracture height. Note that in all the chapters except Chapter IV, the HF propagates in the x-direction. The injection well is assumed at the point (x_0, 0) and $x_0 = 0$ meters. In Chapter IV of the bedding-plane slip study, x in the equation (2.4) should be replaced with z because the HF propagates in z-direction. The injection well is assumed at the point (0, z_0) and $z_0 = 1500$ meters.

2.3 Shear sliding along a weak plane or HF

The jump conditions when a weak plane shears (Day et al. 2005) are formulated as:

$$\tau_c - \tau \geq 0 \tag{2.5}$$

$$\tau_c \dot{\boldsymbol{s}} - \boldsymbol{\tau} \dot{s} = 0 \tag{2.6}$$

In equation (2.5), τ_c is the shear strength, and τ is the shear traction. This equation indicates the shear traction is bounded by current shear strength. τ_c is determined by Coulomb failure criterion given below. In equation (2.6), $\dot{\boldsymbol{s}}$ is the slip velocity vector, $\dot{s}$ is the slip velocity magnitude, and $\boldsymbol{\tau}$ is the shear traction vector. It shows any non-zero slip velocity $\dot{\boldsymbol{s}}$ be opposed by an anti-parallel traction $\boldsymbol{\tau}$ which has the same magnitude with τ_c.

The Coulomb failure criterion controls shear failure of the planes.

$$\tau_c = \mu(-\sigma_n - p) + c \tag{2.7}$$

In the equation above, τ_c is the shear strength, μ is the frictional coefficient, σ_n is the normal stress (negative in compression), p is the pore pressure, and c is the cohesion. When shear sliding occurs, friction coefficient μ evolves from a static value μ_s to a dynamic value μ_d over a critical slip distance d_0, following a linear slip-weakening law (e.g., Andrews, 1976) which is widely used in the earthquake community.

$$\mu(l) = \begin{cases} \mu_s - (\mu_s - \mu_d) \times \frac{l}{d_0} & when\ l \leq d_0 \\ \mu_d & when\ l > d_0 \end{cases} \tag{2.8}$$

2.4 Opening motion along a weak plane or HF

The jump conditions when a fracture or weak plane opens (Duan 2016) are formulated as:

$$\sigma_N + p \leq T \tag{2.9}$$

$$U_N \geq 0 \tag{2.10}$$

$$(\sigma_N + p - T)U_N = 0 \tag{2.11}$$

In equation (2.9), σ_N is the normal stress, p is the pore pressure, T is the rock tensile strength. Equation (2.9) indicates the criterion for a fracture opening. When the effective normal stress $(\sigma_N + p)$ reaches the rock tensile strength, the fracture or weak planes open. Friction disappears where a fracture or weak plane opens, and T disappears as well. In equation (2.10), U_N is the relative displacement between two opposite fracture or weak plane walls in the normal direction. This equation avoid interpenetration. When opening occurs, T becomes zero and U_N is greater than zero. Equation (2.11) indicates that the normal stress σ_N is equal to $-p$ when opening occurs.

2.5 Time-dependent pore pressure

The pore pressure in our models is time-dependent. The medium is assumed to be undrained, fluid saturated and linearly elastic. The pore pressure increment with time is as follows (Harris and Day, 1993)

$$\Delta \mathrm{p(t)} = -\mathrm{B}[(1+\upsilon)/3][\Delta\sigma_{yy}(\mathrm{t}) + \Delta\sigma_{xx}(\mathrm{t})] \tag{2.12}$$

Where $\Delta \mathrm{p(t)}$ is the time-dependent pore pressure change, B is the Skempton coefficient and we use 0.8 in our models, υ is the undrained Poisson ratio, and $\Delta\sigma_{yy}(\mathrm{t})$ and $\Delta\sigma_{xx}(\mathrm{t})$ are the time-dependent normal stress components changes in y- and x-directions. Please note that

$\Delta\sigma_{yy}(\mathrm{t})$ in equation (2.12) should be replaced with $\Delta\sigma_{zz}(\mathrm{t})$ in Chapter IV of bedding-plane slip study since we work in the x-z plane. This time-dependent pore pressure increment is added to the initial pore pressure to get the time-dependent pore pressure in each element. And the pore pressure at each split node on the weak planes is calculated by averaging the pore pressure of the adjacent four elements.

Our model includes a main model region in which the fractures are located and a surrounding buffer region. The buffer region is set to prevent the reflections at the model boundaries from travelling back to the main model region.

CHAPTER III

SIGNIFICANCE OF THE DYNAMIC STRESS PERTURBATIONS INDUCED BY HYDRAULIC FRACTURING[2]

3.1 Introduction

The microseismicity induced during hydraulic fracturing is a powerful tool in determining the geometry of HFs (Gutinerrez et al., 2010; Le Calvez et al., 2007; Michaud et al., 2008). The geometry of the fractures and the dynamics of the fracturing process can be delineated by the MS cloud formed by event locations (Baig et al. 2010). Mahrer et al. (1987) solved dynamic equations of motion to study the seismic wave motion during hydraulic fracturing. Numerical modeling of fracture growth considering the dynamic effects was performed (Duchkov and Stefanov 2015). Microseismicity generation and radiation during hydraulic fracturing are dynamic processes. Currently microseismicity still remains ambiguous in source mechanisms and data interpretation to some extent and interpreting MS results, linking microseismicity to fracture behavior needs a good understanding of geomechanics during hydraulic fracturing (Warpinski et al. 2013). To accurately model the induced microseismicity for the study of source mechanisms and other relevant research areas, dynamic geomechanical modeling is needed. In dynamic geomechanical models, dynamic stress perturbations are solved. Most of current hydraulic fracturing models are based on quasi-static framework (e.g., Kim et al., 2015; Rodriguez et al., 2016). Static stress perturbations are solved in quasi-static models. Our objective in this chapter is not to investigate the source mechanisms of the induced

---

[2] Reprinted with permission from Journal of Petroleum Science and Engineering, He, Z., and Duan, B. “Significance of the dynamic stress perturbations induced by hydraulic fracturing”, doi: https://doi.org/10.1016/j.petrol.2018.11.019. Copyright 2018 with permission from ELSEVIER.

microseismicity but to investigate the difference between static and dynamic stress perturbations exerted by hydraulic fracturing. Therefore, we do not include any NF networks in the models but only one dynamically propagating HF. In addition, we aim to quantify the significance of the dynamic effect.

For HF propagation, the fracturing net pressure is an important controlling factor. For a specific reservoir with certain rock mechanical properties, higher fracturing net pressure could cause larger dynamic effects. We find that the fracturing net pressure varies a lot in hydraulic fracturing treatments. The net pressures in two different wells in the Eagle Ford shale are 206 psi (i.e., 1.4 MPa), and 232 psi (i.e., 1.6 MPa), respectively (Bazan 2011). Cramer (1992) showed the net pressure in a Dunn County well in the Bakken shale is around 400 psi (i.e., 2.7 MPa). The net pressures of the three stages of a well in the Barnett Shale are between 1000-2000psi (1000 psi ≈ 6.9 MPa) (Puyang 2012). In the Marcellus shale, the net pressure of two wells drilled in Morgan, WV is around 500 psi (i.e., 3.5 MPa). However, the net pressure of other Marcellus wells in three areas of the Appalachian basin taking into account the dynamic state of a fracturing treatment could be up to several thousand psi (Gottschling 2010). Therefore, the fracturing net pressure could vary a lot in different reservoirs from very low to very high, even in the different wells of the same reservoir. Different net pressure could cause different levels of dynamic effects. In our models, the propagation of the HF and the net pressure along the HF follows the widely used PKN model (Valko and Economides, 1995), and the net pressure is related to the injection rate, which is an important parameter in hydraulic fracturing treatments. The net pressure increases with the injection rate when the other parameters remain unchanged. Therefore, the injection rate in our models is used as an indicator of the net pressure. Warpinski et al. (2013) showed the stresses perturbations along the distance normal to a HF wall and away from the tip, by using the analytical solutions of Green and Sneddon (1950). These analytical solutions are for quasi-static problems. In this chapter, we first study the distribution of the static and dynamic stress perturbations around a propagating HF when it propagates to a certain half-length. Second, the peak static and dynamic stress perturbations around the HF during the whole hydraulic fracturing process are compared. Lastly, the effect of injection rates on the static and dynamic stress perturbations is investigated and the induced largest peak static and dynamic stress perturbations are used for illustration.

3.2 Model

The model parameters in this study are listed in Table 3.1 and they are based on the Cotton Valley unconventional tight-sand gas reservoir at a depth around 1500 meters. With the hydraulic fracturing parameters in Table 3.1, the fluid net pressure at the wellbore when the facture propagates to about 200 feet (i.e., 61 meters, and total fracture length is 400 feet) is around 1000 psi (i.e., 6.9 MPa).

Table 3.1 Base model parameters

Parameters	Values
Density ρ (kg/m^3)	2650
Young's modulus E (GPa)	41.2
Poisson's ratio ν	0.23
P wave velocity V_p (m/s)	4300
S wave velocity V_s (m/s)	2500
Critical slip distance d_0 (m)	0.001
Cohesion c_o (MPa)	0.1
Skempton's coefficient B	0.8
Tensile strength T (MPa)	1
Initial σ_{xx} (MPa)	40
Initial σ_{yy} (MPa)	33
Initial σ_{xy} (MPa)	0
Initial pore pressure p (MPa)	15
Injection fluid viscosity η (Pa · s)	0.22
HF height h_f (m)	30.5
Injection rate i (m^3/s)	0.12

3.3 Results and Analysis

Because our models are based on a dynamic framework, it needs to be confirmed that the model system reaches static equilibrium when we investigate the static stress perturbations. When the HF propagates to a certain length (e.g., 50 meters), the fluid pressure along the fracture would remain for a short period of time to allow the generated seismic waves to propagate away. The velocity history map of a particle (i.e., a receiver located at the lower left corner of the main model region) in our model region is plotted to check if the model system reaches static equilibrium when the HF propagates to the length (e.g., 50 meters). If the particle velocity stabilizes around zero, the system is considered to be in static equilibrium. Figure 3.1 shows the velocity history plot of a particle in the model region. We can see the model system reaches static equilibrium when the HF propagates to the length (e.g., 50 meters) after about 70-second simulation.

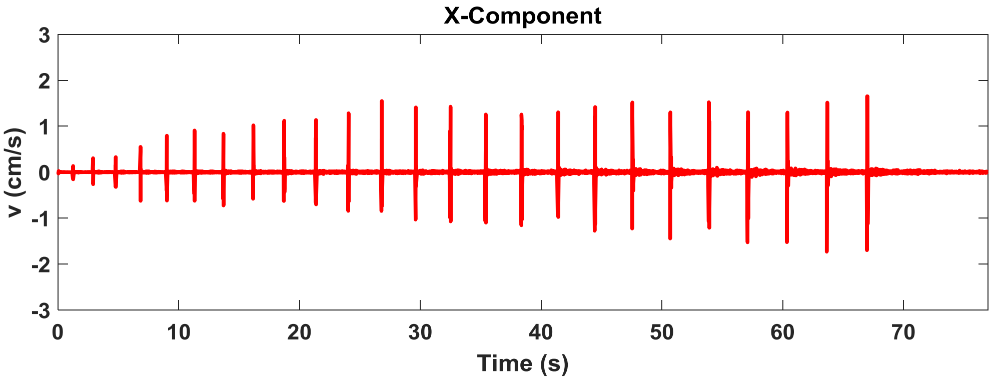

Figure 3.1 The particle velocity history at a receiver in the main model region, indicating static equilibrium is reached after about 70-second simulation.

When the generated seismic wave dies out and the model system reaches static equilibrium, the static stress perturbations around the HF when it propagates to 50 meters is plotted as shown in Figure 3.2. The directions of the maximum principal stress σ_{max} and minimum principal stress σ_{min} are aligned with x- and y- directions, respectively. From the two plots in the top panel, we can conclude that the compressive stress perturbations are the largest around the HF wall and decay along the distance normal to the HF, which is consistent with that reported by Warpinski et al. (2013). The most tensile stress perturbations occur around the HF tips. The stress perturbations exerted by the HF have more significant impact in the σ_{yy} component than in the σ_{xx} component. That is, the bright yellow oval in the top right plot is much larger than the yellow oval in the top left plot. This can be explained by Hooke's law for an isotropic elastic solid.

$$\Delta\sigma_{ij} = \lambda e_{\alpha\alpha}\delta_{ij} + 2\mu e_{ij} \tag{3.1}$$

If we expand it in unabridged notion, it becomes

$$\Delta\sigma_{xx} = \lambda\left(e_{xx} + e_{yy}\right) + 2\mu e_{xx} \tag{3.2}$$

$$\Delta\sigma_{yy} = \lambda\left(e_{xx} + e_{yy}\right) + 2\mu e_{yy} \tag{3.3}$$

$$\Delta\sigma_{xy} = 2\mu e_{xy} \tag{3.4}$$

And Poisson’s ratio is

$$\nu = {}^{e_{xx}}\!/_{e_{yy}} \tag{3.5}$$

Where $\Delta\sigma_{ij}$’s are the stress perturbations, e_{ij}’s are the strains, λ and μ are Lame constants, and ν is the Poisson ratio. Most rocks have Poisson’s ration between 0.1 and 0.4. The deformation in y-direction (i.e. e_{yy}) is larger than that in x-direction. The range of stress perturbations in y-direction is more prominent. In the bottom plot in Figure 3.2, the largest shear stress perturbations occur around the HF tips, and the sense of shear are opposite on the two sides. Similar findings are presented in Cooke et al. (2001) and Rutledge et al. (2015).

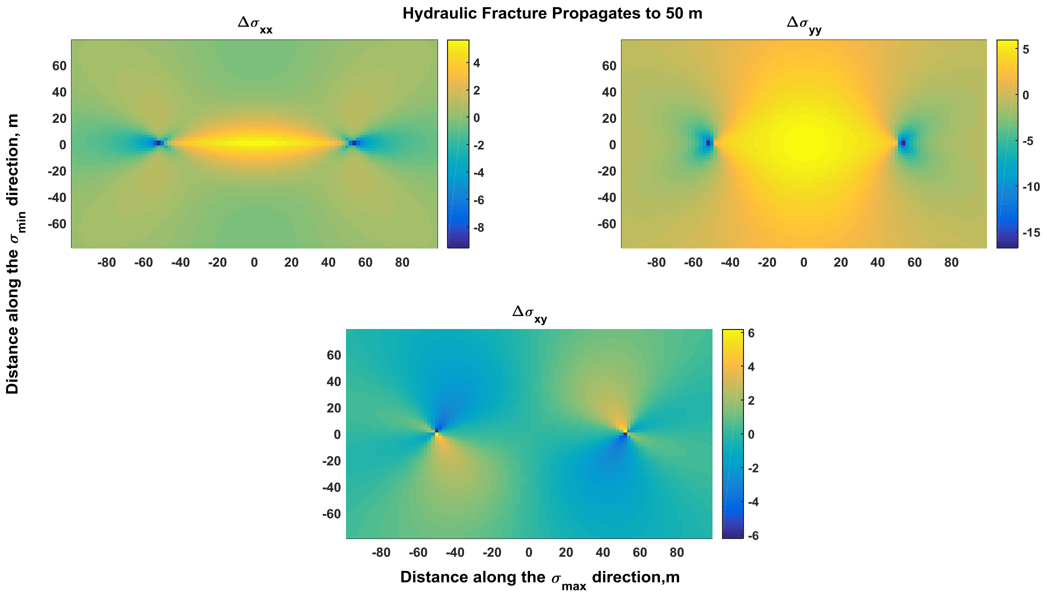

Figure 3.2 Static stress perturbations around a HF when it propagates to 50 meters.

The dynamic stress perturbations around the HF when it propagates to 50 meters are shown in Figure 3.3. Compared with Figure 3.2, we find the distributions of the stress perturbations are similar. However, we can also see some wave-like stress perturbations in Figure 3.3. When they propagate away, the model system reaches static equilibrium.

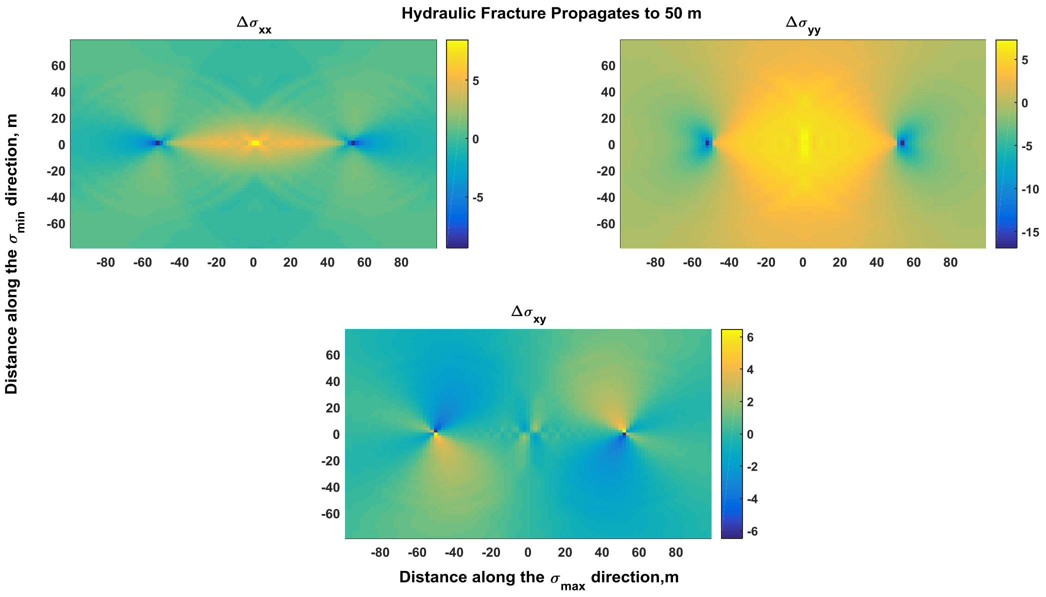

Figure 3.3 Dynamic stress perturbations around a HF when it propagates to 50 meters

Figure 3.4 compares the static and dynamic stress perturbations along the distance normal to the HF for the profile of x = 1 m. We analyze the stability around the fracture wall under dynamic and static stress conditions. In Figure 3.4, the dynamic stress perturbations are greater than the static stress perturbations in the area close to the HF. In the very close vicinity of the fracture wall, more dynamic stress perturbation is added to σ_{xx} while less is added to σ_{yy}, which would cause more instability around this area. The dynamic and static stresses (i.e., stress perturbations plus the prestresses) around the fracture wall when the HF propagates 50 m long are listed in Table 3.2. In Figure 3.5, the red and the blue Mohr circles are drawn by the static and dynamic stress tensors, respectively. The green dashed line is a Mohr-Coulomb failure line with a frictional coefficient of 0.6. We can see that the dynamic Mohr circle is closer to the failure line than the static Mohr circle. It indicates that the weak planes are more prone to fail under the dynamic stress conditions.

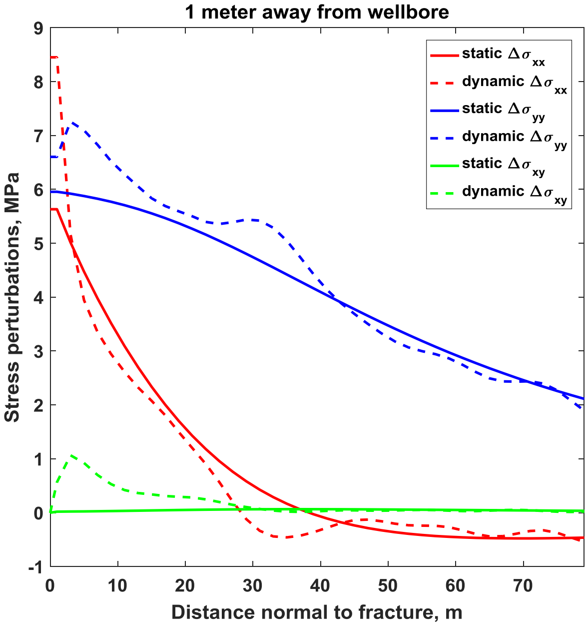

Figure 3.4 The static and dynamic stress perturbations when the HF propagates to 50 meters along the distance normal to the HF.

Table 3.2 Comparison between dynamic and static stresses for a HF with 50 m half length

	σ_{xx}, MPa	σ_{yy}, MPa	σ_{xy}, MPa
Dynamic	48.45	39.60	0.57
Static	45.63	38.95	0.02

Note: These stresses occur around the wellbore (The location coordinate is (1, 1))

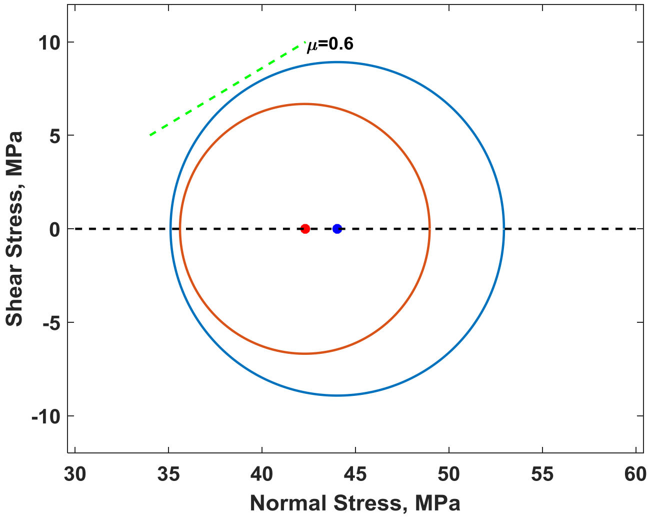

Figure 3.5 Mohr circles drawn based on the dynamic and static stress tensors. The red circle is from the static stress tensors, and the blue circle is from the dynamic stress tensors.

By comparing dynamic and static stress perturbations, we can conclude that dynamic stresses perturbations could cause more instability around the HF. They could play an important role in the study of activation of weak planes including bedding planes, NFs, etc. The activation of NFs in the reservoir could affect the estimation of the shape of the MS clouds, which is critical to infer the HF geometry.

The breaking and abrupt opening of the rock would generate seismic waves, which travel very fast in the model. The associated stress perturbations would also change dramatically in a very short time. Therefore, we study the peak static and dynamic stress perturbations during the whole hydraulic fracturing process for comparison as well.

We investigate the static stress perturbations when the HF propagates from 0 to 60 meters with a small increment. For each investigated length, the model reaches static equilibrium. We study the six different stress perturbations in different stress components: compressive and tensile σ_{xx} stress perturbations, compressive and tensile σ_{yy} stress perturbations and left-lateral and right-lateral σ_{xy} stress perturbations. Figure 3.6 shows the peak dynamic stress perturbations during the process when the HF propagates to 60 meters. The six stress perturbations during the dynamic process are shown in the subplots of Figure 3.6 respectively. In the top panel, the two subplots show the peak compressive and tensile dynamic stress perturbations in the σ_{xx} component respectively. The largest peak compressive σ_{xx} stress perturbations occur around the HF and the largest peak tensile σ_{xx} stress perturbations occur around the HF tips. The two subplots in the middle panel show the peak compressive and tensile dynamic stress perturbations in the σ_{yy} component respectively. Also, the largest peak compressive σ_{yy} stress perturbations occur around the HF and the largest peak tensile σ_{yy} stress perturbations occur around the HF tips. The two subplots in the bottom panel show the peak dynamic shear stresses of difference senses, respectively. The largest peak dynamic shear stresses occur around the HF tips. The distribution of the peak static stress perturbations (not shown) has similar patterns to that in Figure 3.6. However, we observe some large differences between the largest peak static and dynamic stress perturbations in the six different components. The values of the largest peak dynamic stress perturbations occurring during the whole hydraulic fracturing process are quite different from that of the largest peak static stress perturbations. The largest peak dynamic stress perturbations in the six subplots are about 53%, 21%, 34%, 13%, 27% and 27% higher than the corresponding largest peak static stress perturbations, respectively.

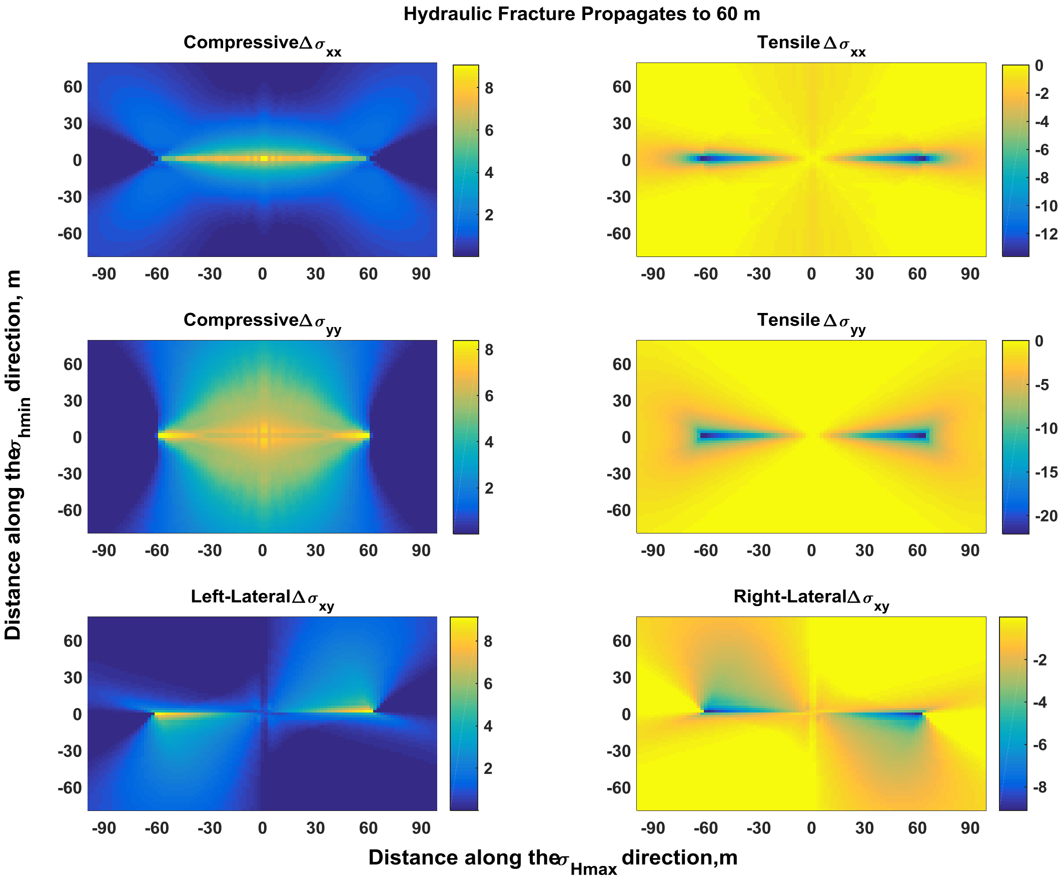

Figure 3.6 The peak dynamic stress perturbations during the process when the HF propagates to 60 meters (The stress unit is MPa).

Figure 3.7 shows the comparison of the peak static and dynamic stress perturbations along the distance normal to the fracture at different locations indicated by distance along the HF away from wellbore (Figures 3.7 (a), (b) and (c)) and from the tip of the fracture (Figure 3.7 (d)). The first 3 plots (a), (b) and (c) present the change of the peak compressive $\Delta\sigma_{xx}$ and $\Delta\sigma_{yy}$ and left-lateral $\Delta\sigma_{xy}$. We can see in the very close vicinity of the HF, peak dynamic stress perturbations in σ_{xx} and σ_{yy} components are greater than peak static stress perturbations. When the distance normal to the HF becomes larger, the difference becomes smaller. However, for the stress perturbations in σ_{xy} component, the peak dynamic shear stress perturbations are greater than the peak static shear stress perturbations in a wider area compared with the σ_{xx} component. For example, in Figure 3.7 (b), the peak dynamic shear stress perturbation is relatively larger than the peak static shear stress perturbation within the distance of about 30 meters normal to the HF. Figure 3.7 (d) shows the change of the peak tensile $\Delta\sigma_{xx}$ and $\Delta\sigma_{yy}$ and left-lateral $\Delta\sigma_{xy}$, with larger peak dynamic shear stress perturbations occurring around the HF tips during the hydraulic fracturing process, which could cause more instability.

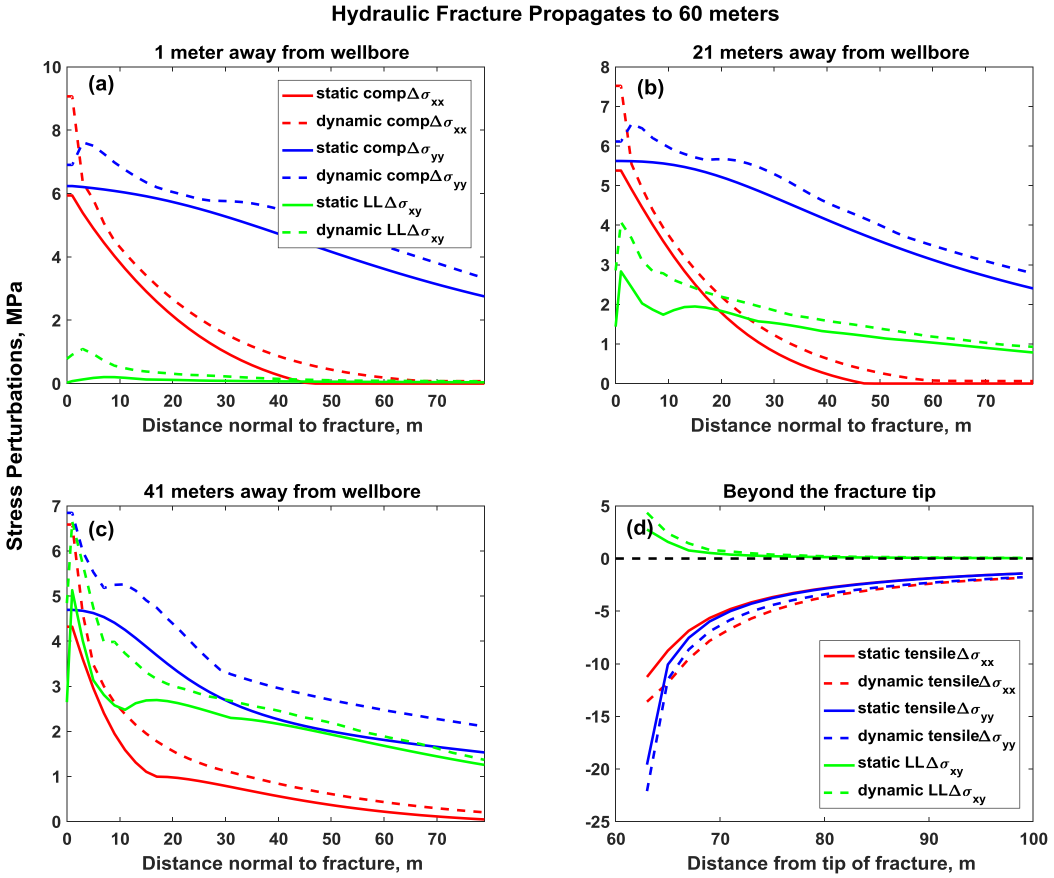

Figure 3.7 Peak stress perturbations along the distance normal to the HF (the first 3 plots) and from tip of the HF (the last plot).

3.3.1 Effect of injection rate on the static and dynamic stress perturbations

The largest peak stress perturbations in the six different components (i.e., compressive and tensile $\Delta\sigma_{xx}$, compressive and tensile $\Delta\sigma_{yy}$, and left-lateral and right lateral $\Delta\sigma_{xy}$) are measured all over the model region and during the whole hydraulic fracturing process when the injection rates are varied while other parameters remain the same as in Table 3.1. The injection rates (in Figure 3.8) are varied at 0.04, 0.08, 0.12, 0.16 m^3/s (i.e., 15, 30, 45, 60 bpm), respectively. The final HF half-lengths in all the cases are 60 meters. We can see that the absolute values of the largest peak dynamic stress perturbations are always greater than the absolute values of the largest peak static stress perturbations. The absolute values of both the largest peak dynamic and static stress perturbations increase with injection rate. Also, the absolute values of the difference between the largest peak dynamic and static stress perturbations increase with injection rates. This is because the fluid net pressure inside the HF increases with injection rates and when the injection rate gets higher, the inertial effect on the dynamic stress perturbations becomes more significant.

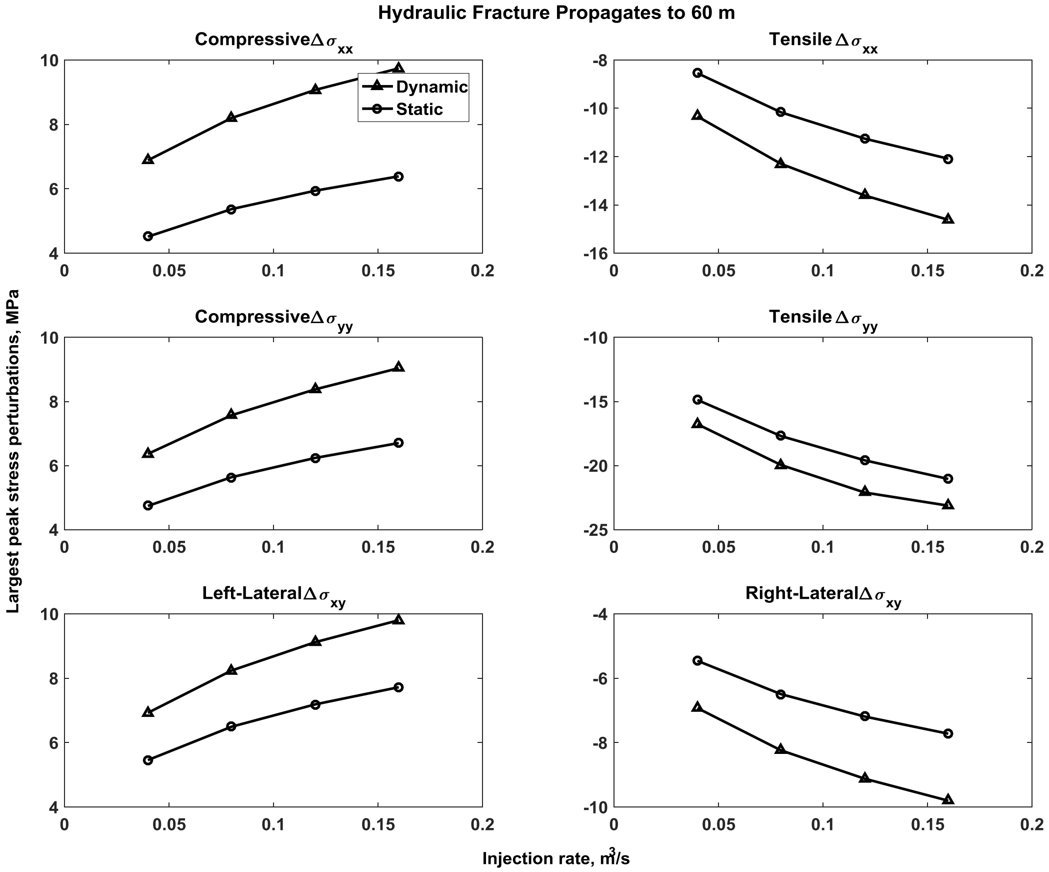

Figure 3.8 Largest peak static and dynamic stress perturbations change with injection rates.

3.4 Discussion

Dynamic stress perturbations could be significant in the studies of NF activation and microseismicity generation. We compare the static and dynamic stress perturbations when the HF propagates to a certain length. The dynamic stress perturbations could cause more instability around the HF than the static stress perturbations.

The peak dynamic stress perturbations at every location in the model will be unique during the whole hydraulic fracturing process when a HF propagates to a certain length. The peak static and dynamic stress perturbations can only be used for comparison about the values.

They are the peak values during the whole hydraulic fracturing process and not necessarily happen at the same moments. For example, the peak dynamic or static $\Delta\sigma_{xx}$, $\Delta\sigma_{yy}$ and $\Delta\sigma_{xy}$ at a location do not necessarily occur at the same time. Therefore, they cannot be viewed at same moments and used for stress analysis.

In this study, the fluid net pressure (about 6-7 MPa) in the hydraulic fracturing treatments in the Cotton Valley tight sand reservoir (i.e., injection rate of 0.12 m^3/s in Figure 3.8) is relatively high compared with the treatments in some other reservoirs. High fluid net pressure causes larger acceleration and the dynamic effects would be more prominent. This is also shown by Figure 3.8. The HF propagation and the net pressure along the HF in our models follow the PKN model. The fluid net pressure inside the HF increases with injection rates. A high injection rate indicates high fluid net pressure in the model, and the largest dynamic stress perturbations are much larger than the largest static stress perturbations. However, a low injection rate indicates low fluid net pressure in the model. The difference between the largest dynamic and static stress perturbations is much less, and so is the dynamic effect. Based on the literature study on the fracturing net pressure in the section *3.1 introduction* and the trends of the curves in Figure 3.8, we expect in some low-net-pressure hydraulic fracturing treatments, the dynamic effect could be much less significant and quasi-static modeling would be accurate enough. However, in other high-net-pressure treatments, the dynamic effect cannot be ignored and may play a significant role in activation of weak planes and induced seismicity.

3.5 Conclusions

A dynamic geomechanics finite element code is applied to study the significance of dynamic stress perturbations during hydraulic fracturing. We achieve the following conclusions:

1. The distributions of the dynamic and static stress perturbations around a HF are similar, though dynamic stress perturbations have larger amplitudes. For the normal stress components, the most compressive stress perturbations occur around the HF wall and the most tensile stress perturbations occur around the HF tips. For the shear stress components, the largest shear stress perturbations occur around the fracture tips. There are wave-like stress perturbations in the dynamic models.
2. The dynamic stress perturbations around a propagating HF could cause more instability than the static stress perturbations. The Mohr circle based on a dynamic stress tensor is closer to a failure line than that based on a static stress tensor.
3. The absolute values of the peak dynamic stress perturbations are always greater than that of the peak static stress perturbations, especially in the area close to the HF and its tips.
4. The absolute values of both the largest peak dynamic and static stress perturbations increase with injection rates and the absolute values of the difference between the largest peak dynamic and static stress perturbations also increase with injection rates as well.
5. The significance of dynamic effects could be related to the fracturing net pressure and rock mechanical properties. For a reservoir with certain rock mechanical properties, the dynamic effect could be significant and cannot be ignored at a high fracturing net pressure. However, it could be less significant when the fracturing net pressure is low and quasi-static modeling may be accurate enough.

CHAPTER IV

DYNAMIC MODELING OF BEDDING-PLANE SLIP DURING HYDRAULIC FRACTURING

4.1 Introduction

Microseismicity has been successfully applied in the petroleum industry (Gutierrez et al. 2010; Le Calvez et al. 2007; Michaud et al. 2008) and enhanced geothermal systems (i.e., EGS) (Oye et al. 2012; Gaucher, 2012). Specific patterns (dip-slip or strike-slip source mechanisms) of MS events could be generated by Bedding-Plane (BP) slip (Rutledge et al. 2013, 2015, and 2016). The located MS events from Barnett Shale and Cotton Valley tight sands which form clear horizontal bands were analyzed and these events presented the common dip-slip MS source mechanisms in fracturing stimulation. It showed one vertical nodal plane aligned with the HF and the other nodal plane oriented horizontally interpreted as a BP where slip occurs. A conceptual model is built up for interpretation in Rutledge et al. (2016). A HF touches the bedding contacts in the model. Relative displacements occur on the two sides of the bedding contacts driven by fracture opening and opposite sense of shear would be generated. The bedding-plane slip model was also proposed by Stanek and Eisner (2013) for induced MS events by hydraulic fracturing. An MS data set acquired during the hydraulic fracturing of Woodford Shale gas reservoir in the Arkoma Basin was analyzed by Stanek and Eisner (2017), who thought that the source mechanisms of the MS events were dominated by shear failure with both dip-slip and strike-slip motion and the prevailing slip mechanisms can be caused by slip along bedding planes driven by HF opening and propagation. 59 MS events induced during the hydraulic fracturing of the Marcellus Shale were used to propose a bedding-plane slip model (Tan and Engelder 2016).

A horizontal plane perpendicular to the maximum principal stress direction is unlikely to slide using a simple geomechanical model (Zoback, 2010). How weakly cohesive horizontal interfaces can slide with a geomechanical model based on some hypothesis was demonstrated by Chuprakov and Prioul (2015). Weng et al. (2018) presented a weak bedding interface may fail depending on some factors such as its strength, frictional properties, effective vertical stress at the interface and the net pressure. Roux (2016) studied the conditions required to trigger slip on horizontal planes in a Coulomb Failure Function framework and showed either low friction or significantly increased fluid pressure could achieve these. These previous studies attempting to understand bedding-plane slip assume that the involved processes are static or quasi-static (i.e., inertial effects being ignored). However, activation of bedding planes and microseismicity generation are dynamic processes, and inertial effects may be important in understanding bedding-plane slip. In this study, we use a dynamic finite element method (FEM) to quantitatively analyze the activation of BPs under different scenarios and the effects of different model parameters. We show that dynamic stress perturbations could be significant, causing large reorientations of the principal stresses and thus slip along the BPs.

4.2 Model

Figure 4.1 shows the model setup. There is one HF and two BPs in each scenario. The model parameters are listed in Table 4.1. These parameters are based on the Cotton Valley unconventional tight-sand gas reservoir at a depth around 1500 meters.

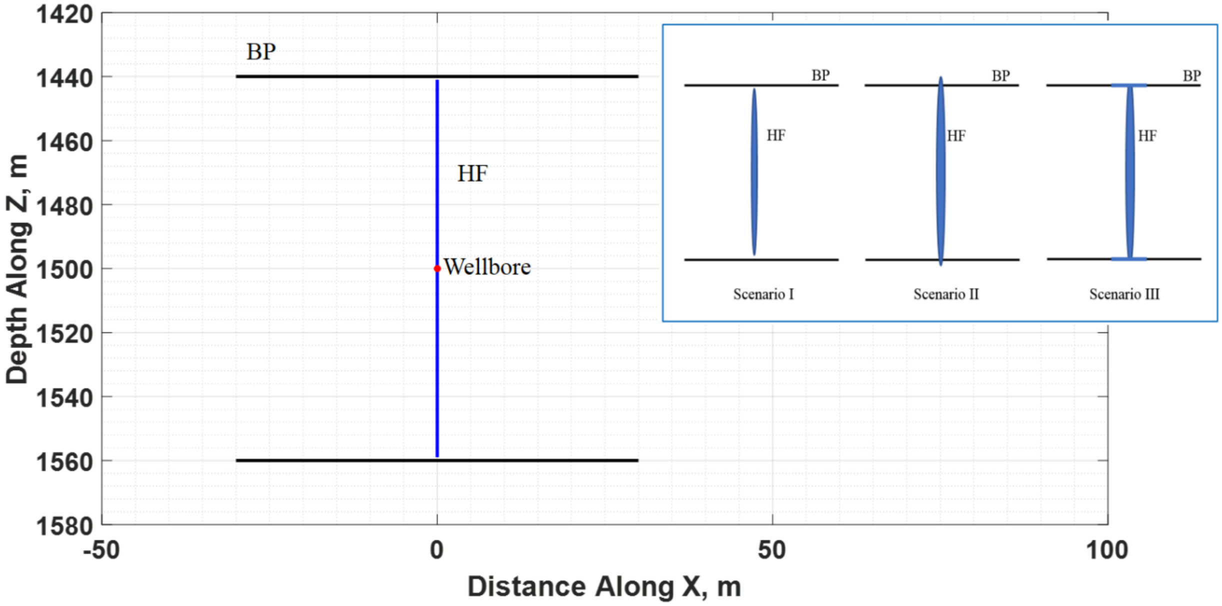

Figure 4.1 Model setup. There is one vertical HF and two symmetric horizontal BPs in the model. The inset plot shows the three different scenarios in the text.

Table 4.1 Base model parameters

Parameters	Values
Density ρ (kg/m^3)	2650
Young's modulus E (GPa)	41.2
Poisson's ratio ν	0.23
P wave velocity V_p (m/s)	4300
S wave velocity V_s (m/s)	2500
Static friction μ_s	0.25
Dynamic friction μ_d	0.15
Critical slip distance d_0 (m)	0.001
Cohesion c_o (MPa)	0.1
Skempton's coefficient B	0.8
Tensile strength T (MPa)	1
Initial σ_{zz} (MPa)	-40
Initial σ_{xx} (MPa)	-33
Initial σ_{zx} (MPa)	0
Initial pore pressure p (MPa)	15
Injection fluid viscosity η (Pa · s)	0.22
Hydraulic fracture height h_f (m)	30.5
Injection rate i (m^3/s)	0.12

4.3 Results and analysis

Hydraulic fracturing and microseismicity generation are dynamic processes and the associated dynamic stress perturbations could play a significant role in relevant studies, such as activation of weak planes (including BPs and NFs). Since BPs are typically (nearly) perpendicular to one of the principal stress axes, there is little static shear stress on them before hydraulic fracturing treatments. Shear slip must be driven by dynamic shear stress induced by propagating HFs. Therefore, the maximum dynamic shear stress on planes parallel to BPs is an important measurement about whether a BP could be activated or not and is studied in this section. The maximum dynamic shear stress herein means the σ_{zx} component, which is perpendicular to the HF, in the stress tensor and always occurs around the HF tip (An example is shown in Figure 4.2). It is obtained by comparing the dynamic shear stresses that occur during the whole hydraulic fracturing process. Because in this section we only want to study the maximum dynamic shear stress induced by HF opening and propagation without the effect of activation of BPs, the two BPs are excluded in the models in this section.

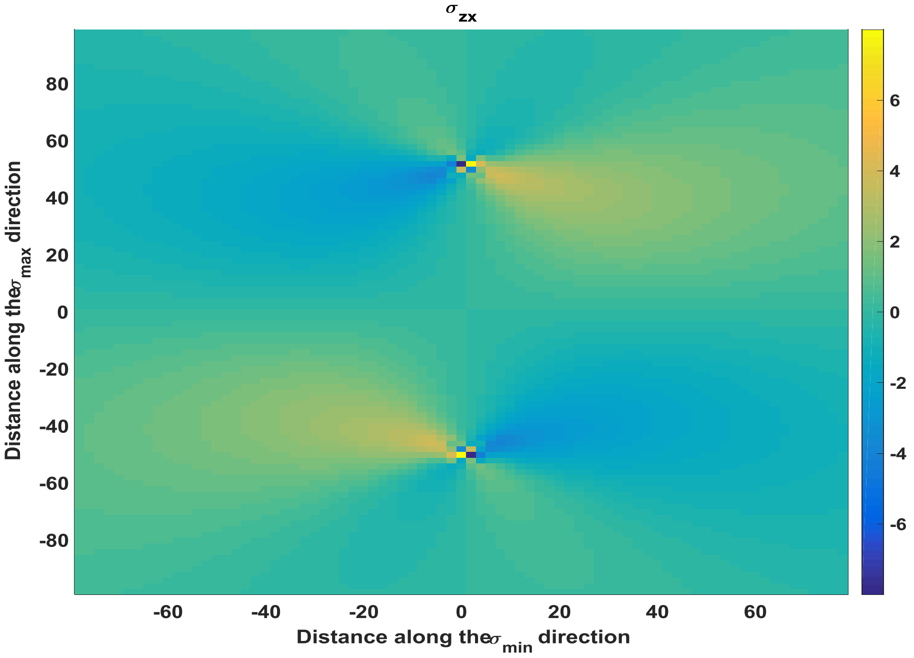

Figure 4.2 The induced dynamic shear stress distribution around a propagating HF when it propagates to a certain length (i.e., 50 meters). We can see that the maximum dynamic shear stress occurs around the HF tips.

The dynamic stress perturbations can be significant during hydraulic fracturing treatments. For example, the total dynamic stresses where the maximum dynamic shear stress occurs in the base model with the parameter values in Table 4.1 when the HF propagates to 62 meters are: σ_{zz} = -30.62 MPa, σ_{xx} = -26.33 MPa, and σ_{zx} = 9.10 MPa. The resultant principal direction reorientation is about 38^o from the original maximum principal direction (z-direction). However, the total static stresses where the maximum shear stress occurs when the HF propagates to 62 meters and the model system reaches static equilibrium (i.e., after the generated seismic waves die out) are: σ_{zz} = -32.12 MPa, σ_{xx} = -20.43 MPa, and σ_{zx} = 7.19 MPa. The resultant principal direction reorientation is about 25^o, which is less than the previous one.

The effects of HF length, reservoir rock density and injection rate on the induced maximum dynamic shear stresses are shown in Figure 4.3. The effects of these model parameters are studied separately. When the effect of one model parameter is being investigated, other model parameters remain the same as in Table 4.1. The upper left plot shows the change of maximum dynamic shear stress with HF half length. The maximum dynamic shear stresses which are used to plot the curve are obtained when the HF propagates to different lengths from 20 to 100 meters with an increment of 10 meters and increase with the HF length. Stress intensity factor increases with crack length, and shear stress is proportional to stress intensity factor (Scholz, 2002). So, shear stress increases with fracture length. Also, when HF length is greater than 80 meters, the slope of the curve decreases, suggesting a smaller increase rate of shear stress after 80 meters. The upper right plot shows how reservoir rock density affects the induced maximum dynamic shear stress. The impact of the rock density on vertical stress gradient is ignored and the vertical stress is assumed to be a constant in the investigated small depth range. σ_{xx} is also assumed to be constant within the depth range. However, the rock density affects the Young's modulus and thus the propagation of the HF and the net pressure (i.e., PKN model). The HF propagates to a same length, 62 meters in each case. The maximum dynamic shear stresses almost increase linearly with density, but not significantly (0.5 MPa incremental from 2600 kg/m^3 to 2800 kg/m^3). The bottom plot shows the effect of injection rate. The injection rate is varied while other parameters remain the same as in Table 4.1. Also, the HF propagates to a same length, 62 meters in each case. The induced maximum dynamic shear stress increases with injection rates. When the injection rate is low, the curve slope is steep. However, the slope becomes much gentler when the injection rate is high. The fluid net pressure increases with $i^{1/4}$ (i is the injection rate) for a certain half-length HF. Fluid net pressure inside the HF will affect the stress perturbations including the shear stress perturbations around the HF.

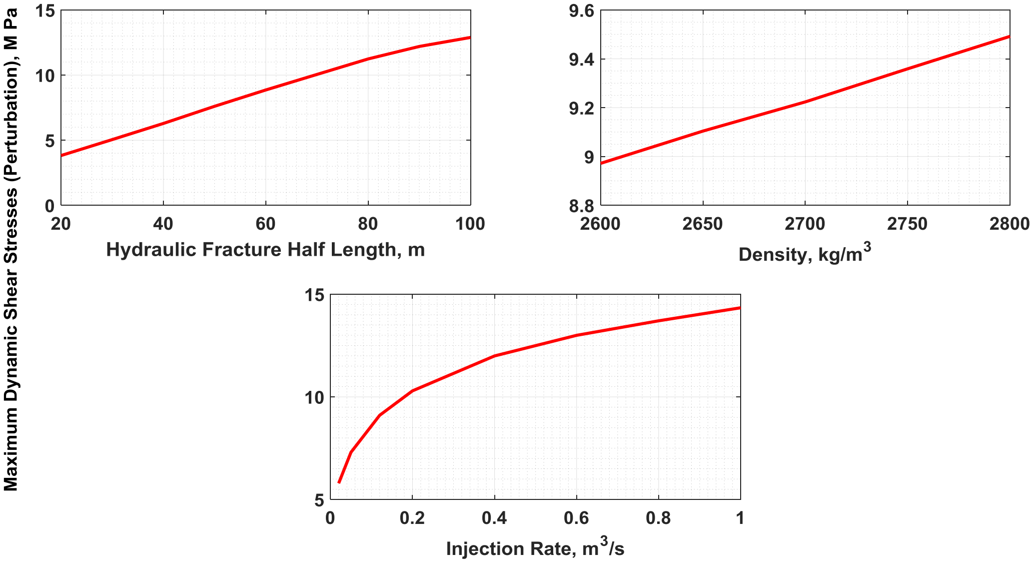

Figure 4.3 Effect of model parameters on the induced maximum dynamic shear stresses. Three subplots show the effects of HF half length, rock density and injection rate, respectively. The maximum dynamic shear stresses increase with these model parameters. However, the slopes of the curves may vary.

4.3.1 Scenario I-Activation of the BPs when a propagating HF is approaching

We performed a series of numerical experiments to investigate the activation of the BPs with different strengths (Static and dynamic frictional coefficients and cohesion are varied) because the BPs with the strength-parameters in the base model cannot be activated (as shown in the first row of Table 4.2) in this scenario. Cooke et al. (2001) also varied the strength of bedding contacts from zero strength ($\mu = 0$; $c = 0$ MPa) to study effect of the activation on fracture termination. Relatively low-strength BPs could be activated in this scenario, and Table 4.2 shows parts of the numerical experiments and the results. These results confirm that the BP can slide only when its strength is very low in this scenario. Figure 4.4 shows the profile of the shear slip and open width along the different-strength BPs. All three cases have no opening along the BPs. When μ_s=0.15, μ_d=0.10, and cohesion $c = 0.01$ MPa, no slip occurs along the BP. When μ_s=0.10, μ_d=0.05, and cohesion $c = 0.01$ MPa, part of the BP slides. The maximum slip magnitude is about 0.114 mm, and the slip length is about 4 meters on each half of a plane. Different sense of shear occurs on the two sides of the middle point. This is consistent with the findings about opposite senses of lateral displacements on the left and right of the fracture tip in Cooke et al. (2001) and Rutledge et al. (2015). When μ_s=0.0012, μ_d=0.001, and cohesion $c = 0.001$ MPa, the entire BP slides. The maximum slip magnitude is about 2.471 mm. Also, the shear slip along the BP has opposite sense. Because the strength parameters (i.e., the frictional coefficients and cohesion) are very low in the bottom plot of Figure 4.4, the induced dynamic stress perturbations can activate the entire BP. However, the local slip magnitudes around the center are very small compared to the maximum slip magnitude along the whole length so it looks like no slip occurred around the center. We remark that our work is based on 2D framework, so the ruptured area cannot be determined. Therefore, we do not compute the moment magnitudes of the events in this study. Some empirical relationships between the rupture length (including both surface and subsurface) and the moment magnitude were developed for large natural earthquakes (e.g., Wells and Coppersmith, 1994). However, a typical rupture length in microseismic studies doesn’t fall into the range (i.e., >1 km) and is much smaller.

Table 4. 2 Models with different-strength BPs

μ_s	μ_d	c_o, MPa	Activated or not
0.25	0.15	0.1	Not activated
0.25	0.15	0.01	Not activated
0.15	0.10	0.1	Not activated
0.15	0.10	0.01	Not activated
0.10	0.05	0.01	Partially activated
0.0012	0.001	0.001	Entirely activated

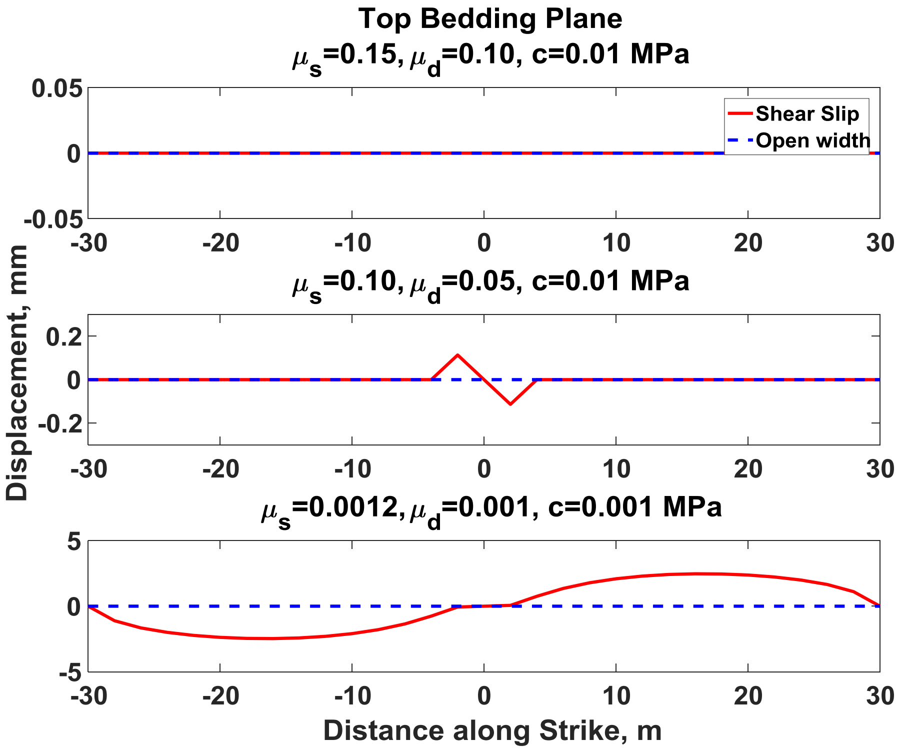

Figure 4.4 Shear slippage and open width along the top bedding plane with different strengths in three cases. There is no opening in all the cases. In the top panel, the BP is not activated. In the middle panel, the BP slides around the center. In the bottom panel, the entire BP slides (The slip magnitude is small around the center).

Figure 4.5 shows the normal stress, pore pressure, shear strength, and shear stress along the top bedding plane in the second case of Figure 4.4 at the end of the hydraulic fracturing treatment. As discussed in the *section 2.5* of *Chapter II*, the pore pressure is time-dependent, and its increment is a function of Skempton coefficient, Poisson ratio, and time-dependent normal stress components changes in x- and z-directions. From Figure 4.5, we can see both normal stress and pore pressure decrease (due to suction caused by fracture opening) on the BP close to the fracture tip. The effective normal stress remains relatively constant, and thus the shear strength. The induced shear stress makes the most contribution to the BP activation. Therefore, the activation of the BPs is mainly driven by dynamic shear stress induced by the propagating HF. Moreover, we can see the induce shear stress is anti-symmetric about the BP center. So, the slip distribution along the BP is also anti-symmetric.

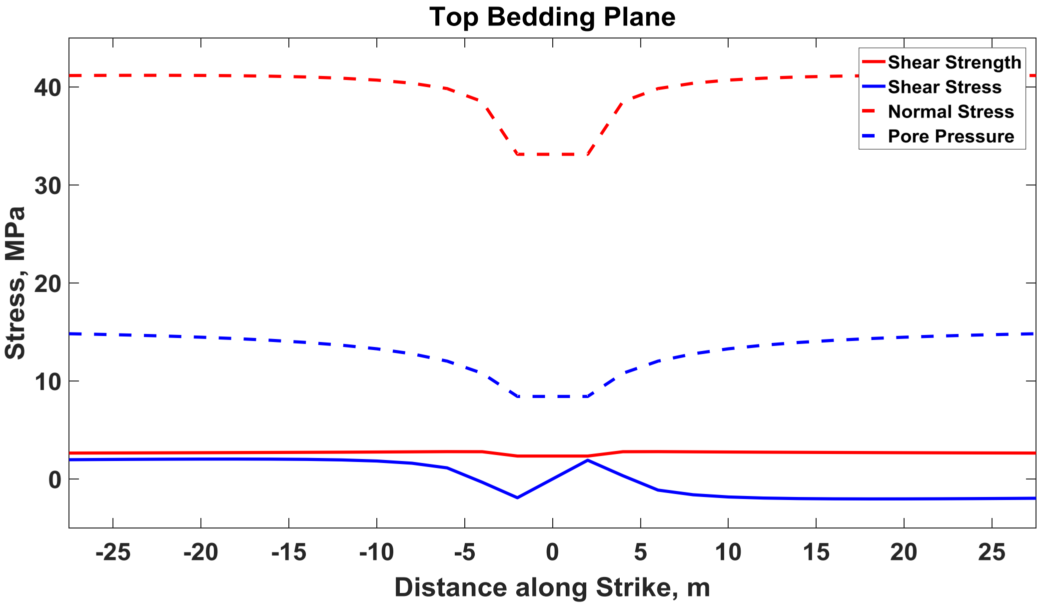

Figure 4.5 Normal stress, pore pressure, shear strength, and shear stress along the top bedding plane (in the middle panel of Figure 4.4). The HF extension line intersects the top bedding plane at 0 meter on the x-axis. The shear strength doesn't change much around the center. The main contributor for the BP activation is the induced dynamic shear stress, which is anti-symmetric about the center.

To summarize, BPs which are perpendicular to a principal stress are very difficult to be activated when a HF approaches but is still a short distance away. However, some low-strength BPs (e.g., some lubricant material or liquid on the BP contact) could be activated by the induced dynamic shear stress perturbations.

4.3.2 Scenario II-Activation of the BPs when a Propagating HF crosses them by a short distance

In this scenario, we study the activation of BPs when a propagating HF crosses them and the HF tips are beyond the BPs by a short distance (2 meters). This model uses the parameters listed in Table 4.1. The frictional parameters and cohesion are μ_s =0.25, μ_d =0.15, and c = 0.1 MPa. Figure 4.6 shows the shear slip and open width along the BPs. No opening occurs, but parts of the BPs slide. The maximum slip magnitude is about 0.380 mm and the slip-length is about 6 m. The shear slip has opposite sense to the left and right of the intersection point. What is the main contributor to the activation of the BPs? Figure 4.7 shows the snapshots of the normal stress, pore pressure, shear strength, and shear stress along the BPs at two different moments: one is when there is still some time before the rupture happens, and the other is right before the rupture happens. Comparing the two top and bottom plots of Figure 4.7, we can see that around the intersection the normal stress decreases a little while the pore pressure increases, which is caused by stress perturbations in the σ_{xx} component. Effective normal stress decreases a little. However, the shear strength doesn’t change much. The main factor to cause the activation is still the induced shear stress.

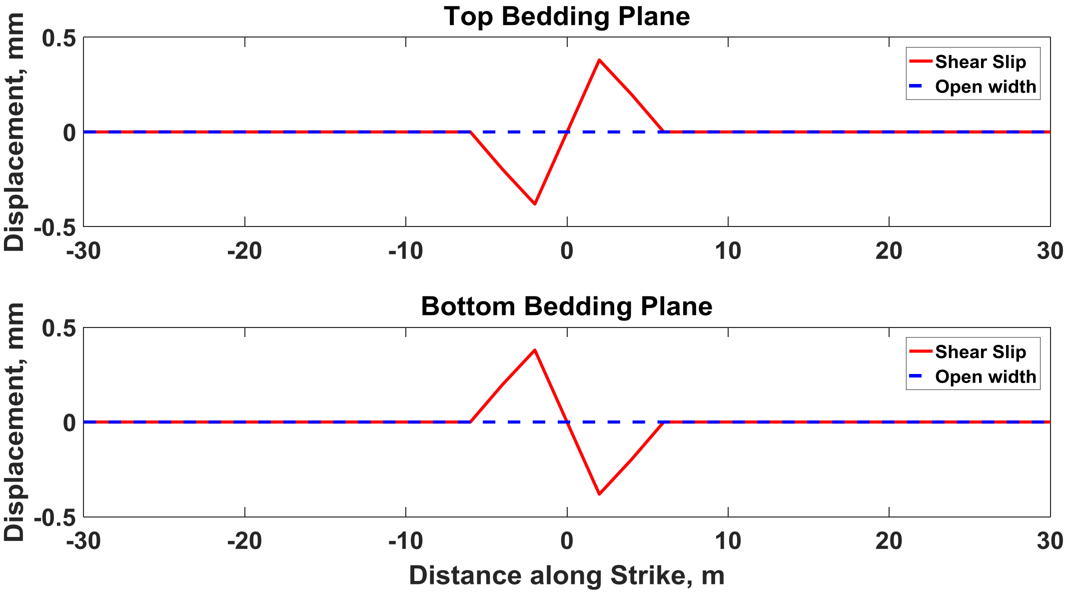

Figure 4.6 Shear slip and open width along the BPs in Scenario II. The HF crosses the BPs by a short distance (2 meters) in the Scenario II. No opening occurs along the BPs, but anti-symmetric shear slippage occurs around the center of each BP.

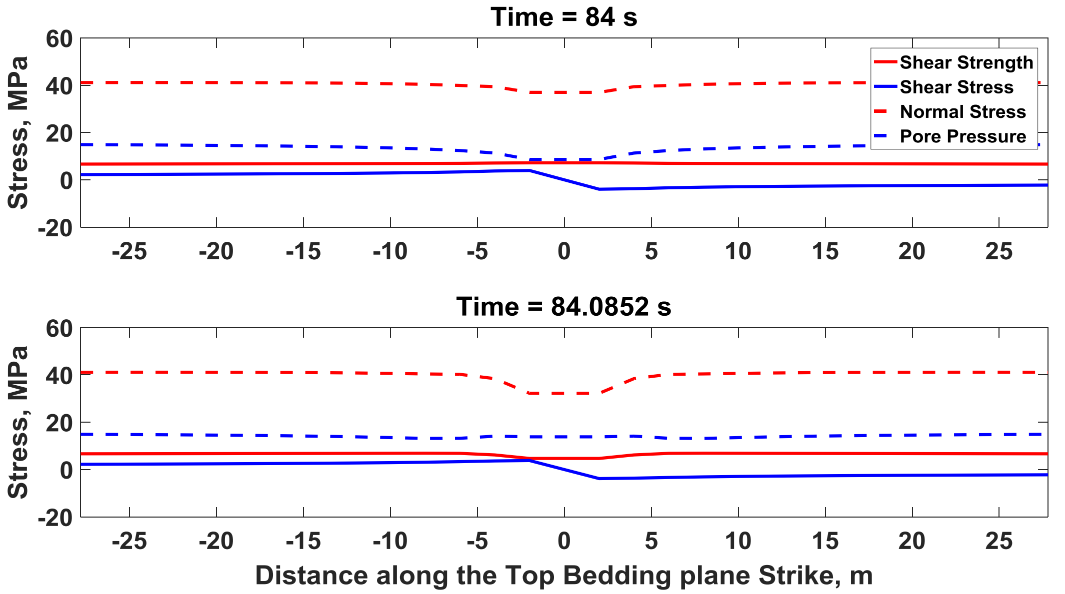

Figure 4.7 Snapshots of normal stress, pore pressure, shear strength, and shear stress along the top BP at two different moments. The first moment is when there is still some time before rupture/activation occurs, and the second moment is right before the rupture/activation occurs.

Why are the BPs with the same strength not activated in Scenario I while activated in Scenario II when the HF crosses them by a short distance? Shearing could occur as the HF rips through layer surfaces (Rutledge et al. 2015). The principal direction around the fracture tip is shown in Figure 4.8. On the left plot is a sketch of an investigation circle of 5-meter radius around the HF tip. θ is the angle measured from the HF plane, and it is positive to the left and negative to the right. The right plot shows the principal re-orientation with the angle θ. We can see from this plot the largest principal reorientation behind the fracture tip is greater than that beyond the fracture tip. Therefore, it will be easier for a BP to be activated after a HF crosses it by a short distance.

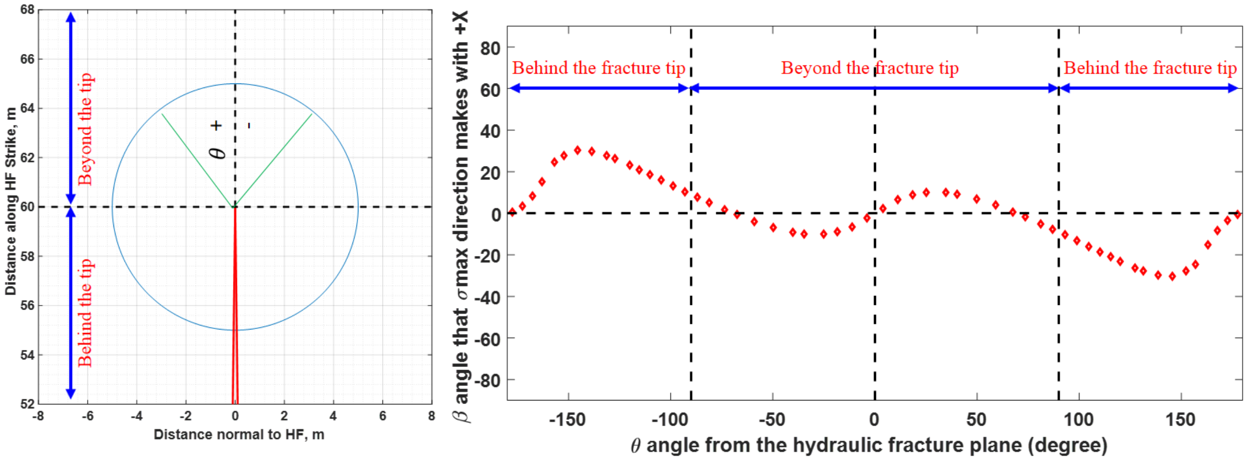

Figure 4.8 Principal direction reorientation around a propagating HF. The left subplot shows a sketch of an investigation circle of 5-meter radius around a HF tip (in red). The right subplot shows the angle of principal direction reorientation with θ angle (indicated as in left subplot). From the right subplot, we can see the largest principal reorientation behind the fracturing tip is greater than that beyond the fracture tip.

4.3.2.1 Effect of model parameters on the activation of the BPs

The effect of model parameters including cohesion, critical slip distance, maximum principal stress, and rock density on the activation of the BPs were shown in Figure 4.9. The base model parameters are listed in Table 4.1. The investigated parameter value is varied while others remain the same as in the base model to study its effect. The effect of cohesion is shown in the upper left plot. When the cohesion increases, the maximum slip magnitude and slip length decrease. When cohesion is high, it gets harder to activate a BP. We can see the stair-case decrease of the slip length because of discretization of the BPs by the finite size of elements. Moreover, we can find that the BPs cannot be activated if the cohesion is greater than 1.75 MPa. The upper right plot shows the effect of the critical slip distance. Overall, the maximum slip magnitude and the slip length decrease with the critical slip distance. The reduction is significant when the critical slip distance is small. When the critical slip distance is large, the maximum slip magnitude decreases very slowly, and the slip length remains constant. Critical slip distance indicates the distance over which the frictional coefficient evolves from a static value to a dynamic value. If it is small, a BP is relatively easy to be activated and slide. It seems when it is large, its effect on BP activation is limited. The lower left plot shows the variation of the maximum principal stress, σ_1 (i.e., vertical stress in the models) on the activation. The BPs are perpendicular to the direction of the maximum principal stress. Therefore, when σ_1 increases, the normal stress acting on the BPs increases, and it gets harder to activate the BPs. When σ_1 is too large, the BPs cannot be activated. In this study, we only test the effect of the maximum principal stress, and the minimum principal stress (horizontal principal stress) remains constant. The effect of rock density is shown in the lower right plot. Over the rock density in the range of interest, the slip length doesn't change, and the maximum slip magnitude increases.

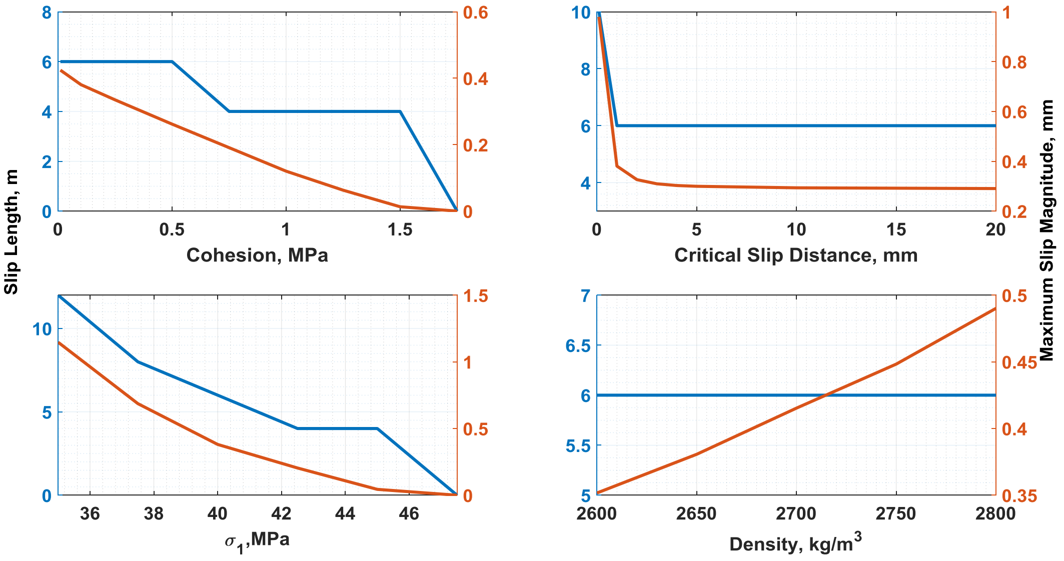

Figure 4.9 Effect of different model parameters on the activation of BPs including the slip length (blue lines) and maximum slip magnitude (red lines). The four subplots show the effect of cohesion, critical slip distance, vertical stress (acting as σ_1, the maximum principal prestress), and rock density on the BP activation, respectively.

4.3.2.2 Rupture along the BPs

We also study the rupture along the BPs. In this part, we use the model with maximum principal stress, σ_1= 35 MPa because the slip length is relatively longer (more node pairs slide) and it is better to show how ruptures propagate along the BPs. Figure 4.10 shows the slip distribution with opposite sense about the middle/intersection point. The maximum slip magnitude is about 1.147 mm and the slip-length is about 10 meters on one side. Figure 4.11 presents how rupture propagates along the BPs. For both BPs, the rupture propagates bilaterally from the center and stops at about 10-meter location on each side. The rupture speed is generally a constant of about 2300 m/s (i.e., sub-shear rupture, a little below the shear wave velocity, 2500 m/s) at the beginning and then significantly drops and becomes zero at the end.

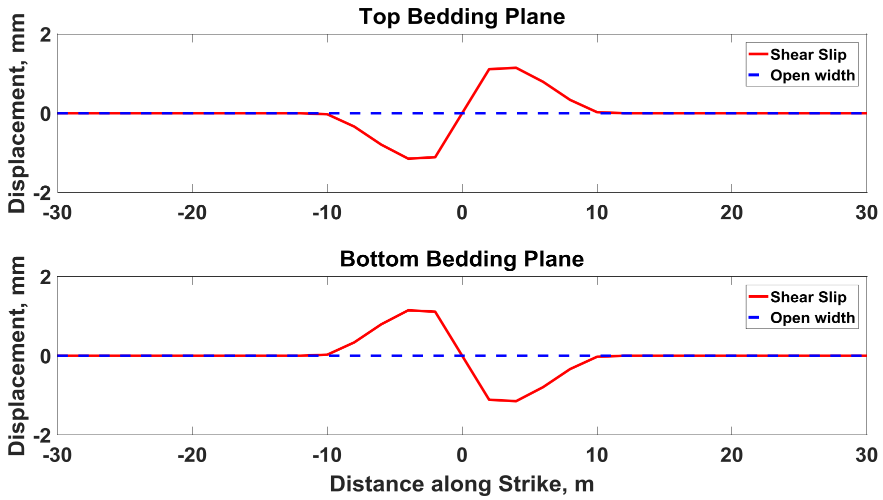

Figure 4.10 Shear slip and open width along the BPs in the case when σ_1= 35 MPa (in Figure 4.8). No opening occurs along the BPs, but anti-symmetric shear slippage occurs around the center of each BP.

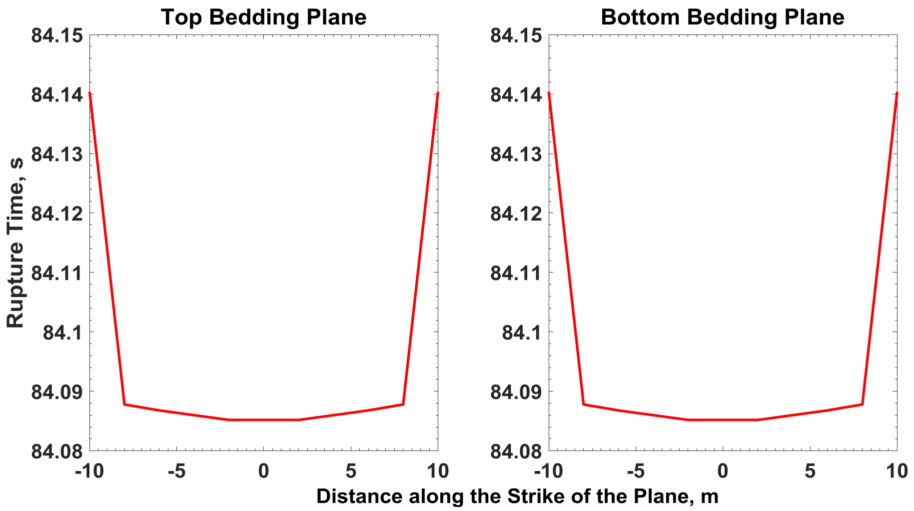

Figure 4.11 Rupture along the BPs in the case when σ_1= 35 MPa (in Figure 4.8). Rupture time at a location is defined as the moment when the two walls at that location start to slide. We can see both the ruptures along the BPs initiate at the center and then propagate bilaterally. The rupture speeds are first fast and then become slower.

To summarize, the BPs are relatively easily activated when the HF crosses them by a short distance because more significant principal direction re-orientation occurs behind the fracture tip than beyond the fracture tip. Some model input parameters such as cohesion, critical slip distance, rock density and maximum principal stress have impacts on the BP activation. In the models, the rupture could propagate bilaterally along the BPs.

4.3.3 Scenario III-Activation of the BPs when a propagating HF deflects into the BPs and fluid invasion occurs

In the models of this scenario, we assume that the HF deflects into the BPs after they intersect. In our models, the interstitial fluid pressure on the BPs, P_{int}, which is essentially p in Equations (2.7), (2.9) and (2.11), equals the pore pressure before fluid penetration and the pressure of the penetrated fluid after fracturing fluid penetration. Following Chuprakov et al. (2015), we calculate the penetrated fluid pressure on a BP as below. First, we keep calculating the net pressure within the HF after the HF intersects with the BP as if the HF continues to propagate along the vertical direction. Second, we add the calculated net pressure and the closure pressure (the minimum principal stress) to obtain the fluid pressure. Third, we project the above fluid pressure onto the BP as the penetrated fluid pressure. Figure 4.12 shows the shear slip and open width. The maximum slip magnitude is about 3.257 mm and the slip-length is about 16 meters on one side of the intersection point. The shear activation is much larger than that in the first two scenarios. And the BPs have a very small opening around the center and the largest opening width is about 0.478 mm. The interstitial fluid pressure, normal stress, shear strength and shear stress along the BPs at the end of the hydraulic fracturing are shown in Figure 4.13. We can see P_{int} is a little larger than the normal stress around the center and causes the opening.

Different senses of shear stress cause the opposite sense of slip along the BPs and slip distribution along the two BPs are anti-symmetric about the origin (or the wellbore where the fracture originates, see Figure 4.1).

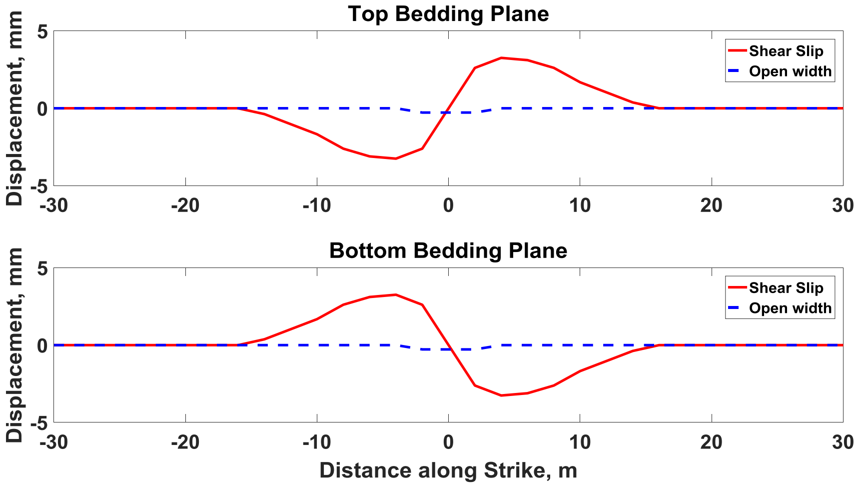

Figure 4.12 Shear slip and open width along the BPs when fluid penetration occurs. Each BP has a very small opening and anti-symmetric shear slippage around the center.

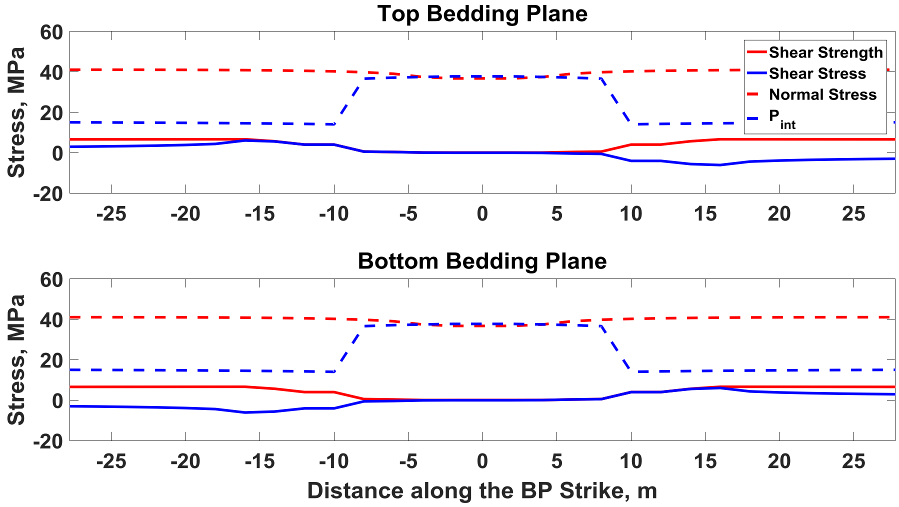

Figure 4.13 Normal stress, interstitial fluid pressure, shear strength and shear stress along the BPs in Figure 4.12. The HF and the two BPs intersect at x = 0 meter. We can see P_{int} is a little larger than the normal stress around the center and causes the small opening. The induced shear stress is anti-symmetric about the center.

4.3.3.1 Rupture along the BPs

The rupture along the BPs when fluid penetration happens also was studied (Figure 4.14). From the rupture curves, we can see some slow rupture (inclined line segments) and fast rupture (almost horizontal small line segments). Same with the previous scenario, the rupture initiates from the center. The rupture penetrates very fast bilaterally at a speed of about 2500 m/s (close to the shear wave velocity) first, and then slow down to a speed of about only 0.564 m/s and increases to a high speed of about 560 m/s and then decreases to a low speed of 0.555 m/s and zero at the end. The slow rupture is fluid-driven, and the fast rupture is caused by dynamic stress perturbations.

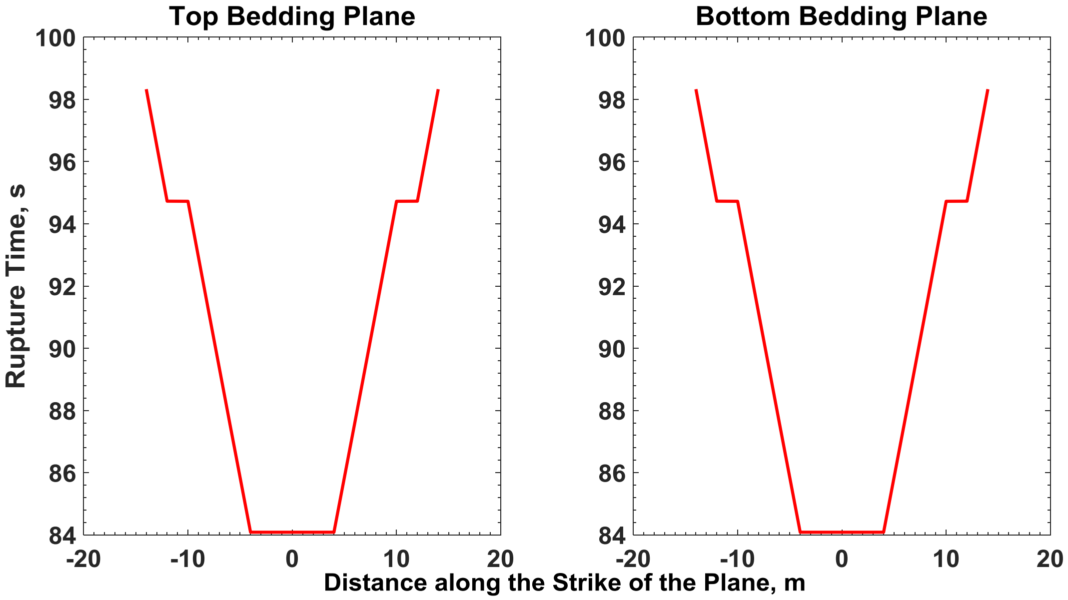

Figure 4.14 The rupture along the BPs in the case when fluid invasion occurs. Rupture time at a location is defined as the moment when the two walls at that location start to slide. There are ‘fast’ ruptures and ‘slow’ ruptures. The slow ruptures could be fluid-driven, and the fast ruptures are induced by perturbations of stresses and pore pressure.

4.4 Discussion

In our models, the maximum dynamic shear stress is studied by comparing the dynamic shear stresses that occur during the whole hydraulic fracturing process. It reflects the maximum shear strength of the BPs that could allow shear slip on the BPs. Although the dynamic changes in the two normal stress components matter on BP activation, we use the maximum dynamic shear stress as a main measurement to show the effect of some input parameters. Our base model parameters are based on the Cotton Valley tight sand gas reservoir and a gel fracturing treatment. The model parameters are also varied to study their effects on the maximum dynamic shear stress. From Figure 4.3, we can see, for the input parameters over the range of interest, density could have a small effect (only 0.5 MPa increment from 2600 to 2800 kg/m^3), whereas HF half-length and injection rate have more significant effects (several MPa increment over their ranges, respectively). In the base example, a gel fracturing fluid is injected at a flow rate of 0.12 m^3/s (about 45 bpm), the maximum dynamic shear stress could be around 9 MPa, which is significant and could cause a relatively large principal direction reorientation. However, for most of the slick-water fracturing treatments, the fluid net pressure is small, and the induced shear stress on horizontal bedding planes is small as well. The principal direction reorientation is of minor significance, which will be much harder to activate horizontal bedding planes. In some field examples, BP slip with the slick-water fracturing is indeed observed or inferred. In these field cases, inclination of the layer interfaces could facilitate the BP activation during low net-pressure fracturing treatments. In general, it is very hard to activate a BP which is perpendicular to a principal stress (Zoback, 2010).

We setup three scenarios to study BP activation as discussed above. In the first two scenarios, the activation of the BPs is caused only by deformation of HF opening and propagation. In fact, they can be combined in one scenario and viewed as at different moments. However, it is tested and confirmed to be much harder to activate the BP in the first scenario than in the second scenario. Therefore, we keep them separate to give some flexibility of varying the strength of the BPs. Cooke et al. (2001) also varied the strength of bedding contacts from zero strength ($\mu=0$; c=0 MPa) to study fracture termination controlled by activation (sliding-only, opening-only, or combined mechanism) of bedding contacts. The bedding contacts between sandstone and shale would become very slippery when wet (liquid invasion) (Frank, 2004). The Cotton Valley tight sand reservoir also has some thin shale zones. The wet bedding contacts could have very low frictional coefficients. Very low-strength BPs could be activated by the deformation caused by HF opening and propagation as shown in Figure 4.4. Our model results verify this model (e.g., Rutledge et al., 2015; Stanek and Eisner, 2013; Tan and Engelder, 2016). The larger principal direction reorientation behind the fracture tip makes it easier to activate a BP when the HF crosses it by a short distance.

Different model parameters have different effects on activations of the BPs. In Figure 4.9, we can see a small amount increase (0 to 1.75 MPa) in cohesion could completely prevent the BPs from being activated. When the critical slip distance in the slip-weakening friction law is much larger than the maximum slip magnitude, its effect on activation of the BPs becomes very limited. The BPs are perpendicular to the vertical stress, which is the maximum principal stress, in our models. Therefore, the vertical stress acts as normal stress on the BPs. The higher it is, the harder the BPs are to be activated. As for the rupture study in Figures 4.11 and 4.14, we can see the rupture happens in a very narrow time window (84.085-84.140 second) in Figure 4.11 and a wider time window (84-98 second) in Figure 4.14. Because we don’t include fluid invasion in the model of Figure 4.11, the speedy rupture is caused by the perturbations on the stresses and pore pressure. However, we consider fluid penetration into the BPs in the model of Figure 4.14, and the average velocity of the fluid diffusion along the BPs is about 0.561 m/s, which is roughly the same with the slow rupture speeds. The intermittent fast ruptures are caused by perturbations on the stresses and pore pressure, which are similar to those in Figure 4.11. Therefore, the ruptures along the BPs could be induced by different mechanisms: dynamic stress perturbations and/or fluid penetration. The rupture speed is related to which factor dominates and induces failure along the BPs. Fluid penetration could cause slow slip, which Gischig (2015) also presented. The rupture along a BP is symmetric about the center. In Figure 4.13, for example, the shear strength is symmetric about the BP center and the dynamic shear stress is anti-symmetric about the center. Therefore, the resultant slip distribution is anti-symmetric and the rupture along the BP is symmetric about the center.

Here we discuss the issues of the stress singularity around a fracture tip and the model element size. Although the stress field near a fracture tip varies dramatically and is even singular in an elastic medium, non-elastic processes must occur near the fracture tip to dissipate some energy, spread stress variations to a finite size of zones near the fracture tip, and remove stress singularity. The slip-weakening friction law for shear fractures in our models essentially takes into account these effects for BP slip. In principle, any given grid size, no matter how fine it is, cannot resolve a singular stress field, which is actually not physical (i.e., the singular stress field is a merely mathematical solution with an assumption of elastic deformation that cannot be true physically). We use a finite element size (2 m in most models) and therefore the stress perturbations can be considered as the averaged values over the length scale of the element size. However, these averaged stress perturbations may be considered as the results of non-elastic processes occurring near the fracture tip, which is more physical than a singular stress field. Element-size independence is also verified as below.

We performed numerical experiments when the maximum principal stress σ_1=35 MPa (i.e., a case in the bottom left plot of Figure 4.9) with different element sizes. We investigate the shear stresses and shear strengths along the BP at the end of simulation. The results are shown in Figure 4.15. We can see that the shear stresses and shear strengths along the BP from different element-size models match each other well, respectively.

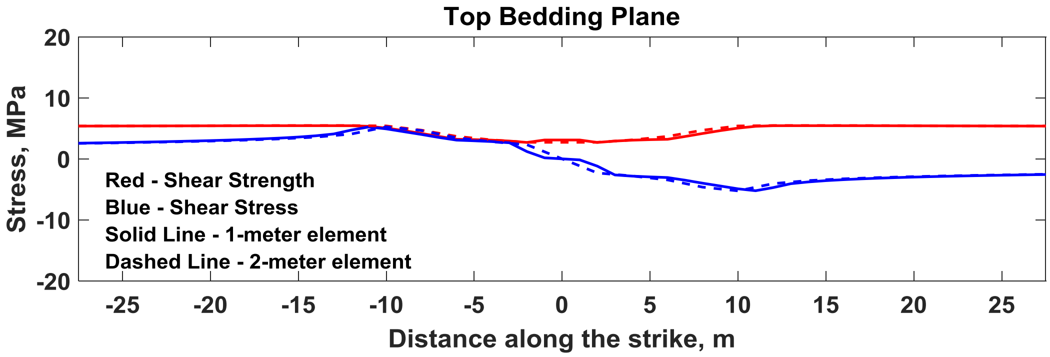

Figure 4.15 Shear stress and shear strength along the top BP at the end of simulation when the maximum principal stress σ_1=35 MPa (i.e., a case in the bottom left plot of Figure 4. 9) with different element sizes (i.e., 1 m and 2 m). We can see that they match each other well in different element size models respectively.

4.5 Conclusions

Our in-house dynamic geomechanics finite element code is applied to study bedding-plane slip based on the Cotton Valley tight-sand reservoir properties and we achieve following conclusions:

1. The maximum dynamic shear stress induced during hydraulic fracturing occurs close to fracture tip and could cause significant principal direction reorientation.

2. The maximum dynamic shear stress increases with HF length. Injection rates and rock density can also have some effects. Maximum dynamic shear stress increases significantly at low injection rates and gently at high rates, and increases almost linearly with rock density in the range of interest, but not much.
3. When a propagating HF approaches a BP but is still a short distance away, the BPs with strength parameters of $\mu_s \geq 0.15$, $\mu_d \geq 0.10$, and cohesion $c \geq 0.01$ MPa cannot be activated. However, lower-strength BPs could be activated by the induced dynamic stress perturbations (or the deformation caused by HF opening and propagation).
4. When a propagating HF crosses a BP by a short distance, the BPs with strength parameters of $\mu_s \geq 0.15$, $\mu_d \geq 0.10$, and cohesion $c \geq 0.01$ MPa could also be activated because more significant principal direction reorientation occurs behind the fracture tip than beyond the fracture tip.
5. Effect of input model parameters such as cohesion, critical slip distance, rock density and maximum principal stress on the BP activation (including slip length and maximum slip) is investigated. When cohesion, critical slip distance or maximum principal stress increases, the slip length and the maximum slip magnitude along the BPs decrease. Over the rock density in the range of interest (2600-2800 kg/m^3), the slip length doesn't change, and the maximum slip magnitude increases.
6. In our models, the rupture propagates bilaterally along the BPs and could be at different speeds.
7. Fracturing fluid invasion into BPs could weaken the BPs and facilitate the activation. The rupture along the BPs in this case is mainly fluid-driven rupture (slow rupture or creep) along with some fast rupture.

CHAPTER V

DYNAMIC STUDY ON THE FRACTURE INTERACTION AND THE PREDOMINANT FREQUENCY OF THE INDUCED MICROSEISMIC SIGNALS DURING HYDRAULIC FRACTURING[3]

5.1 Introduction

Hydraulic fracturing is a critical well stimulation technology for economically producing oil and gas from reservoirs (Sutton et al., 2010; Warpinski et al., 2012). NFs occur in most unconventional reservoirs and can affect the behaviors of the hydraulic fracturs (Gale et al., 2007; Wu and Olson, 2014). Extensive research including experimental (e.g., Blanton, 1986; Warpinski and Teufel, 1987; Renshaw and Pollard, 1995; Beugelsdijk et al., 2000; Gu, et al., 2011; Bahorich et al., 2012; Yang et al., 2016) and numerical work (e.g., Zhang and Jeffrey, 2006; Dahi-Taleghani and Olson, 2011; Gu and Weng, 2010; Olson and Wu, 2012; Chuprakov, et al., 2013; Wu and Olson, 2014; Zhang et al., 2015; Duan, 2016) has been conducted to study the interaction between the natural and HFs. Activation of the NFs could change the opening profile of the HF (Akulich and Zvyagin, 2008; Duan, 2016). When the fracturing fluid pressure within a HF accumulates and the effective normal stress reached the rock tensile strength, the rock breaks and an abrupt or jerky opening occurs (Hu et al., 2017). Most of these studies are based on a quasi-static framework, whereas abrupt opening and unstable shear slip of fractures are dynamic processes. In this study, we investigate dynamic interactions between a HF and pre-existing NFs.

---

[3] Reprinted with permission from Journal of Improved Oil and Gas Recovery Technology (JIOGRT), Vol 2, He, Z., and Duan, B. "Dynamic study on the fracture interaction and the predominant frequency of the induced microseismic signals during hydraulic fracturing" pp. 48-61 Copyright 2018 with permission from JIOGRT.

When a HF is propagating in a naturally fractured reservoir, seismicity could be induced. Warpinski et al. (2012) studied the induced seismicity in many fracturing treatments in all the major shale basins in North America and found the magnitudes are very small (i.e., -3.0 M_w ~ 1.0 M_w and typically around -2.5 M_w). So, the induced events are called MS events. Warpinski et al. (2013) also pointed out the source mechanisms of the microseismicity still remains ambiguous. Zeng et al. (2014) presented that the opening and growth of tensile fractures and shear slip along fractures during hydraulic fracturing are the major source mechanisms for the induced MS events and showed MS traces recorded on six stations. And these traces include some specific patterns of signals such as isolated spiky signals and continuous signals with coda waves. Similar patterns of MS signals can also be documented in Song et al. (2010). Duan (2016) numerically studied and also presented such characteristics of the induced MS signals from different sources. Different sensors are used to record the MS signals in the petroleum industry and the best sensors used to acquire the MS data will be those with high sensitivity, low self-generated noise and a flat response over the frequency range of interest (Warpinski 2009). In microseismic monitoring, there are two main types of sensors: 'omni-geophone' and 'GAC' (Geophone Accelerometer) sensor. An omni-geophone can be placed in any orientation and a GAC sensor can provide acceleration data. Geophones measure velocity and accelerometers measure acceleration. However, they respond well to different ranges of frequency (Warpinski, 2009). Determination of predominant frequencies could be helpful for sensor selection (Maxwell, 2014). In this study, we investigate whether some model parameters such as the rock properties and injection parameters could affect the predominant frequencies of the MS signals.

5.2 Model

Figure 5.1 shows the model setup. There is one HF and one set of inclined NFs in the model. This set of NFs includes eight uniformly distributed NFs. The red triangles in the model indicate the location of the receivers. The parameters are listed in Table 5.1. The reservoir is assumed to be at around 2500 meters in depth. The maximum and minimum horizontal stresses and initial reservoir pore pressure are 55, 40 and 25 MPa, respectively. Based on the data from Stanford Rock Physics Laboratory (i.e., Mavko, 2005), the rock property values are selected. Some shale samples show frictional coefficients around 0.4 (Kohli and Zoback, 2013). The fracturing fluid with a viscosity of 0.02 Pa · s is injected at a rate of 0.053 m^3/s (i.e., about 20 bpm).

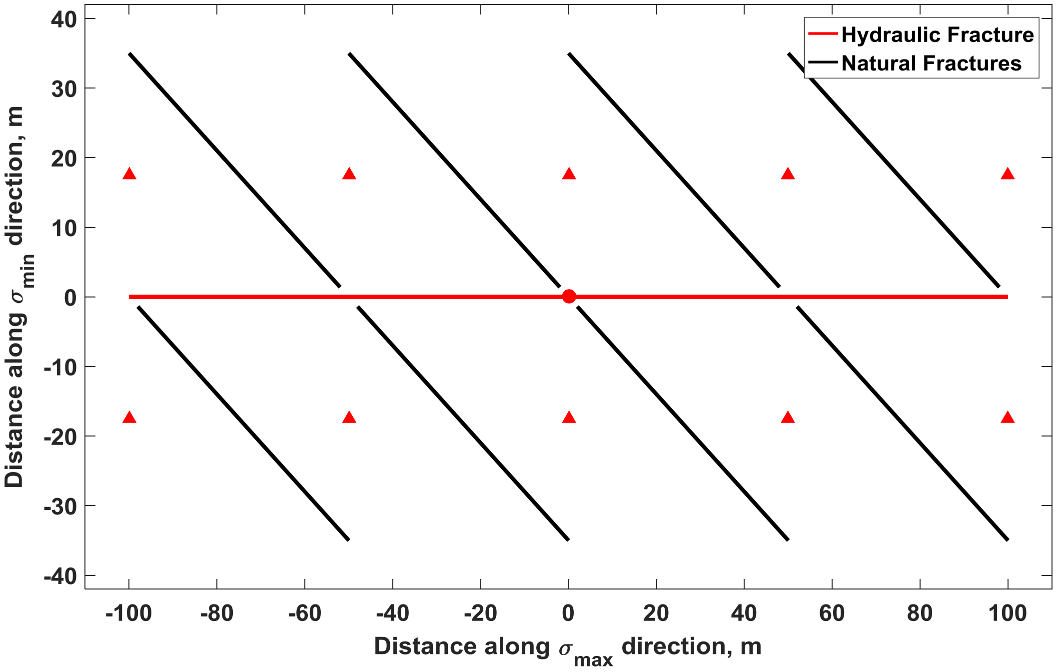

Figure 5.1 Model setup

Table 5.1 model parameters

Parameters	Model A	Model B (Base model)	Model C
Density ρ (kg/m^3)	2400		
Young's modulus E (GPa)	10.0		
Poisson's ratio ν	0.2		
P wave velocity V_p (m/s)	2200		
S wave velocity V_s (m/s)	1300		
Static friction μ_s	0.35		
Dynamic friction μ_d	0.25		
Critical slip distance d_0 (m)	0.001		
Cohesion c_o (MPa)	10.0	0.35	0.70
Skempton's coefficient B	0.8		
Tensile strength T (MPa)	1		
Initial σ_{xx} (MPa)	55		
Initial σ_{yy} (MPa)	40		
Initial σ_{xy} (MPa)	0		
Initial pore pressure p (MPa)	25		
Injection fluid viscosity η (Pa · s)	0.02		
Hydraulic fracture height h_f (m)	50.0		
Injection rate i (m^3/s)	0.053		

5.3 Results and analysis

5.3.1 Activation of the NFs in different models

When the HF is propagating in the reservoir, the induced stress perturbations could activate some of the NFs. The activation of the NFs of the three models (i.e., Models A, B and C in Table 5.1) is shown in Figure 5.2. In Model A, the cohesion of the NFs is the largest and we can see no NFs are activated. Model B has a much smaller cohesion (i.e., 0.35 MPa), and all the NFs are activated along the whole length. Model C has a little larger cohesion (i.e., 0.7 MPa) than Model B, and only some of the NFs are activated. We can see the lower (i.e., the region with negative y values in Figure 5.1) fourth (counted from left to right) and the upper first NFs are entirely activated, and the lower second and the upper third NFs are partially activated although the slip magnitudes are very small comparatively (i.e., the inset plots in Figure 5.2).

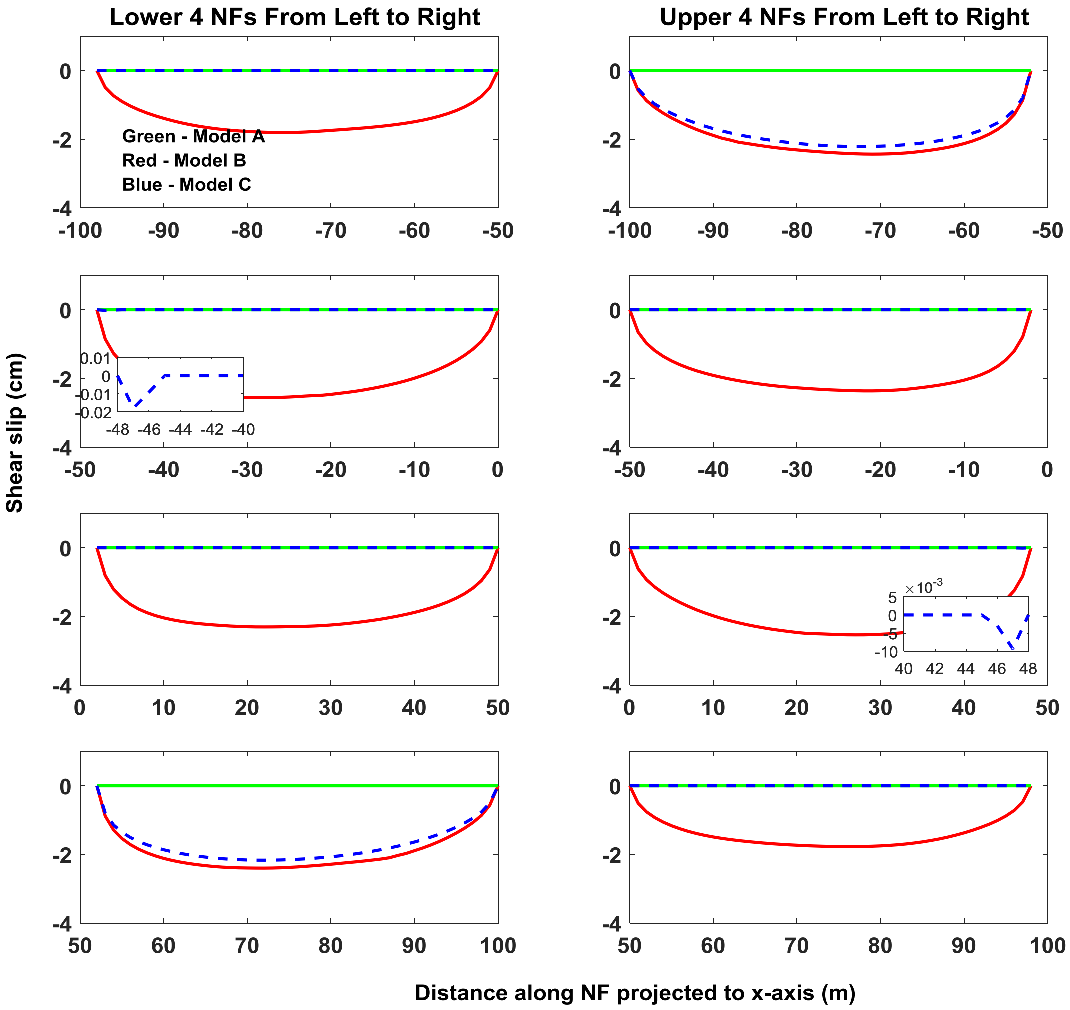

Figure 5.2 Activation of the NFs in the Models A, B and C.

In the models, cohesion affects the shear strength of the NFs based on Coulomb failure criterion (i.e., Equation (2.7)). When the cohesion is very large (e.g., Model A), the induced shear stress cannot reach the shear strengths along all the NFs and none of them can be activated. When the cohesion is very small (e.g., Model B), the shear strengths of the NFs are also very small, and the shear stress can reach the shear strengths along all the NFs and cause failure. However, when the cohesion is moderate (e.g., Model C), only some of the NFs that are in the unstable regions around the HF could be activated. Warpinski et al. (2013) showed the stability in a case without leakoff. The regions normal to the HF are stable and the regions around and beyond the HF tips are unstable. At the beginning of a hydraulic fracturing treatment, the HF length is small. The induced stress perturbations are limited and cannot activate any NF. When the HF propagates longer, the entire lower fourth and upper first NFs (including parts of the upper third and lower second NFs) are in the unstable regions and activated.

5.3.2 Displacement profiles along the HF in different models

In Figure 5.3, the top panel (a) shows the displacement profiles of the HF walls in the three models, the middle panel (b) shows the width profile along the HF, and the bottom panel (c) shows the shearing profile (i.e., the relative displacement of the two walls in the shear direction) along the HF. In Model A, there are no NFs activated as shown in Figure 5.2, and the two HF walls open in the opposite directions. The open width profile is almost elliptical as shown in Figure 5.3(b) and there is no shearing between the two walls as shown in Figure 5.3(c). In Model B, all the NFs are activated. The displacement profiles of the two HF walls are greatly distorted. The flow channel along this HF is very tortuous. In Figure 5.3(b), the width profile has three peaks at x = -50, 0 and 50 meters corresponding to the effect of the slip of the NFs intercepting x-axis at x = -50, 0 and 50 meters. From Figure 5.3(b), we can see that the HF only propagates to 80 meters. So, the other two NFs intercepting x-axis at -100 and 100 meters do not have much impact on the width profile. Figure 5.3(c) shows there is shearing along the HF. In Model C, the lower fourth and upper first NFs are entirely activated, and the lower second and upper third NFs are partially activated with very small slip at one end respectively. In Figure 5.3(b), the width profile has significant change at x = -50 and 50 meters corresponding to the effect of the activated NFs intercepting x-axis at -50 and 50 meters. Also, there is shearing along the HF, and different sense of shear can occur.

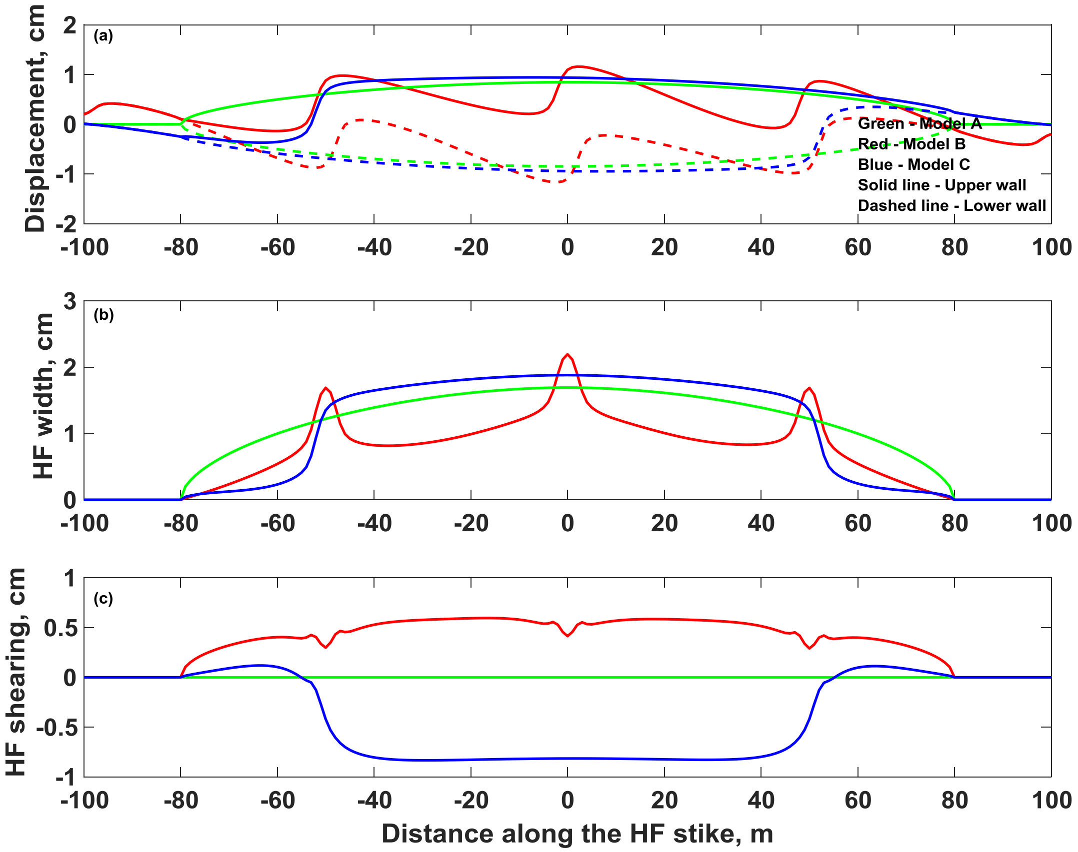

Figure 5.3 The top panel shows the displacements of the two HF walls in the three models; The middle panel shows the width profile along the HF; And the bottom panel shows the shearing profile along the HF.

Figure 5.4 shows the evolution of the HF width at the wellbore in the three models. In Model A, no NFs are activated. There is no interaction between HF and NFs and thus no abrupt change in the width. However, Models B and C produce abrupt/jerky openings during the hydraulic fracturing process. The abrupt opening occurs at around 98 seconds in Model B and 163 seconds in Model C and are caused by the interaction between the HF and the activated NFs. After this abrupt opening, the HF width gradually gets back to the normal trend (i.e., green line in Figure 5.4). By looking at the curve of the HF width evolution more closely (i.e., the inset plot of Figure 5.4), the HF has closing and opening motions.

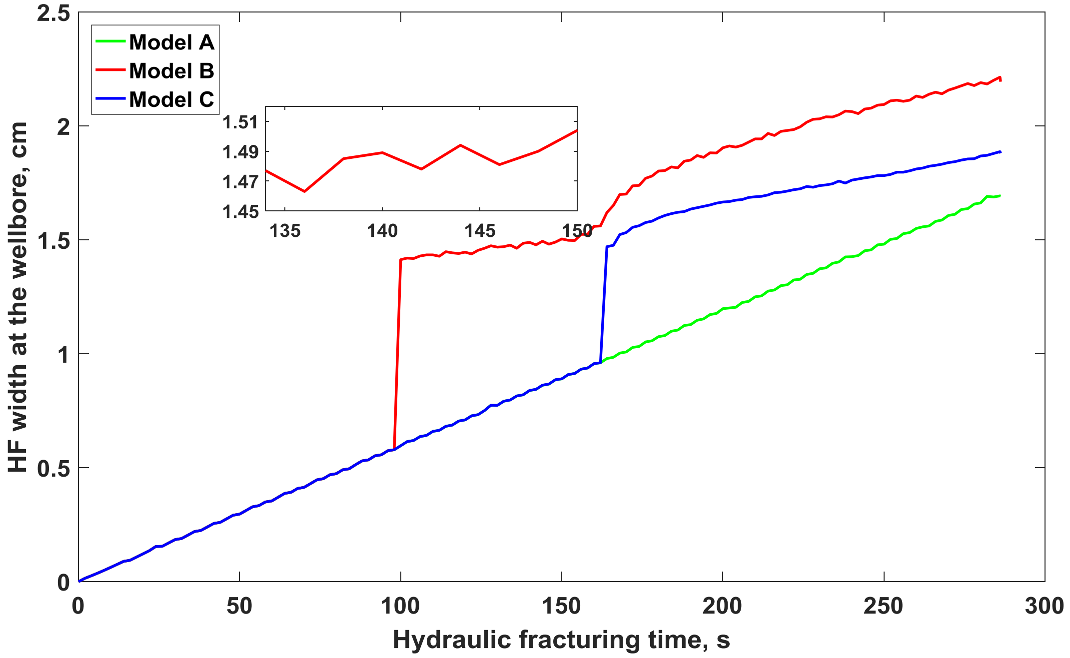

Figure 5.4 Evolution of the HF width at the wellbore in the three models.

5.3.3 Rupture along the NFs in different models

The rupture along the NFs in Models B and C are shown in Figures 5.5 and 5.6, respectively. From Figure 5.5, we can see that the NFs are activated and slide at around 98 seconds, which is corresponding to the time when the abrupt opening of the HF at the wellbore occurs. The patterns of the rupture (i.e., rupture directionality and speed) along the NFs could be very different. The ruptures could be unilateral (i.e., Figures 5.5(a) and 5.5(h)) and bilateral (i.e., Figures 5.5(b), 5.5(c), 5.5(d), 5.5(e), 5.5(f) and 5.5(g)). The rupture speeds in the Figures 5.5(a) and 5.5(h) are almost constant along the NFs and they are 2173 m/s and 2157m/s, respectively.

The speeds of the other ruptures vary along the NFs. Looking at Figures 5.5(c) and 5.5(f) for examples, both the ruptures initiate from an inner location on the NFs and then propagate bilaterally to the two ends. From the initiation point to the two ends, the rupture starts from a very slow speed and then gradually accelerates to a high speed respectively. In Figure 5.6, there are some blank plots (i.e., Figures 5.6(b), 5.6(d), 5.6(e) and 5.6(g)), which indicate that the NFs are not activated. By looking at the Figures 5.2 and 5.6 together, we can see that the ruptures in Figures 5.6(a) and 5.6(h) are large while the ruptures in Figures 5.6(c) and 5.6(f) are very small and would not affect the HF opening much. Therefore, the abrupt opening of the HF in Model C shown in Figure 5.4 is caused by the activation of the upper first (i.e., Figure 5.6(a)) and lower fourth (i.e., Figure 5.6(h)) NFs. The activation of these two NFs occurs around 163 seconds, which corresponds to the time when the abrupt opening of the HF happens.

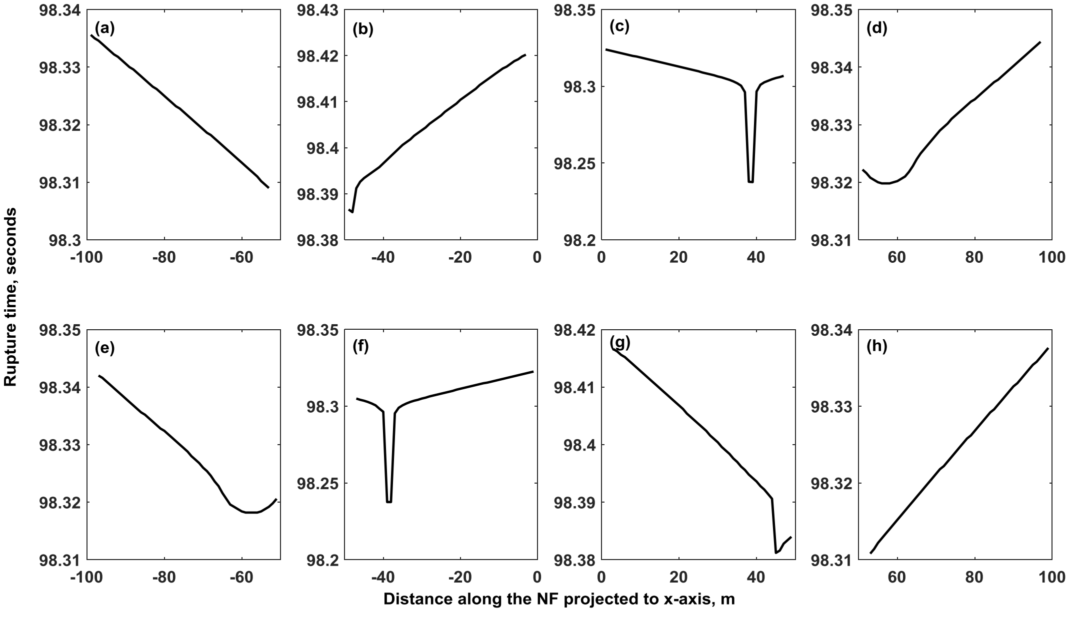

Figure 5.5 Rupture along the NFs in Model B (i.e., cohesion = 0.35 MPa).

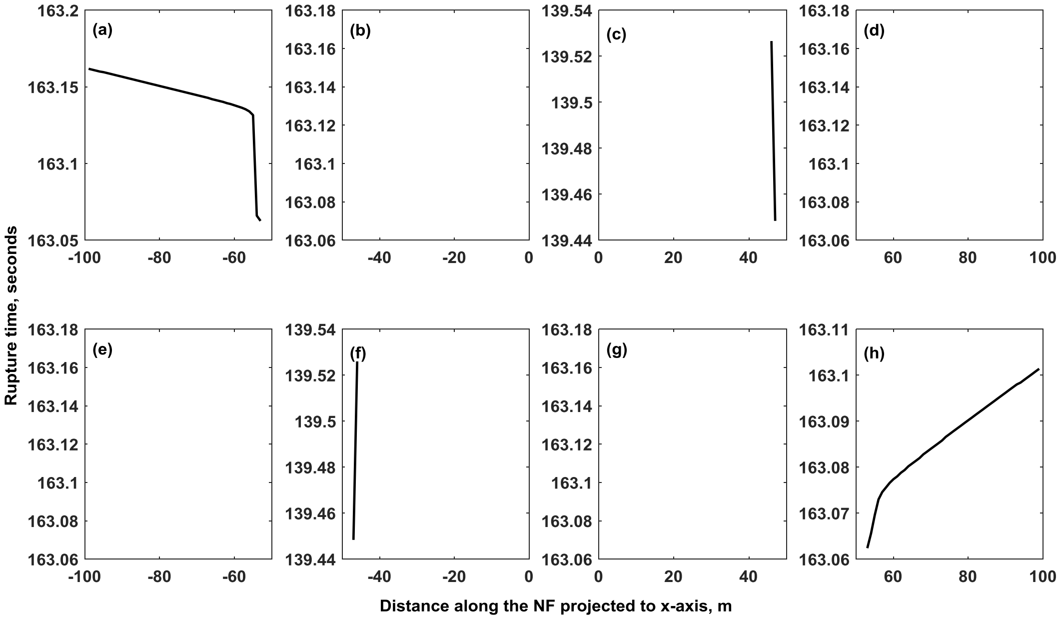

Figure 5.6 Rupture along the NFs in Model C (i.e., cohesion = 0.7 MPa).

5.3.4 Induced microseismicity in different models

The x- and y- components of the seismogram of the induced microseismicity during hydraulic fracturing in Models A, B and C are shown in Figures 5.7 and 5.8, respectively. In Model A, there are no NFs activated. So, the only source of the MS signals is the non-smooth opening (e.g., the slightly wiggly opening profile in Figure 5.4) of the HF as suggested by Duan (2016). Isolated spiky signals are generated in both x- and y- components and they are seismic signals with very short rise time as shown in the inset plot of Figure 5.7. Therefore, these isolated spiky signals are induced by HF non-smooth opening, as proposed by Duan (2016). In Model B, there are NFs activated at around 98 seconds. Comparing the Models A and B in Figures 5.7 and 5.8, the MS signals are the same from 0-98 seconds. When the NFs are activated at about 98 seconds, continuous signals with relatively large amplitude and long-duration and low-amplitude coda waves are generated. These signals are caused by the unstable shear sliding along the NFs as presented in Duan (2016). This is similar in Model C when the NFs are activated at around 163 seconds.

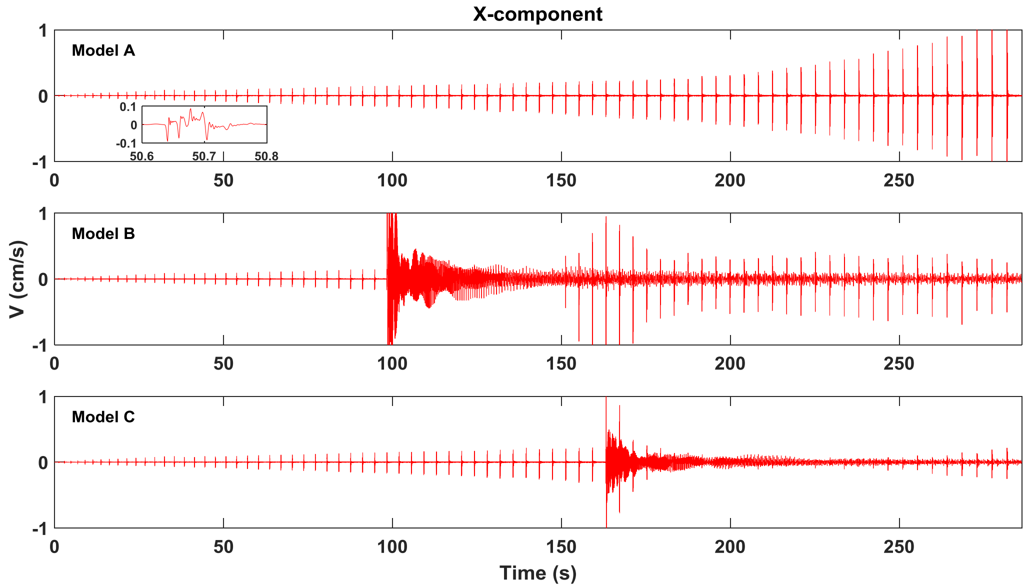

Figure 5.7 The x-component of the induced microseismicity during hydraulic fracturing. The seismic signals are obtained from the lower first receiver, whose location is shown in Figure 5.1.

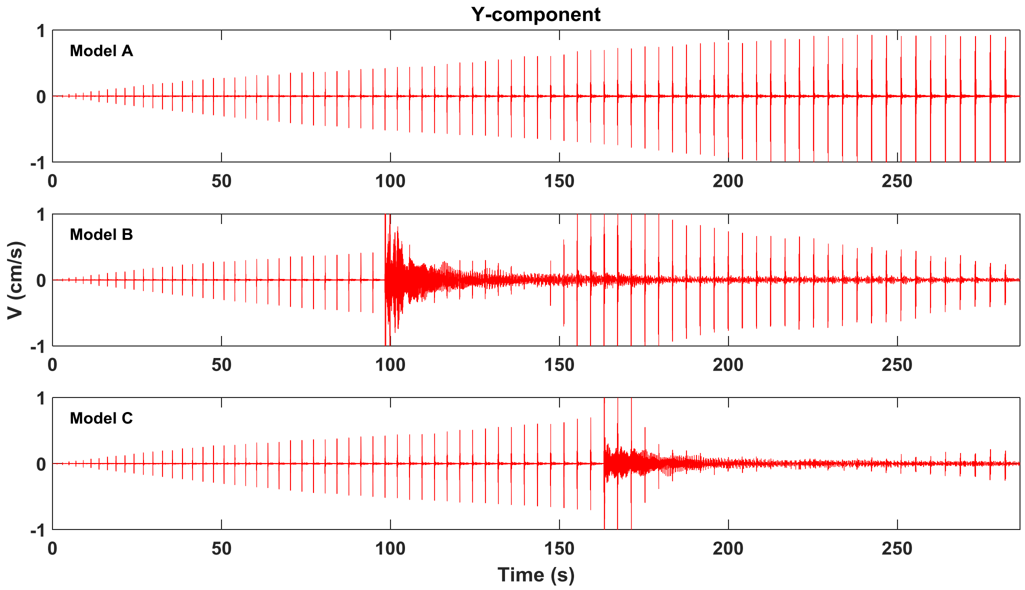

Figure 5.8 The y-component of the induced microseismicity during hydraulic fracturing. The seismic signals are obtained from the lower first receiver, whose location is shown in Figure 5.1.

5.3.5 Predominant frequency of the induced microseismicity

To eliminate the impact of the activation of other NFs on the MS signals, in this section we keep only one NF in each model. Figure 5.9 shows the model configurations with only one NF. In the left plot (i.e., L1 model), only the lower first (L1) NF exists. The black solid line indicates the location of the NF. The black dashed lines indicate the locations of the other NFs in the previous models, but they do not exist in this model. In the right plot (i.e., L4 model), only the lower fourth (L4) NF exists. L1 and L4 models are chosen as representatives based on the fact that the NFs at these two locations have different rupture patterns as shown in Figure 5.5. Different rupture patterns could cause different patterns of frequency spectrums, which is shown later.

In these models, the element length in the x-direction is 1 meter. Six elements are used to represent a full wavelength. So, the highest frequency that can be resolved is $f_{max} = \frac{V_s}{6 \times dx} = \frac{1300}{6 \times 1} = 216.6\ (Hz)$.

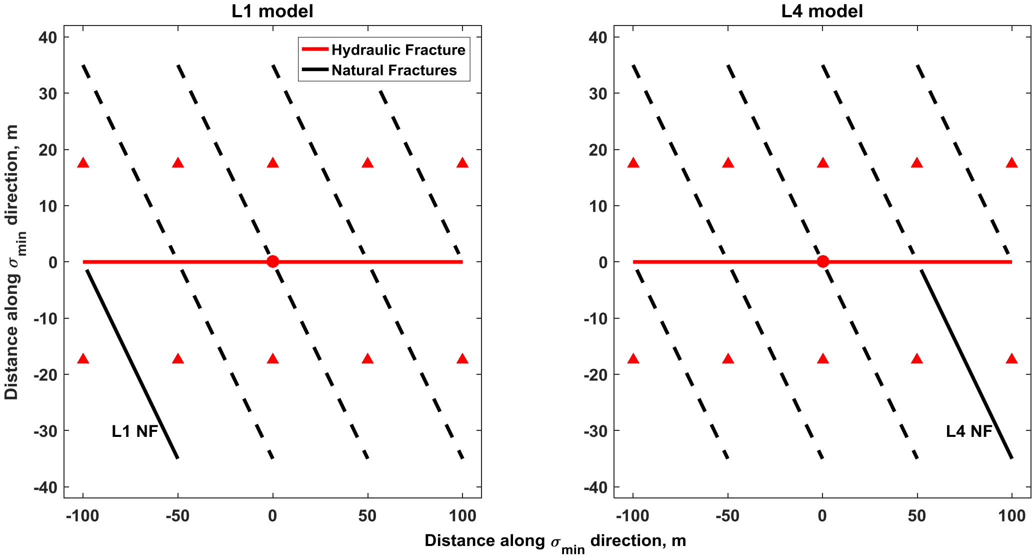

Figure 5.9 Model setup with only one NF.

The seismogram of the induced microseismicity, the spectrum and the rupture along the NFs in these two models are shown in Figure 5.10. The top half is for L1 model. In Figure 5.10 L1(a), we can see that a continuous signal with a coda wave starts to occur around 212 seconds. There are multiple distinct predominant frequencies of 17 Hz, 100 Hz, and 170 Hz as shown in Figure 5.10 L1(b). Figure 5.10 L1(c) shows the rupture along the NF. It initiates around the center and then propagates bilaterally to the left and right sides. The speed varies along each rupture path. The bottom half of Figure 5.10 is for L4 model. A continuous signal appears at about 155 seconds (i.e., Figure 5.10 L4(a)). The spectrum is relatively flat over the frequency range (i.e., Figure 5.10 L4(b)). The predominant frequencies are not distinct, and the spectrum mainly lies in the high frequency band. Figure 5.10 L4(c) shows that the rupture initiates from the left end, and then propagates unilaterally to the right end. The speed varies at the beginning and then remains almost a constant afterwards.

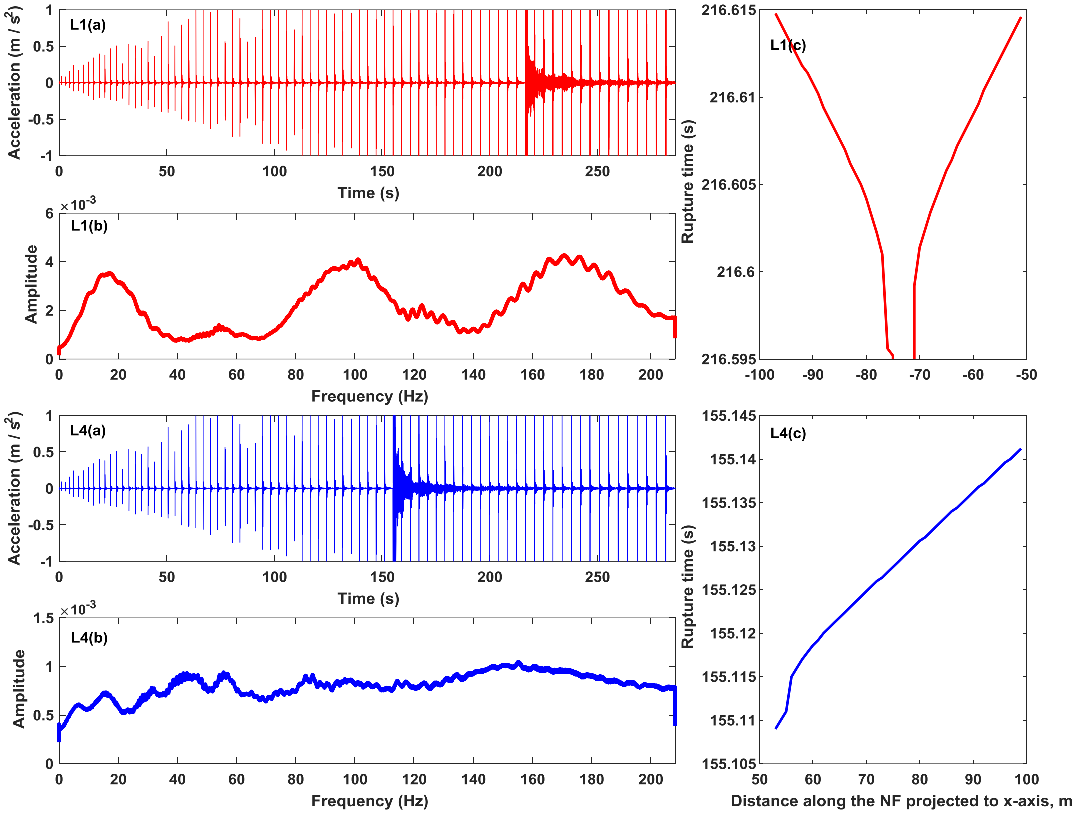

Figure 5.10 The x-component of the seismogram of the induced microseismicity, the spectrum and the rupture along the NFs in the two different models (i.e., L1 and L4). The top half is for the model with only the lower first (i.e., L1) NF, and the bottom half is for the model with only the lower fourth (i.e., L4) NF.

5.3.5.1 Effect of injection rate on the predominant frequency

The effect of injection rate on the predominant frequency of the induced microseismic signals is studied. The L1 and L4 model configurations are also used in this section. The base model parameters are shown in Table 5.1 (i.e., the base model column). For each model configuration, the injection rate is varied in three different cases. The injection rates in the other two cases double and triple the injection rate in the base case, respectively. At the end of the simulation, the HFs propagate to the same length in all three cases.

Figure 5.11 presents the spectrums of the induced microseismicity in the three cases under L1 and L4 model configurations, respectively. The top panel shows the spectrums in L1 model configuration. We can see that there are three distinct predominant frequencies in each of the three cases and the three predominant frequencies in one case are very close to those in the other two cases correspondingly. However, the amplitudes in the higher-injection-rate case are greater than those in the lower-injection-rate case. The bottom panel shows the spectrums in L4 model configuration. In general, the spectrums are all relatively flat and mainly lie in the high frequency band. The predominant frequencies of the three cases are all around 150 Hz. The amplitude also increases with injection rate.

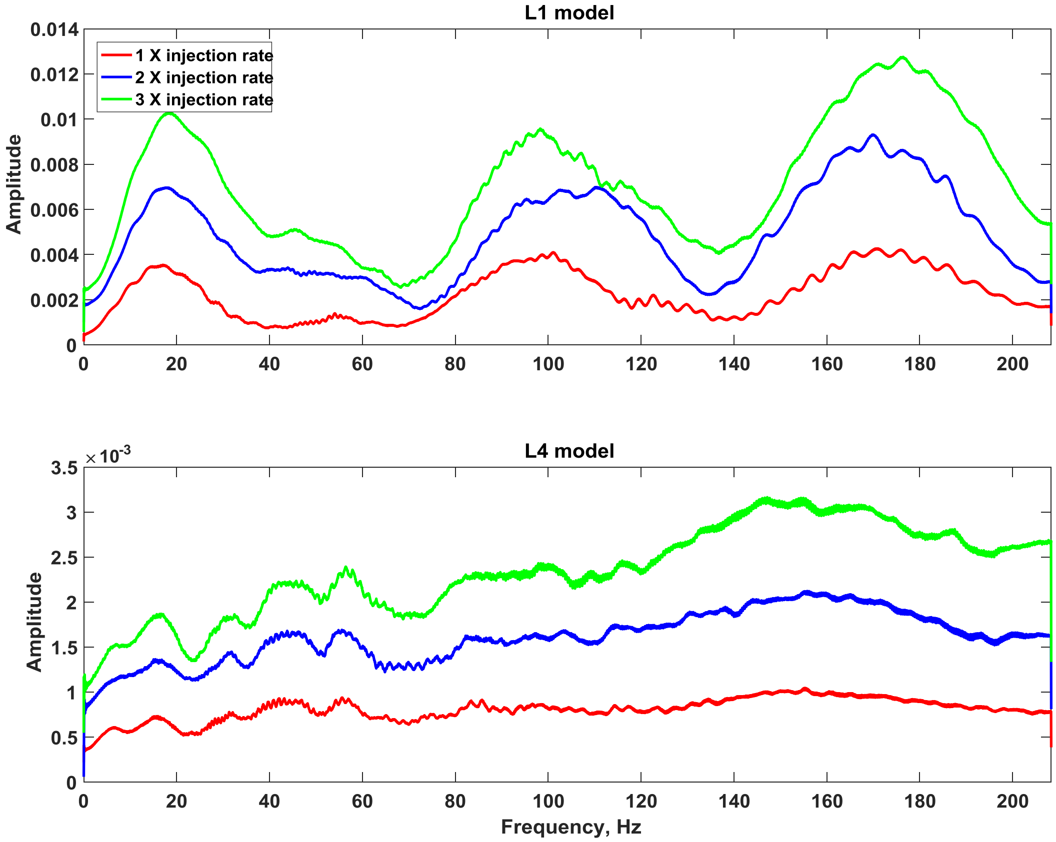

Figure 5.11 Comparison of the spectrums of the microseismicity induced in the models with different injection rates

5.3.5.2 Effect of Young’s modulus on the predominant frequency

We also make use of the L1 and L4 model configurations and investigate the effect of Young’s modulus on the predominant frequency of the induced microseismic signals in this section. The base model parameters are also as in Table 5.1 (i.e., the base model column). For each model configuration, the Young’s modulus is varied in three different cases and are 10.0, 10.8, 11.6 GPa, respectively. At the end of the simulation, the HFs propagate to the same length in all three cases.

The spectrums of the induced microseismicity in the three cases under L1 and L4 model configurations respectively are shown in Figure 5.12. The top panel shows the spectrums in L1 model configuration. For each spectrum, there are multiple distinct predominant frequencies. Comparing different cases and the second predominant frequency, we can see the predominant frequency shifts to the right (i.e., high frequency) when the Young's modulus increases. The spectrums in L4 model configuration are shown in the bottom panel. All the spectrums are relatively flat over the investigated frequency range and it is hard to distinguish the change or shift of the predominant frequencies with the Young's modulus.

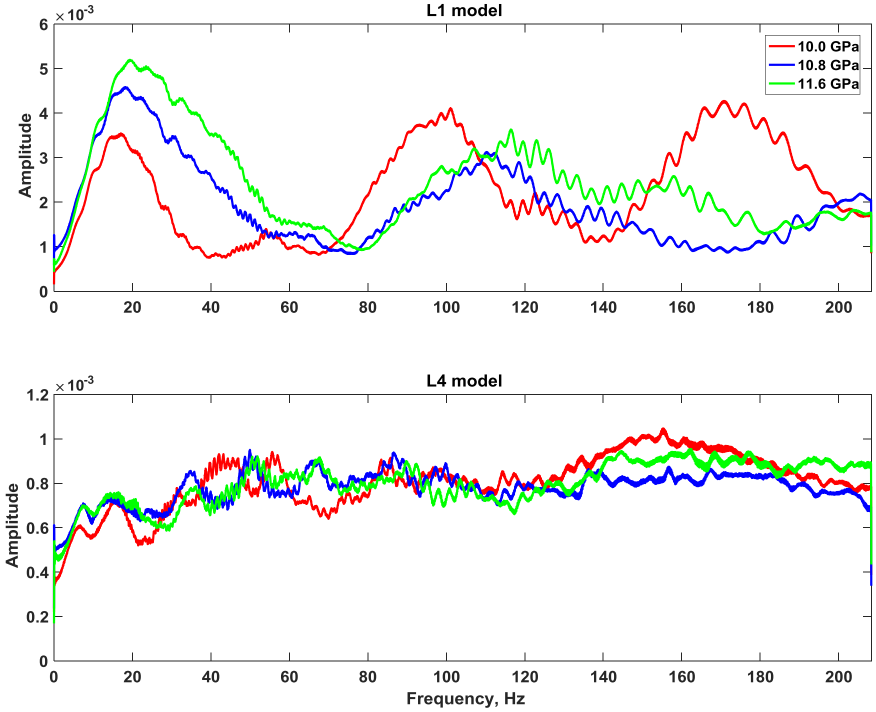

Figure 5.12 Comparison of the spectrums of the microseismicity induced in the models with different Young's modulus.

In summary, from the study on the effects of injection rate and Young's modulus on the predominant frequency of the induced microseismicity, we can see that the spectrum could either have multiple distinct predominant frequencies or could be relatively flat over the investigated frequency range. The injection rate doesn't affect the predominant frequencies much, however, a higher Young's modulus could shift the predominant frequency to the higher side.

5.4 Discussion

During hydraulic fracturing, the activation of NFs and associated microseismic generation and radiation are dynamic processes. Dynamic modeling is needed to accurately model the fracture interaction and induced microseismicity. In this study, we do not attempt to simulate the fluid flow in a HF and thus the spontaneous rupture. The well-known non-leak-off PKN model is implemented. The models still capture the main characteristics of the processes associated with hydraulic fracturing.

In our models, some frequency spectrums have multiple distinct predominant frequencies (e.g., L1(b) in Figure 5.10) and others could be relatively flat over the investigated frequency range (e.g., L4(b) in Figure 5.10). Maxwell and Cipolla (2011) presented similar frequency spectra of MS events induced by hydraulic fracturing. For natural earthquakes, Martin (2016) proposed that the controlling factors of the frequency are the size, geometry and the rupture pattern of the earthquake source. We also studied the rupture patterns in our models and found that rupture directionality could affect the frequency spectrum. Bilateral ruptures may induce multiple predominant frequencies, whereas unliteral ruptures may induce relatively flat frequency spectrums.

Effect of Young's modulus on the predominant frequency of the induced microseismic signals is studied. Young's modulus is not a direct input parameter in our dynamic models but P and S wave velocities, V_p, V_s are. Mavko (2005) presented a saturated shale rock (Pore pressure, P_p around 25 MPa) has V_s of 1300-1500 m/s under the confining pressure of 40-55 MPa. In these studies, varying Young's modulus is achieved by varying V_p and V_s and V_p/V_s is assumed to be about 1.7 for the rocks.

5.5 Conclusions

We apply our in-house finite element geomechanics code to study the fracture interaction and the predominant frequency of the induced MS signals during hydraulic fracturing. Some conclusions are achieved as below.

- Cohesion affects the activation of the NFs during hydraulic fracturing process. The NFs are easier to be activated in the low-cohesion models. The NFs could be activated to different extents. Some NFs may slide along the whole lengths, while some others may slide along just part of the whole lengths.
- The width profile along the HF could be changed by the activation of the NFs. Abrupt opening or closing (i.e., increase or decrease in HF width) could occur when NFs are activated.
- When a NF is activated, the rupture could be unilateral or bilateral along the NF. The speed of the rupture could be constant or varying along the path.
- Rupture patterns (i.e., directionality and speed) along the NFs could affect the spectrum of the induced microseismicity. The spectrum could have multiple predominant frequencies or could be relatively flat over the investigated frequency range.

- Injection rate doesn’t affect the predominant frequencies much. A higher Young’s modulus could shift the predominant frequency to the higher side.

CHAPTER VI

STUDY ON THE MICROSEISMIC CLOUD INDUCED BY HYDRAULIC FRACTURING

6.1 Introduction

During the last decade, MS monitoring has attracted great interest from many oil and gas companies (Warpinski, 2009; Maxwell et al., 2010) as it can be applied to detect the hydraulic fracturing process and estimate the fracture geometry by locating the MS events. Besides the petroleum industry, underground mining and enhanced geothermal systems also need this technology. MS monitoring involves detecting, locating and characterizing the large-number cloud-like induced MS events (Van Der Baan et al. 2013). Location of the induced MS events can spatiotemporally map the orientation and growth of the fracture or the stimulated rock volume (SRV) and dynamics of the fracturing process (Baig et al. 2010; Baisch et al., 2003; Evans et al., 2005; Fischer et al., 2008; House, 1987; Phillips et al., 1998). Based on the parameters for typical hydraulic fracturing treatments in Barnett Shale, Warpinski et al. (2013) and Agarwal et al. (2012) showed the stability around HFs for cases in which leakoff is not considered. The area normal to the HFs are stable, where microseismicity is unlikely to be induced. The area around the fracture tips are unstable, where microseismicity is likely to be induced. Shapiro et al. (2006) studied the hydraulic fracturing processes from the MS data on the basis of PKN model. Fischer et al. (2008) applied principal component analysis (PCA) to quantify the geometry of the MS clouds. Warpinski et al. (2000 and 2001) presented that the microseismicity induced by hydraulic fracturing of a low permeability formation is concentrated in a spatial domain quite close to the HF. However, currently microseismicity remains ambiguous in mechanisms and data interpretation (Warpinski et al. 2013). Liu et al. (2016)

pointed out that it is still ambiguous if the MS cloud geometry could derive the correct or accurate HF geometry or SRV. Interpreting MS results and linking microseismicity to fracture behavior needs a good understanding of geomechanics (Warpinski et al. 2013). Therefore, dynamic geomechanical modeling is needed to accurately model hydraulic fracturing and associated processes such as microseismicity generation and radiation. We know that the primary goal of MS monitoring is to estimate the geometry of a HF. However, to our best knowledge, currently not much effort was made to discover the correlation between the geometry of the HF and the MS cloud by simulation. Dynamic problems of equations of motion are solved with a finite element method (Duan, 2016). We study the following problems. How far could a MS event occur away from a HF? And how can HF length and some parameters such as cohesion of NFs affect the shape of the MS cloud? How is the stability around a dynamically propagating HF? What is the correlation between the geometry of the HF and the MS cloud induced by dynamic stress perturbations in different scenarios when the inclination of NFs relative to the maximum horizontal principal direction varies?

6.2 Model

Figure 6.1 shows the model setup. There is one HF and four hundred uniformly oriented NFs in the model. The HF is propagating in the direction of the maximum horizontal stress and opening in the direction of the minimum horizontal stress. The NFs have a uniform orientation, N70W. Each length is about 50 meters and the spacing of the NFs is about 34 meters. These features are good representatives of the NFs in Barnett Shale (Kresse et al., 2013). The model parameters are listed in Table 6.1 and are based on Barnett Shale at a depth around 2360 meters. The direction of the maximum horizontal stress varies from N30E to N90E based on the information of the drilling induced fractures at this depth (Lancaster et al. 1992). In all our models, we set the direction of the maximum horizontal principal stress aligned with the x-axis. Knowing about the angles between the NFs and the directions of the maximum horizontal principal stress, we can determine the slopes of the NFs in different scenarios, which will be discussed later.

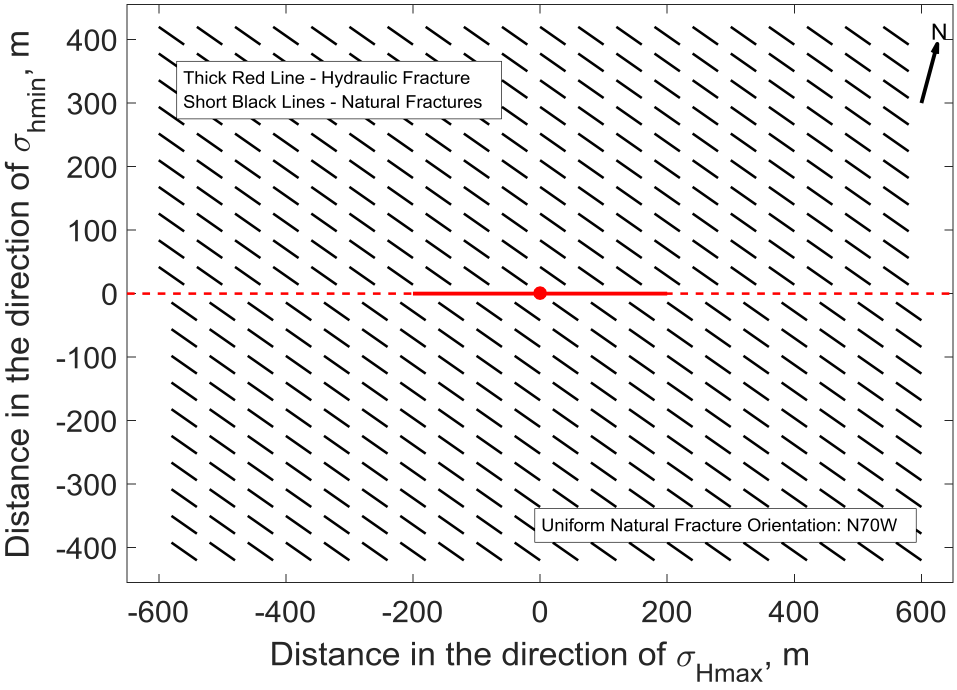

Figure 6.1 Model setup. There is one HF and four hundred uniformly oriented NFs in the model. The north direction is indicated.

Table 6.1 Base model parameters

Parameters	Values
Density ρ (kg/m^3)	2600
Young's modulus E (GPa)	40.0
Poisson's ratio ν	0.23
P wave velocity V_p (m/s)	4000
S wave velocity V_s (m/s)	2600
Static friction μ_s	0.35
Dynamic friction μ_d	0.25
Critical slip distance d_0 (m)	0.001
Cohesion c_o (MPa)	0.35
Skempton's coefficient B	0.8
Tensile strength T (MPa)	1
Initial σ_{xx} (MPa)	42
Initial σ_{yy} (MPa)	33
Initial σ_{xy} (MPa)	0
Initial pore pressure p (MPa)	23.6
Injection fluid viscosity η (Pa · s)	0.005
Hydraulic fracture height h_f (m)	50.0
Injection rate i (m^3/s)	0.33

6.3 Results and Analysis

At the investigated depth, 2360 meters of Barnett Shale, the direction of the maximum horizontal principal stress varies (Lancaster et al., 1992). Therefore, we study different scenarios with different directions of the maximum horizontal principal stress. First, we study the scenario when the maximum horizontal principal direction is N75E. As shown in Figure 6.1, the slope of the NFs, k is -0.7 in this scenario. The MS cloud is studied when the HF propagates to lengths from 50 meters to 200 meters with 25 meters increment in different cases.

6.3.1 Maximum horizontal principal direction: N75E (i.e., NF slope is -0.7)

In this study, we delineate/determine the shape of the MS cloud in this study using a closed elliptical envelope as small as possible to include as many activated NFs or MS events as possible. The estimated/interpreted strike and length are from the long axis of the elliptical envelope. Therefore, the key is to determine the long axis including both the strike (i.e., direction) and length. In this study, a MS cloud includes many events on a 2-dimensional plane and the long axis of the MS cloud envelope is 1-dimensional. So, we apply principal component analysis/algorithm (PCA) to reduce the data from high dimensions (e.g., 2D) to low dimensions (e.g., 1D). Fischer et al. (2008) also applied this method to analyze geometry of the MS clouds. What PCA does is to find a direction (a vector $u \in R^2$) onto which to project the data so as to minimize the projection error. The projection error is defined as the summation of the distance from the data points to a line with a direction. The direction determined from the PCA is used as the strike of the long-axis, and the length of the long-axis is from the line segment between the two most distant projection points. For more details about PCA and some examples from this study, please refer to the Appendix.

When the HF propagates to a short distance, 50 meters in this scenario, no NFs are activated, so no MS events occurred.

When the HF propagates to 75 meters, four NFs occurring around the HF tips are activated as shown in Figure 6.2. In this study, one NF is discretized into four segments. If there are three red-star markers on a NF, it means the NF is activated along its whole length. However, if there are fewer than three red-star markers but at least one on a NF, it means the NF is activated only partially along its length. Since these events are very close to the HF tip in Figure 6.2, the strike and length of the MS cloud long-axis could be good representatives for the real HF. However, because the uniformly orientated NFs in the model are anti-symmetric about the wellbore (i.e., the origin point) but not symmetric about the x-axis, the MS cloud long-axis is not perfectly aligned with the x-axis. The strikes of the HF and MS cloud long-axis have small difference. From PCA, the MS cloud half-length (i.e., half of the long-axis) is about 112 meters and the ratio between the MS cloud half-length, l and the HF half-length, x_f, is l/x_f = 112 m / 75 m = 1.49. The strike difference between the MS cloud long-axis and the HF is about 2.5^o.

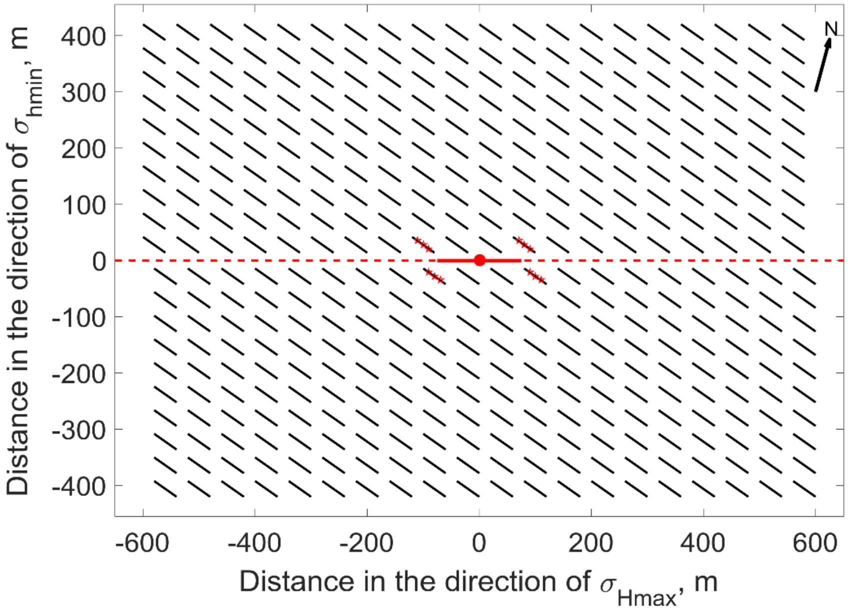

Figure 6.2 Microseismic events/activated NFs in the model when k = -0.7 and x_f = 75 meters. k is the slope of the inclined NFs. x_f is the half-length of the HF. Small red-star markers on a NF indicate the NF is activated. If there are three red-star markers on a NF, it means the NF is entirely activated. If there are fewer than three red-star markers but at least one on a NF, it means the NF is partially activated.

When the HF propagates further to 100 meters, more NFs are activated, so more MS events occurred in the model as shown in Figure 6.3. From the figure, we can see four ‘branches’ (i.e., zones of the activated NFs). However, the two branches in the top right and bottom left quadrants are a little stronger (i.e., more event locations) but not significantly stronger than the other two in the remaining quadrants, which is similar in the following figures in this section. The long axis of the elliptical envelope is a little closer to these two branches than the other two, but still it is almost in the E-W direction. The MS cloud half-length is about 168 meters and the ratio between the MS cloud half-length and the HF half-length is 1.68. The strike difference between the HF and MS cloud long-axis is about 1.4°. It becomes smaller because more MS events occur close to the HF and aligned with the HF strike.

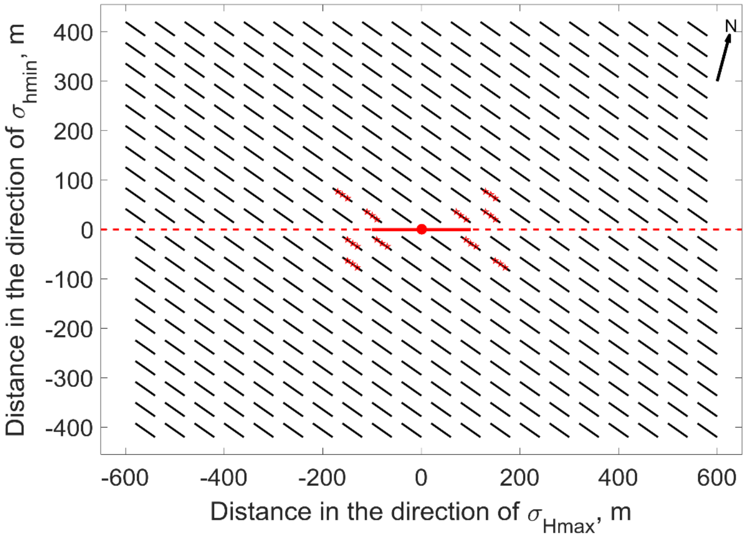

Figure 6.3 Microseismic events/activated NFs in the model when k = -0.7 and x_f = 100 meters. k is the slope of the inclined NFs. x_f is the half-length of the HF. Small red-star markers on a NF indicate the NF is activated. If there are three red-star markers on a NF, it means the NF is entirely activated. If there are fewer than three red-star markers but at least one on a NF, it means the NF is partially activated.

When the HF propagates to 125 meters, more NFs are activated away from the HF than those close to the HF as shown in Figure 6.4. Both the MS cloud length and the strike difference becomes larger. The MS cloud half-length is about 223 meters and the ratio between the MS cloud half-length and the HF half-length is 1.78. The strike difference between the HF and MS cloud length is about 3.4^{o}.

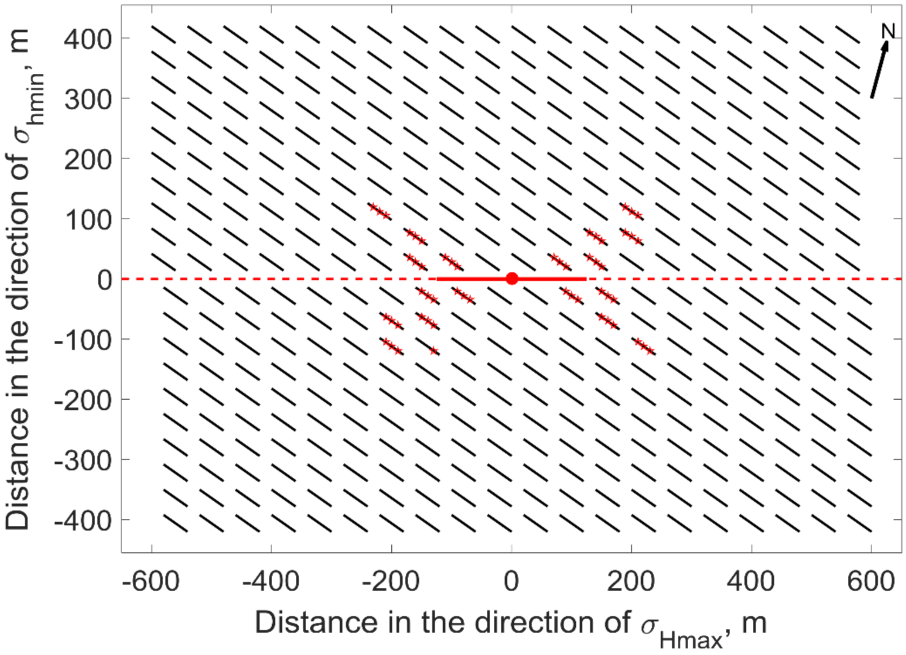

Figure 6.4 Microseismic events/activated NFs in the model when k = -0.7 and x_f = 125 meters. k is the slope of the inclined NFs. x_f is the half-length of the HF. Small red-star markers on a NF indicate the NF is activated. If there are three red-star markers on a NF, it means the NF is entirely activated. If there are fewer than three red-star markers but at least one on a NF, it means the NF is partially activated.

When the HF propagates to 150 meters, some more NFs are activated away from the HF, which increases the MS cloud length and meanwhile some other NFs are activated close to the

HF, which decreases the strike difference (Figure 6.5). The MS cloud half-length is about 341 meters and the length-ratio is 2.27. The strike difference is about 2.4^{o}.

When the HF propagates to 175 and 200 meters, more MS events occur as shown in Figures 6.6 and 6.7. Both the length ratio and strike difference increase. The length ratios are 2.28 and 2.41, and the strike differences are 3.4^{o} and 3.5^{o} in the two cases, respectively.

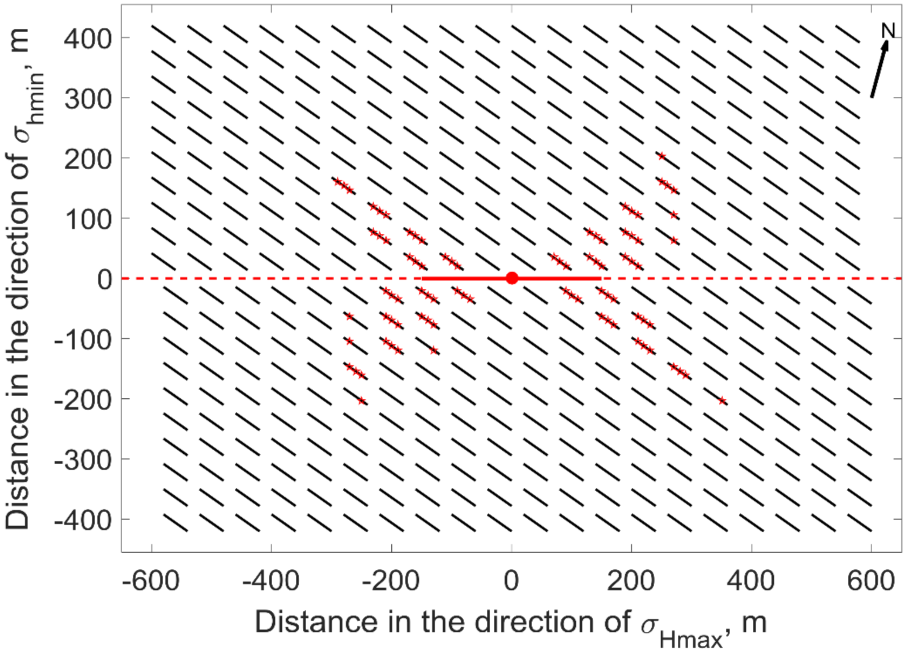

Figure 6.5 Microseismic events/activated NFs in the model when k = -0.7 and x_f = 150 meters. k is the slope of the inclined NFs. x_f is the half-length of the HF. Small red-star markers on a NF indicate the NF is activated. If there are three red-star markers on a NF, it means the NF is entirely activated. If there are fewer than three red-star markers but at least one on a NF, it means the NF is partially activated.

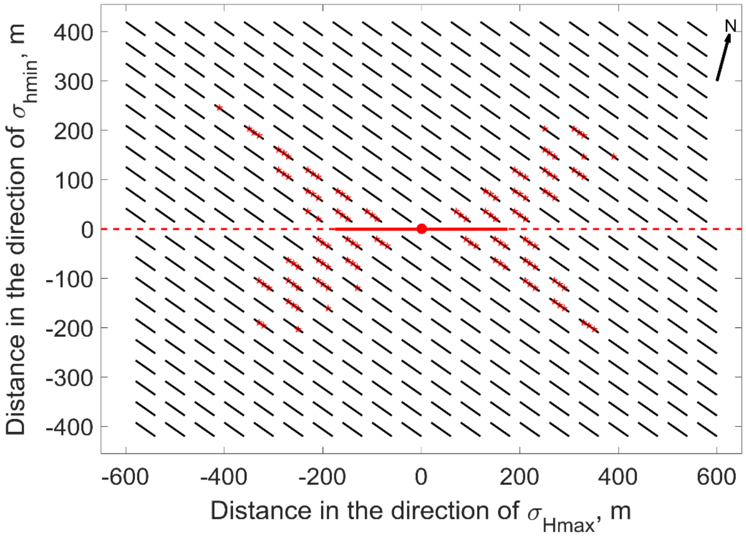

Figure 6.6 Microseismic events/activated NFs in the model when k = -0.7 and x_f = 175 meters. k is the slope of the inclined NFs. x_f is the half-length of the HF. Small red-star markers on a NF indicate the NF is activated. If there are three red-star markers on a NF, it means the NF is entirely activated. If there are fewer than three red-star markers but at least one on a NF, it means the NF is partially activated.

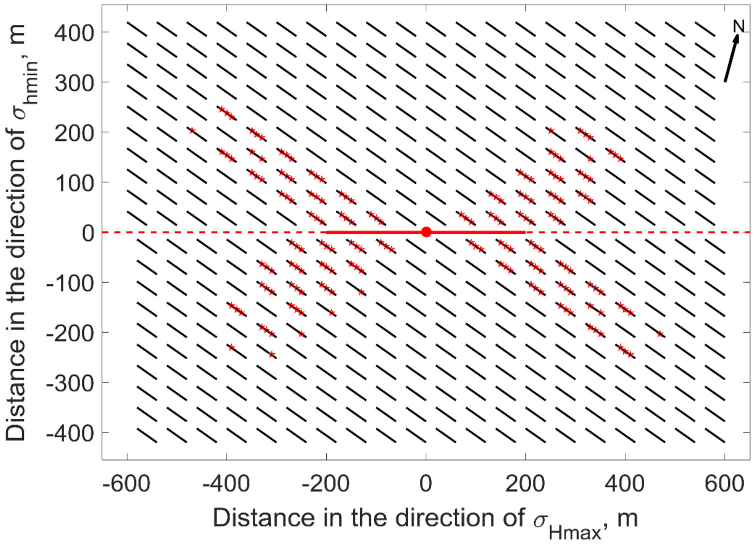

Figure 6.7 Microseismic events/activated NFs in the model when k = -0.7 and x_f = 200 meters. k is the slope of the inclined NFs. x_f is the half-length of the HF. Small red-star markers on a NF indicate the NF is activated. If there are three red-star markers on a NF, it means the NF is entirely activated. If there are fewer than three red-star markers but at least one on a NF, it means the NF is partially activated.

The results of the correlation between the geometry of the HF and MS cloud when the maximum horizontal principal direction is N75E is summarized in Table 6.2. We can conclude that the MS cloud half-length and the ratio between the MS cloud half-length and HF half-length both increase when the HF propagates longer. The strike difference between the MS cloud long-axis and HF is essentially very small, less than 4^{o} in all the cases of this scenario because the four 'branches' are not significantly different in number of the activated NFs and are almost symmetric about the HF. It varies depending on where the activated NFs are located. When the activated NFs are closer to the HF, the strike difference is smaller. And when the activated NFs are further away from the HF, the strike difference is larger.

Table 6.2 Correlation between the HF and MS cloud when σ_{Hmax} direction is N75E

HF half-length (x_f), m	MS cloud half-length (l), m	l/x_f	Strike difference, ^{o}
75	112	1.49	2.5
100	168	1.68	1.4
125	223	1.78	3.4
150	341	2.27	2.4
175	399	2.28	3.4
200	481	2.41	3.5

6.3.1.1 Effect of HF length on the induced MS cloud

Figure 6.8 shows the number of the activated NFs when HF propagates to different lengths. The model parameters are listed as in Table 6.1. We can see that the longer the HF propagates, the more NFs are activated. The number of the activated NFs increases with the HF length in an exponential way. However, only knowing about the number of the activated NFs is not enough to get a sense how they are distributed. In Figure 6.9, the distance of the furthest activated NF with the HF length is plotted. First, we plot the data points and then add a trend line. The trend line shows the distance of the furthest activated NF increases with the HF length. When the HF is short (e.g., less than 80 meters), the MS events are concentrated in a spatial domain close to the HF, consistent with the conclusions in Warpinski et al. (2000 and 2001). However, when the HF propagates much longer, the MS events could spread very far away. The distance of the furthest activated NF does not increase so much when the HF length is very large (e.g., greater than 170 meters). The slope of the trend line decreases.

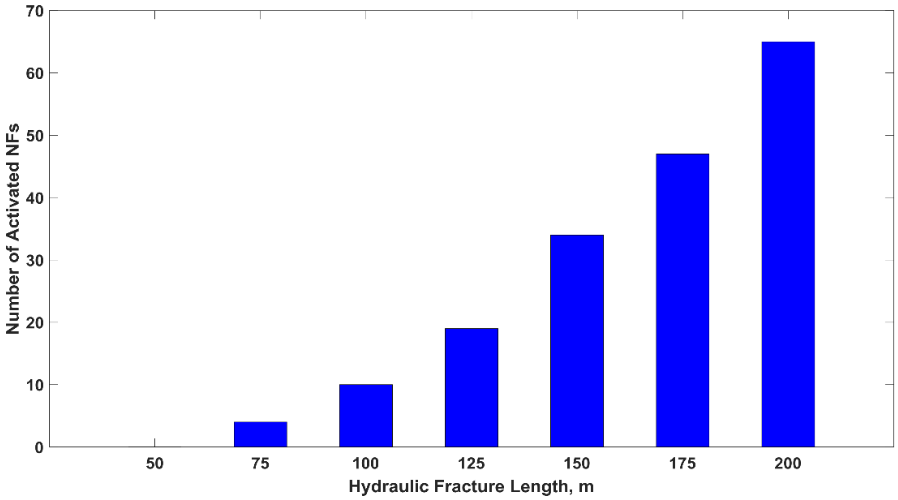

Figure 6.8 The number of the activated NFs when the HF propagates to different lengths. The number of the activated NFs increases with HF length exponentially.

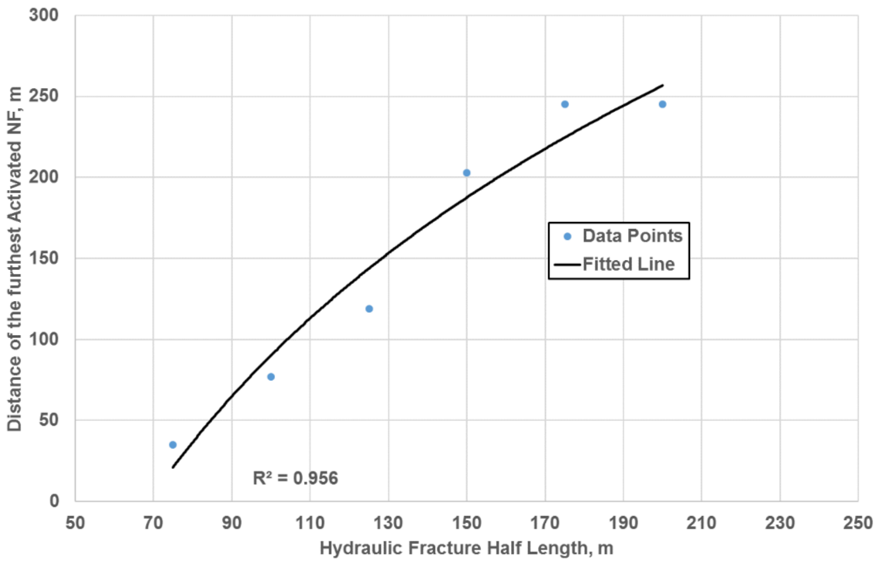

Figure 6.9 The distance of the furthest activated NF when the HF propagates to different lengths. From the fitted or trend line, we can see the distance increases with HF length.

6.3.1.2 Effect of cohesion of NFs on the induced MS cloud

The effect of cohesion of NFs on the induced MS cloud is also studied. In these models, the cohesion varies from 0.05 to 1.05 MPa while other parameters remain the same as in Table 6.1 and the HF propagates to the same length, 200 meters. In Figure 6.10, we can see that the number of the activated NFs exponentially decreases with cohesion. When the cohesion is very low (e.g., less than 0.15 MPa), many NFs are activated in the models. However, when the cohesion becomes larger (e.g., greater than 0.75 MPa), only a few (around 20) NFs are activated. The distance of the furthest activated NF is also studied in different-cohesion models as shown in Figure 6.11. The distance decreases with cohesion in an exponential way as well. When the cohesion is very low, the distance could be over 400 meters. When the cohesion becomes higher, the distance becomes much smaller. In the high-cohesion (e.g., greater than 1.0 MPa) cases, the furthest distance could be around only 50 meters, very close to the HF.

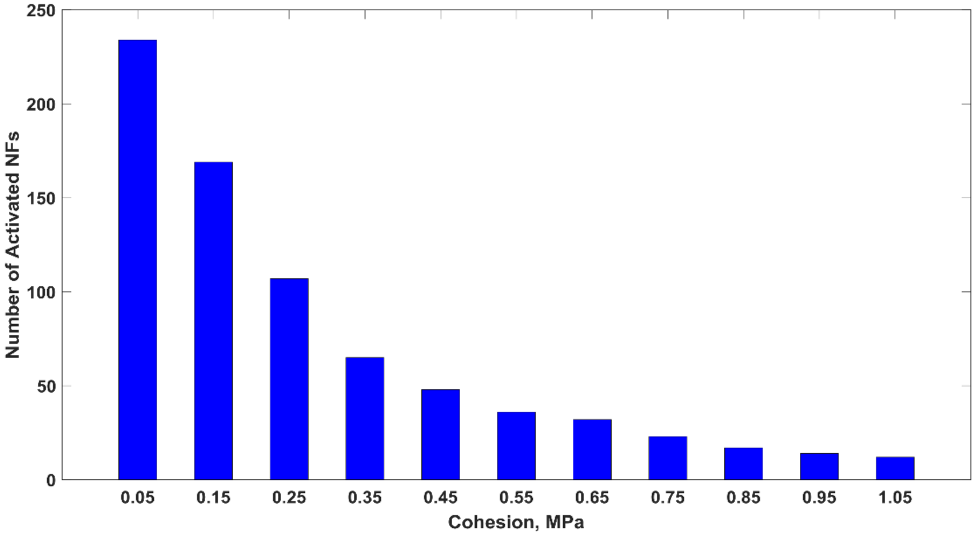

Figure 6.10 The number of activated NFs in the models with different cohesion. The number of the activated NFs decreases with cohesion exponentially.

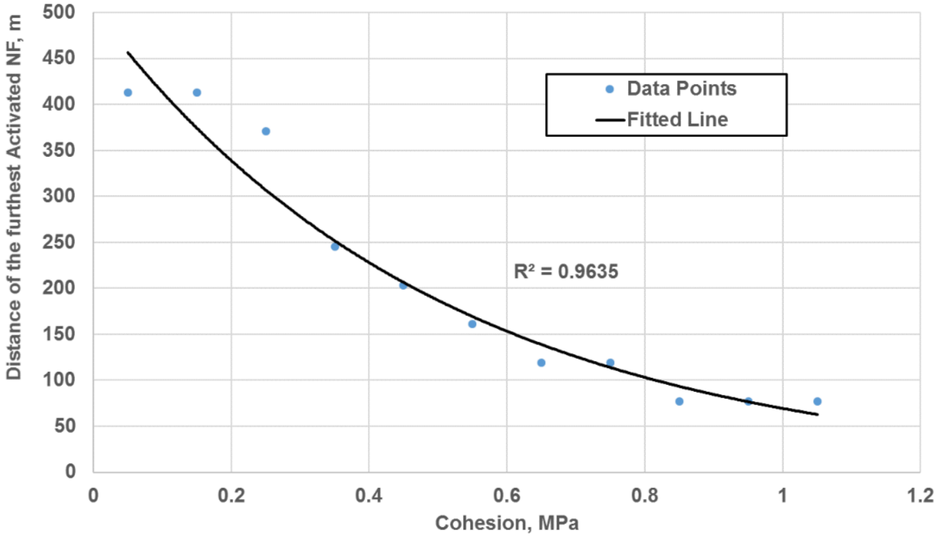

Figure 6.11 The distance of the furthest activated NF in the models with different cohesion. From the fitted or trend line, we can see the distance decreases with cohesion.

6.3.1.3 Rupture along the NFs

The rupture along the NFs in the model are not necessarily in the same pattern. They could be simple and complex as well. In Figure 6.12, we pick only four different representative patterns of rupture happening in the models, but there are more other patterns. The positions of the NFs are indicated in the titles of the subplots. In the upper left plot, the rupture initiates from the right side of the NF and propagates in a unilateral manner along the NF. The rupture speed is pretty uniform, and the average speed is about 1100 m/s, which is a subshear rupture, meaning the rupture speed is less than the S wave velocity. In the upper right plot, the rupture initiates from an inner location of the NF and propagates in a bilateral manner along the NF. Along each direction, the rupture propagates slowly first and then fast. For example, on the right side (from 15 to 35 meters), the rupture speed increases from 110 m/s to 650 m/s. In the lower left plot, the rupture is also bilateral. However, the rupture is complex on the right side (from 15 to 35 meters). The rupture first has a slow speed, then a fast speed and a slow speed at the end. In the lower right plot, the rupture first initiates from the right end, and propagates to the middle. Some time later, another rupture initiates from the left end, and propagates to the middle. And these two ruptures meet at around the center of the NF. Both ruptures are very slow.

In summary, the patterns of the rupture along the NFs are not necessarily the same in the models but could be quite different in both the speed and direction.

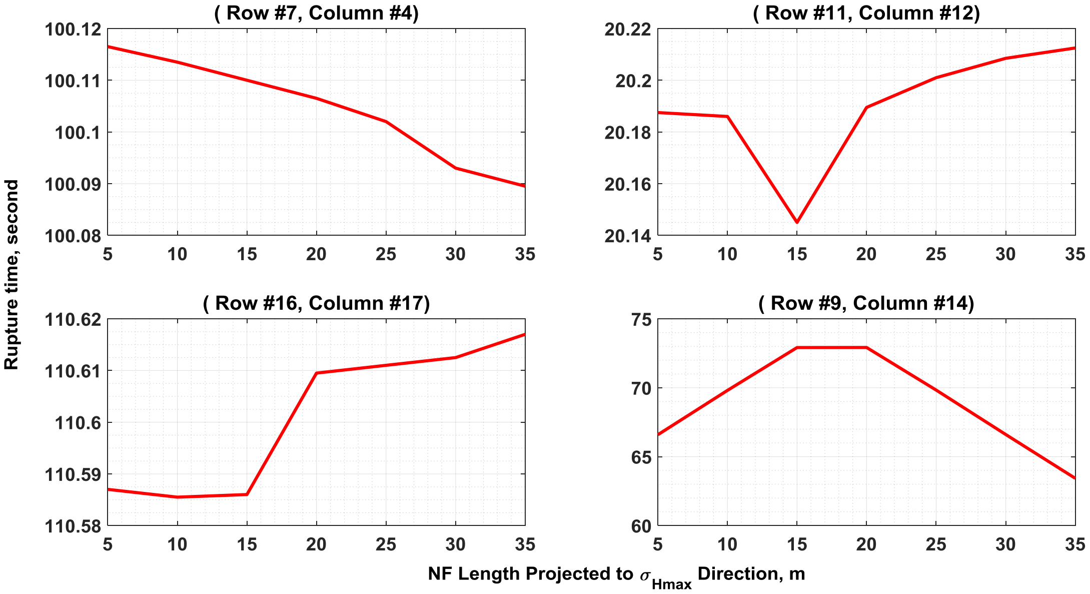

Figure 6.12 Rupture along the NFs in the models shows different patterns. The four patterns shown above indicate that the ruptures along the NFs could not be the same but quite different in both speed and direction.

6.3.1.4 Stresses and failure analysis

The dynamic stress perturbations in σ_{xx}, σ_{yy}, and σ_{xy} components around a propagating HF is shown in Figure 6.13. In the top two plots, stresses decay along the distance normal to the HF. The largest stress perturbations occur near the fracture surface and are compressive. Also, we can see that the tensile (negative) stress perturbations in σ_{xx}, and σ_{yy} occur around the fracture tip. The range of the stress perturbations on σ_{xx} component (i.e., the yellow oval in the top left plot) is much smaller than that of the stress perturbations on σ_{yy} (i.e., the bright yellow oval in the top right plot). This can be explained by Hook's law for an isotropic elastic solid (Please see the *section 3.3* in *Chapter 3*).

In Figure 6.13, the bottom plot shows the dynamic shear stress perturbations. We can see the largest induced shear stresses occur around the HF tips. On the two sides of the HF around the HF tips, the shear stresses have opposite sense.

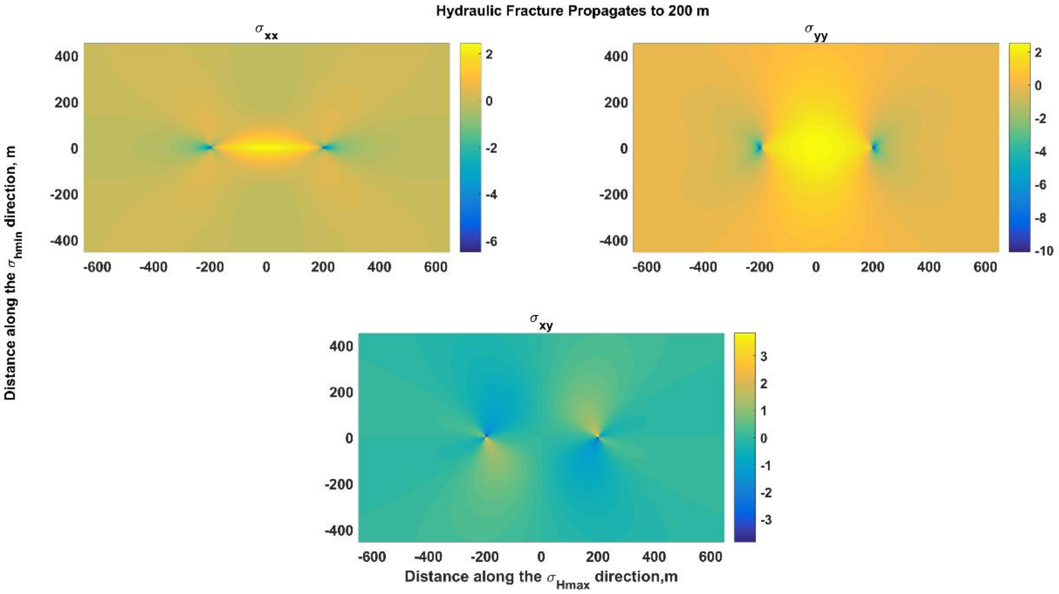

Figure 6.13 Dynamic stress perturbations around a propagating HF when it propagates to 200 meters.

We resolve the stress tensors at every location point onto a plane that is oriented N70W, which is same to the NF orientations and get the resolved shear stress and normal stress on the plane. We use a failure factor, ff, which is expressed as

$$ff = \frac{shear\ stress}{shear\ strength} \tag{6.1}$$

The higher the failure factor is, the lower the stability is. The stability map around a propagating HF when it propagates to 200 meters is shown in Figure 6.14. The yellow warm colors and large numbers are associated with unstable areas in the reservoir and are likely places for microseismicity to occur. We can see that the most unstable areas are around the HF tips and growing radially forward. The region normal to the HF has blue cool colors and they are stable. This verifies the conclusions of Warpinski et al. (2013) and the non leakoff case in Agarwal et al. (2012). In addition, the figure also shows that the stability is anti-symmetric about the wellbore. The two most stable (deep blue) regions are some distance away from the HF. The two unstable regions around one-wing of the HF are not equal in size and asymmetric. For example, on the right-wing side, the unstable region above is a little larger than below.

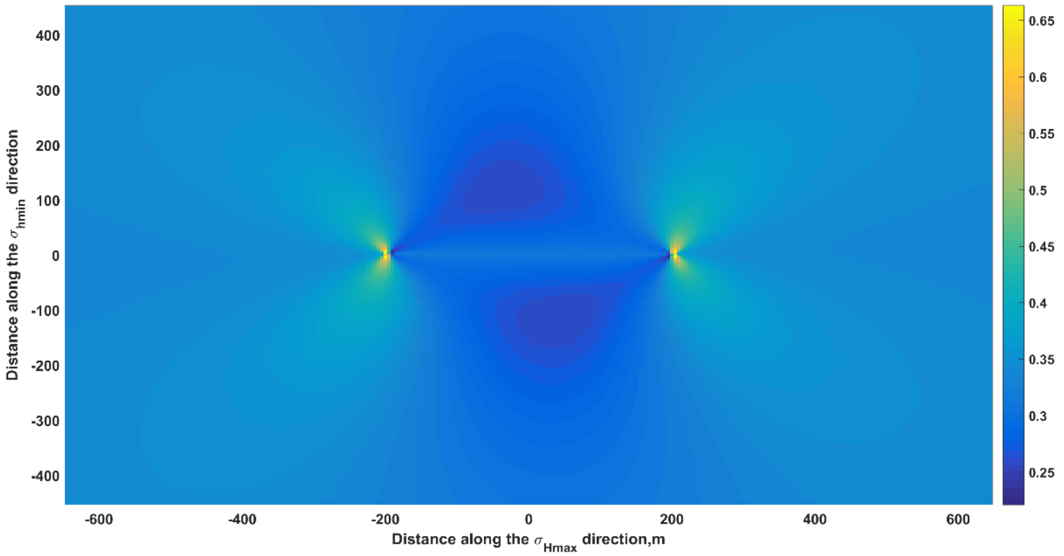

Figure 6.14 Stability map around a propagating HF when it propagates to 200 meters. The region normal to the HF is stable, where microseismicity is unlikely to be induced. The tip region is unstable, where microseismicity is likely to be induced.

6.3.2 Maximum horizontal principal directions: N88.2E, N83.4E, N79E, N71.3E, N68E, N65E, and N53.7E (i.e., the NF slopes are -0.4, -0.5, -0.6, -0.8, -0.9, -1.0, and -1.5, respectively)

Other scenarios with different directions of maximum horizontal principal stress are also studied. The investigated maximum horizontal principal directions include N88.2E, N83.4E, N79E, N71.3E, N68E, N65E, and N53.7E. The corresponding NF slopes, k in the models are -0.4, -0.5, -0.6, -0.8, -0.9, -1.0, and -1.5, respectively. The patterns of the MS events distribution in different scenarios are similar other than the exact values of the MS cloud length and strike (No NFs are activated in the scenario when the maximum horizontal principal direction is N53.7E (i.e., $k = -1.5$)). Here we just show one plot of the activated NFs when maximum horizontal principal direction is N88.2E (i.e., $k = -0.4$) and the HF propagates to 200 meters as an example. The plot is shown in Figure 6.15.

In Figure 6.15, after PCA analysis of the long-axis of the MS cloud envelope, we determined that the MS cloud length is 285 meters, the ratio between the MS cloud half-length and the HF half-length is 1.43, and the strike difference between the MS cloud long-axis and the HF is about 10.4^{o}. These parameter values from all the different scenarios are summarized and listed in Table 6.3. Compared with the scenario when maximum horizontal principal direction is N75E (i.e., $k = -0.7$), the interpreted length from the MS cloud is better. However, the interpreted strike is worse because the four 'branches' (i.e., zones of the activated NFs) are more asymmetric. From Table 6.3, we conclude that when the NF slope is -0.6 ~ -0.8, the MS cloud has large discrepancy with the HF in length but small discrepancy in strike. When the NF slope is at the two ends (-0.4 ~ -0.5 and -0.9 ~ -1.0), the MS cloud has small discrepancy with the HF in length but large discrepancy in strike.

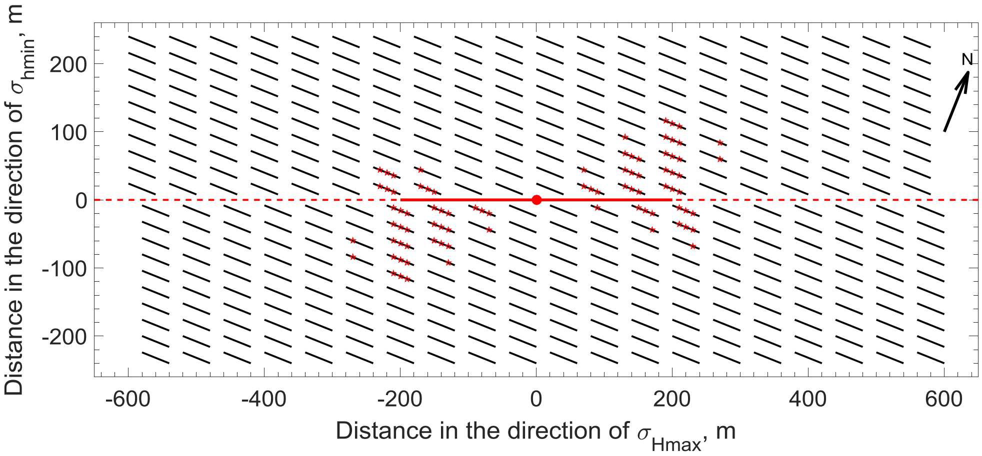

Figure 6.15 MS events/activated NFs in the model when k = -0.4 and x_f = 200 meters. k is the slope of the inclined NFs. x_f is the half-length of the HF. Small red-star markers on a NF indicate the NF is activated. If there are three red-star markers on a NF, it means the NF is entirely activated. If there are fewer than three red-star markers but at least one on a NF, it means the NF is partially activated.

Table 6.3 Correlation between the MS Cloud and the HF when x_f = 200 m

NF slope	MS cloud half-length (l), m	l/x_f	Strike difference, °
-0.4	285	1.43	10.4
-0.5	303	1.52	11.3
-0.6	354	1.77	7.0
-0.7	481	2.41	3.5
-0.8	444	2.22	6.8
-0.9	383	1.92	8.9
-1.0	325	1.63	11.7

The number of activated NFs in the models with different σ_{Hmax} directions are plotted in Figure 6.16. When the NF slope is -0.7 (i.e., the σ_{Hmax} direction is N75E), There are the most activated NFs, about 65 NFs are activated. And the bars are in a parabolic shape, and the peak occurs around -0.7. The distance of the furthest activated NF in the models with different σ_{Hmax} directions are shown in Figure 6.17. A trend line is fitted to the data points. The largest distance, which could be up to 250 meters, also occurs around -0.7.

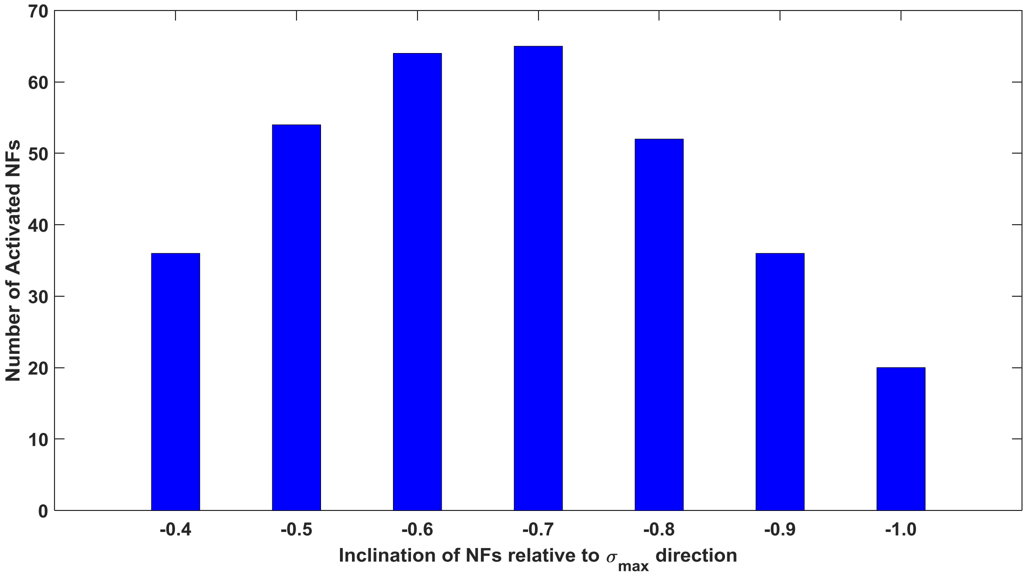

Figure 6.16 The number of activated NFs in the models with different σ_{Hmax} directions. The heights of the bars are in a parabolic shape.

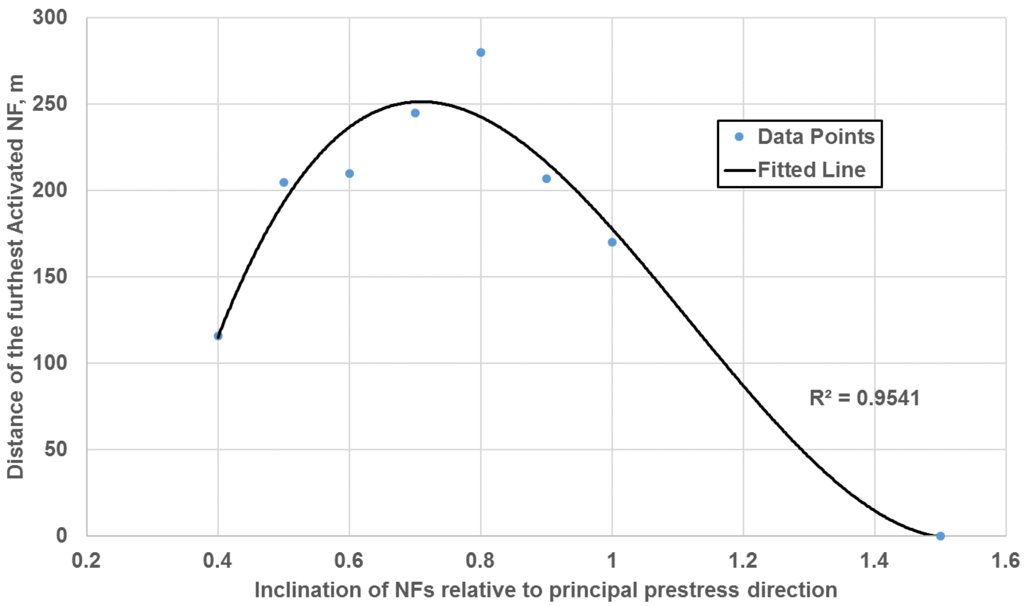

Figure 6.17 The distance of the furthest activated NF in the models with different σ_{Hmax} directions. The fitted or trend curve has the peak value at around 0.7 (i.e., -0.7 scenario, absolute values are used in this plot).

6.4 Discussion

Comparing different scenarios with different maximum horizontal principal directions, we find that when the maximum horizontal principal direction is N75E (i.e., k = -0.7), the most NFs are activated, and the distance of the furthest activated NF is the largest among all the scenarios. When k = -0.7, the NFs are more easily activated. From a geomechanics point of view, there exists an optimal angle for frictional sliding. And the optimal angle can be calculated as

$$\beta = \frac{\pi}{4} + \frac{1}{2} tan^{-1}\mu \tag{6.2}$$

Where β is the angle between maximum principal pre-stress S1 and a weak plane normal, and μ is the frictional coefficient. By using this equation, we can get $\beta = \frac{\pi}{4} + \frac{1}{2} tan^{-1}(0.35) = 0.3036$ (rad). Therefore, the optimal inclination slope (OIS) is

$$\mathrm{OIS} = \pm \tan\left(\frac{\pi}{2} - \beta\right) = \pm 0.71 \tag{6.3}$$

On the Mohr circle as shown in Figure 6.18, every set of inclined NFs of a certain inclination corresponds to a stress state. And we can see the NFs with inclination slope of -0.7 are the nearly optimal-inclination NFs, meaning the closest to failure. Therefore, these NFs are most easily activated, and many MS events would be triggered. NFs with an inclination slopes of -0.4 (low-inclination NFs) and -1.5 (high-inclination NFs) are far from the optimal stress state and more dynamic stress perturbations are needed to activate them, so fewer or even no MS events are induced.

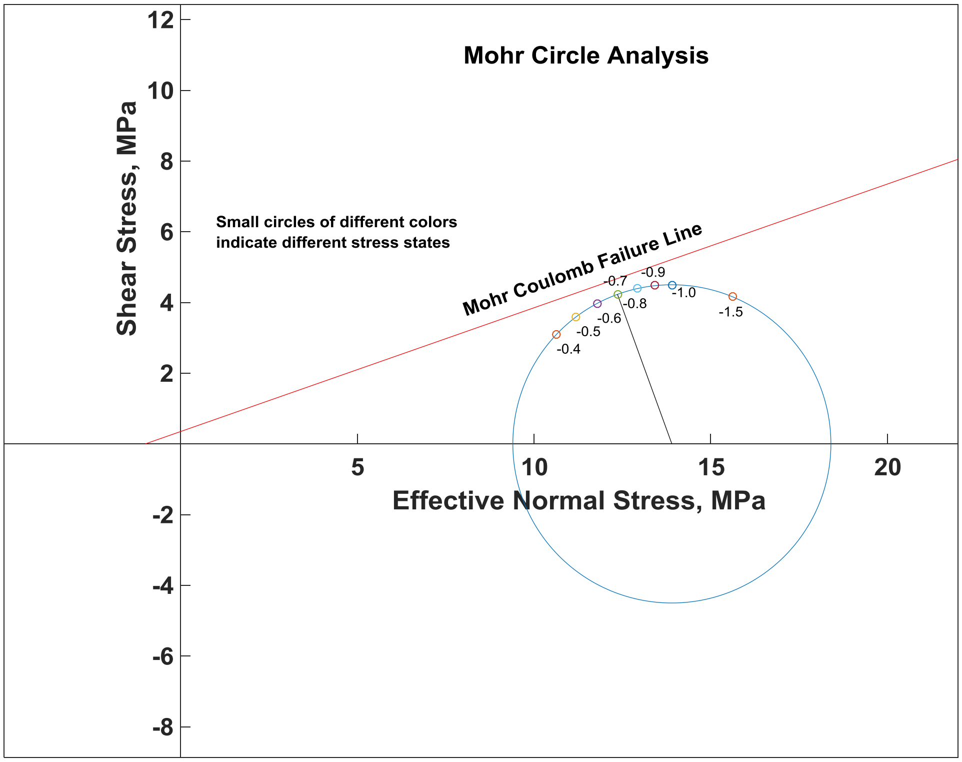

Figure 6.18 Mohr circle analysis. Different stress states (i.e., small circles on the Mohr circle) have different distances away from the Mohr Coulombe Failure Line. The stress state when the NF slope is -0.7 is the closest to the failure line.

As mentioned above, when the NF inclination slope is around the OIS (e.g., -0.6 ~ -0.7), the NFs are easily activated. The four branches (i.e., zones of the activated NFs) around the HF are not significantly different in numbers of activated NFs and almost symmetric about the HF, which lessens the strike difference. However, when the NF inclination slope is far from the OIS (e.g., -0.4 ~ -0.5 or -0.9 ~ -1.0), the NFs are hard to activate. On the side of one wing of the HF, the two branches would be quite different in numbers of activated NFs and asymmetric about the HF (e.g., Figure 6.15), which increases the strike difference.

In some other research of the Barnett shale, smaller horizontal stress anisotropy is used than that in our model. Kresse et al. (2013) used a low horizontal stress anisotropy in their Barnett fracture simulations. Vermylen et al. (2011) determined a small difference between the maximum and minimum horizontal stress gradients (S_{Hmax} = 0.73 psi/ft, and S_{hmin} = 0.65 psi/ft) by investigating five horizontal wells, whose horizontal sections are at a depth between 5700-5750 feet. A low horizontal stress anisotropy will shrink the Mohr circle, and make the NFs harder to be activated. However, the Barnett Shale is regarded as overpressured with a pressure gradient approximately at 0.52 psi/ft (Bowker 2007 and Tian 2010). The overpressure could move the Mohr circle to the left (compression is assumed to be positive) and make the NFs easier to be activated. Ketter et al. (2008) presented stress heterogeneity in the Barnett Shale. Locally, in some compartments of the Barnett shale, the horizontal stress anisotropy could be large, which might make the activation of the NFs easier.

6.5 Conclusions

Our in-house dynamic geomechanics finite element code is applied to study the MS cloud induced by hydraulic fracturing based on Barnett Shale gas reservoir properties and we achieve the conclusions below:

1. When a HF propagates to a longer length, more MS events would be triggered and the distance of the furthest activated NF normal to the HF becomes larger. The induced MS cloud length increases. The ratio between the MS cloud half-length and HF half-length increases.
2. The number of the activated NFs and the distance of the furthest activated NF normal to the HF decrease exponentially with cohesion.

3. The patterns of the rupture along the NFs are not necessarily the same but could be quite different in both the speed and direction.
4. Without considering leakoff, the area normal to the HF surface is stable, and microseisms seldom occur in the area. The tip region is unstable, and microseisms would be likely to be induced.
5. When the inclination of the NFs relative to the maximum horizontal principal direction is nearly optimal, many MS events would be generated and spread far away from the HF but are almost symmetric about the HF. The MS cloud has large discrepancy with the HF in length but small discrepancy in strike.
6. When the inclination of the NFs relative to the maximum horizontal principal direction is either high or low, not so many MS events would be generated, and they could be close to the HF but quite asymmetric about the HF. The MS cloud has small discrepancy with the HF in length but large discrepancy in strike.

CHAPTER VII

SUMMARY AND CONCLUSIONS

Hydraulic fracturing and microseismicity generation and radiation are dynamic processes. The associated dynamic stress perturbations could play a significant role in relevant studies, such as activation of weak planes including NFs, and bedding planes, etc. We apply our in-house dynamic FEM geomechanics code to work on microseismic-related questions.

First, we investigate the significance of the dynamic stress perturbations by studying how different the dynamic and static stress perturbations could be during hydraulic fracturing. The static stress perturbations are obtained when the models reach static equilibrium (i.e., after generated seismic waves die out). We compare the static and dynamic stress perturbations at a moment when a HF propagates to a certain length. Mohr circle analysis shows that around the HF the Mohr circle based on a dynamic stress tensor is closer to a failure line than that based on a static stress tensor. The peak static and dynamic stress perturbations during the process are also compared. We determine that the absolute values of the peak dynamic stress perturbations are always greater than those of the peak static stress perturbations, especially in the area close to the HF and its tips. The effect of injection rates on the static and dynamic stress perturbations also is studied. The largest peak static and dynamic stress perturbations during the hydraulic fracturing process are measured. The absolute values of both the largest peak dynamic and static stress perturbations increase with injection rates. The absolute values of the difference between the largest peak dynamic and static stress perturbations also increase with injection rates due to more significant dynamic effects.

Second, we apply our code to examine the induced dynamic shear stress and the activation of horizontal BPs based on Cotton Valley tight-sand reservoir properties. Whether the tip stresses around a dynamically propagating HF could activate a bedding plane is an important question for HF propagation and microseismicity generation. Some specific patterns of MS events (dip-slip or strike-slip events) could be induced. A BP perpendicular to a principal direction is unlikely to be activated using a simple geomechanical model. However, the induced dynamic stresses around a HF tip could be significant. We set up three different scenarios to study the BP activation. In the first scenario, a HF is dynamically propagating towards two symmetric BPs, but has not touched them yet. In the second scenario, a HF dynamically propagates towards two symmetric BPs, and then crosses them by a short distance. In the third scenario, a HF dynamically propagates towards two symmetric BPs, and then fluid invasion to the BPs occurs after the HF deflects into them. BPs could be activated under dynamic stress conditions and the slip may induce the microseismic events. The shear slippage and open width along the BPs are calculated and quantified in our models. We find that only low-strength BPs can be activated in the first scenario. The effect of different model parameters such as cohesion, critical slip distance, rock density and vertical stress on the activation of the BPs is investigated in the second scenario. Large shear slippage and slip length happen in the third scenario with fluid invasion weakening the BPs. Different senses of shear could occur along the BPs. The rupture initiates at around the center of a BP and then propagates bilaterally.

Third, we perform analysis on the fracture dynamic interaction and the predominant frequency of the induced microseismic signals during hydraulic fracturing. The slip distributions and the ruptures along the activated NFs in the models with different cohesion are studied. We find that some activated NFs could have partial failure while others could fail entirely. The ruptures could be either unilateral or bilateral and the speeds may vary. The NFs and the HF can interact with each other. Different patterns of MS signals could be induced by different sources. The effects of model parameters such as injection rate and Young's modulus on the predominant frequency of the MS signals are investigated. We find that injection rate doesn't affect the predominant frequencies much and a higher Young's modulus could shift the predominant frequencies higher. Rupture patterns (i.e., directionality and speed) along the NFs could affect the spectrum of the induced MS signals. The spectrum could either have multiple predominant frequencies or be relatively flat over the investigated frequency range.

Fourth, the correlation between the geometry (i.e., orientation and length) of the HF and the MS cloud induced by hydraulic fracturing is determined. We work in a 2D framework and use a uniformly fractured shale reservoir as an example. The NF direction, length and spacing are similar to those in the Barnett Shale. Effects of HF length and cohesion on the correlation are studied. Some examples of the rupture patterns along the NFs are presented. The stability around a dynamically propagating HF is also determined. The area normal to the HF surface is stable, and microseisms seldom occur in this area. The tip region is unstable, and microseisms would be likely to be induced here. The inclination of the NFs relative to the maximum horizontal principal direction also affects the correlation. When the NF inclination is nearly optimal, meaning close to failure, many MS events would be generated, and spread far away from the HF but the symmetry about the HF is good. The correlation between the strikes of the HF and the MS cloud long-axis remains good but the correlation between their lengths is poor. However, when the NF inclination is either high or low, not so many MS events would be generated, and they could be close to the HF but the asymmetry about the HF is more apparent. The correlation between the lengths of the HF and the MS cloud long-axis is good but the correlation between their strikes is poor.

REFERENCES

Agarwal, K., Mayerhofer, M.J. and Warpinski, N.R., 2012. Impact of geomechanics on microseismicity. SPE/EAGE European Unconventional Resources Conference & Exhibition-From Potential to Production.

Akulich, A., and Zvyagin, A. 2008. Interaction between hydraulic and natural fractures. *Fluid dynamics* 43(3): 428-435.

Andrews, D. 1976. Rupture velocity of plane strain shear cracks. *Journal of Geophysical Research* 81(32): 5679-5687.

Anikiev, D., Valenta, J., Stanek, F., and Eisner, L. 2014. Joint location and source mechanism inversion of microseismic events: Benchmarking on seismicity induced by hydraulic fracturing. *Geophysical Journal International* 198(1): 249-258.

Bahorich, B., Olson, J. E., and Holder, J. 2012. Examining the effect of cemented natural fractures on hydraulic fracture propagation in hydrostone block experiments. Presented at SPE Annual Technical Conference and Exhibition, San Antonio, Texas, 8-10 October. SPE-160197-MS.

Baig, A., Urbancic, T., 2010. Microseismic moment tensors: A path to understanding frac growth. The Leading Edge. 29, 320-324.

Baisch, S. and Harjes, H-P., 2003. A model for fluid-injection-induced seismicity at the KTB, Germany. Geophysical Journal International, 152(1), 160-170.

Bazan, L. W., 2011. Advanced Completion Design, Fracture Modeling Technologies Optimize Eagle Ford Performance. The American Oil and Gas Reporter.

Beugelsdijk, L., De Pater, C., and Sato, K. 2000. Experimental hydraulic fracture propagation in a multi-fractured medium. Presented at SPE Asia Pacific conference on integrated modelling for asset management, Yokohama, Japan, 25–26 April. SPE-59419-MS.

Blanton, T. L. 1986. Propagation of hydraulically and dynamically induced fractures in naturally fractured reservoirs. Presented at SPE unconventional gas technology symposium, Louisville, Kentucky, 18-21 May. SPE-15261-MS.

Bowker, K.A., 2007. Barnett shale gas production, Fort Worth Basin: Issues and discussion. AAPG bulletin, 91(4), 523-533.

Cooke, M. L., and Underwood, C. A., 2001. Fracture termination and step-over at bedding interfaces due to frictional slip and interface opening. Journal of Structural Geology. 23, 223-238.

Chuprakov, D., Melchaeva, O., and Prioul, R. 2013. Hydraulic fracture propagation across a weak discontinuity controlled by fluid injection. Effective and sustainable hydraulic fracturing, InTech.

Chuprakov, D. A., and Prioul, R. 2015, Hydraulic fracture height containment by weak horizontal interfaces: SPE Hydraulic Fracturing Technology Conference, Society of Petroleum Engineers.

Cooke, M. L., and Underwood, C. A. 2001. Fracture termination and step-over at bedding interfaces due to frictional slip and interface opening: Journal of Structural Geology, 23, 223-238.

Cramer, D. D., 1992. Treating-pressure analysis in the Bakken formation. Journal of Petroleum Technology. 44, 20-27.

Dahi-Taleghani, A., and Olson, J. E. 2011. Numerical modeling of multistranded-hydraulic-fracture propagation: Accounting for the interaction between induced and natural fractures. *SPE Journal* 16(03): 575-581.

Day, S. M., Dalguer, L. A., Lapusta, N., and Liu, Y., 2005. Comparison of finite difference and boundary integral solutions to three-dimensional spontaneous rupture. Journal of Geophysical Research: Solid Earth. 110, 1-23.

Diller, D. E., Shuck, T. and Fish, B. 2015. Estimation and interpretation of high-confidence microseismic source mechanisms: The Leading Edge, 34, 918-924.

Duan, B., 2010. Role of initial stress rotations in rupture dynamics and ground motion: A case study with implications for the Wenchuan earthquake, J. Geophys. Res., 115, B05301.

Duan, B., 2012. Dynamic rupture of the 2011 Mw 9.0 Tohoku-Oki earthquake: Roles of a possible subducting seamount, J. Geophys. Res., 117, B05311.

Duan, B. 2016. Spontaneous rupture on natural fractures and seismic radiation during hydraulic fracturing treatments. *Geophysical Research Letters* 43(14): 7451-7458.

Duan, B., and Oglesby, D. D. 2006. Heterogeneous fault stresses from previous earthquakes and the effect on dynamics of parallel strike-slip faults, *J. Geophys. Res.*, 111, B05309.

Duan, B., and Day, S. M. 2008. Inelastic strain distribution and seismic radiation from rupture of a fault kink, *J. Geophys. Res.*, 113, B12311.

Duchkov, A., and Stefanov, Y. P., 2015. Analysis of seismic sources for different mechanisms of fracture growth for microseismic monitoring applications. AIP Conference Proceedings, AIP Publishing.

Evans, K.F., Moriya, H., Niitsuma, H., Jones, R.H., Phillips, W.S., Genter, A., Sausse, J., Jung, R., and Baria, R., 2005. Microseismicity and permeability enhancement of hydrogeologic structures during massive fluid injections into granite at 3 km depth at the Soultz HDR site. *Geophysical Journal International*, 160(1), 388-412.

Fischer, T., Bouskova, A., Eisner, L., and Le Calvez, J., 2007. Automated P-and S-Wave Picking of Micro Earthquakes Re-Corded by a Vertical Array. 69th EAGE Conference and Exhibition incorporating SPE EUROPEC 2007.

Fischer, T., Hainzl, S., Eisner, L., Shapiro, S.A., and Le Calvez, J., 2008. Microseismic signatures of hydraulic fracture growth in sediment formations: Observations and modeling. *Journal of Geophysical Research: Solid Earth*, 113(B2),1-12.

Gale, J. F., Reed, R. M., and Holder, J. 2007. Natural fractures in the Barnett Shale and their importance for hydraulic fracture treatments. *AAPG bulletin* 91(4): 603-622.

Gaucher, E., 2012. Microseismic monitoring of geothermal fields: more than a traffic light system. International Geothermal Conferenz.

Gibowicz, S.J. and Kijko, A., 2013. An introduction to mining seismology, Elsevier.

Gischig, V. S., 2015. Rupture propagation behavior and the largest possible earthquake induced by fluid injection into deep reservoirs: *Geophysical Research Letters* 42, 7420-7428.

Gottschling, J. C., 2010. Marcellus net fracturing pressure analysis. SPE Eastern Regional Meeting, Society of Petroleum Engineers.

Green, A., and Sneddon, I., 1950. The distribution of stress in the neighbourhood of a flat elliptical crack in an elastic solid. Mathematical Proceedings of the Cambridge Philosophical Society, Cambridge Univ Press.

Gu, H. and Weng, X. 2010. Criterion for fractures crossing frictional interfaces at non-orthogonal angles. Presented at 44th US rock mechanics symposium and 5th US-Canada rock mechanics symposium, Salt Lake City, Utah, 27–30 June. ARMA 10-198

Gutierrez Murillo, G., Sanchez, A., Rios, A., and Arguello, L., 2010. Microseismic HF monitoring to determine the fracture geometry in Coyotes field, Chicontepec. SPE Latin American and Caribbean Petroleum Engineering Conference, Society of Petroleum Engineers.

Häring, M.O., Schanz, U., Ladner, F., and Dyer, B.C., 2008. Characterisation of the Basel 1 enhanced geothermal system. *Geothermics*, 37(5), 469-495.

Harris, R. A., and Day S. M., 1993. Dynamics of fault interaction: Parallel strike-slip faults. *Journal of Geophysical Research: Solid Earth* 98(B3): 4461-4472.

Harris, R. A., Barall, M., Archuleta, R., et al. 2009. The SCEC/USGS dynamic earthquake rupture code verification exercise, *Seismol. Res. Lett.*, 80(1), 119–126, doi:10.1785/ gssrl.80.1.119.

Harris, R. A., Barall, M., Andrews, D.J., et al. 2011. Verifying a computational method for predicting extreme ground motion, *Seismol. Res. Lett.*, 82(5), 638-644, doi:10.1785/gssrl.85.5.638.

Harris, R. A., Barall, M., Aagaard, B., et al. 2018. A suite of exercises for verifying dynamic earthquake rupture codes, Seismol. Res. Lett., 89, 1146-1162.

House, L., 1987. Locating microearthquakes induced by hydraulic fracturing in crystalline rock. *Geophysical Research Letters*, 14(9), 919-921.

Hu, H., Li, A., and Zavala-Torres, R. 2017. Long-period long-duration seismic events during hydraulic fracturing: implications for tensile fracture development. *Geophysical Research Letters* 44(10): 4814-4819.

Jiang, H., Chen, Z., Zeng, X., Lv, H., and Liu, X. 2016. Velocity calibration for microseismic event location using surface data. *Petroleum Science* 13(2): 225-236.

Kim, J., Woo, J., Rhie, J., and Kang, T. 2017. Automatic determination of first-motion polarity and its application to focal mechanism analysis of microseismic events. *Geosciences Journal* **21**(5): 695-702.

Kohli, A. H. and Zoback, M. D. 2013. Frictional properties of shale reservoir rocks. *Journal of Geophysical Research: Solid Earth* 118(9): 5109-5125.

Kresse, O., Weng, X., Chuprakov, D., Prioul, R., and Cohen, C., 2013. Effect of flow rate and viscosity on complex fracture development in UFM model. Effective and sustainable hydraulic fracturing, InTech, 183-210.

Kuang, W., Zoback, M., and Zhang, J. 2016. Estimating geomechanical parameters from microseismic plane focal mechanisms recorded during multistage hydraulic fracturing. *Geophysics* 82(1): KS1-KS11.

Lancaster, D., McKetta, S.F., Hill, R.E., Guidry, F.K., and Jochen, J.E., 1992. Reservoir evaluation, completion techniques, and recent results from Barnett Shale development in the Fort Worth Basin. SPE Annual Technical Conference and Exhibition, Society of Petroleum Engineers.

Le Calvez, J. H., Craven, M. E., Klem, R. C., Baihly, J. D., Bennett, L. A., and Brook, K., 2007. Real-time microseismic monitoring of HF treatment: a tool to improve completion and reservoir management. SPE Hydraulic Fracturing Technology Conference, Society of Petroleum Engineers.

Li, J., Kuleli, H. S., Zhang, H., and Toksoz, M. N. 2011. Focal mechanism determination of induced microearthquakes in an oil field using full waveforms from shallow and deep seismic networks Determining focal mechanism by waveforms. *Geophysics* 76(6): WC87-WC101.

Liu, S., Valko, P.P., McKetta, S., and Liu, X., 2016. Microseismic Closure Window Characterizes Hydraulic-Fracture Geometry Better. SPE Reservoir Evaluation & Engineering. 20, 423-445.

Mahrer, K. D., and Mauk, F. J., 1987. Seismic wave motion for a new model of HF with an induced low-velocity zone. Journal of Geophysical Research: Solid Earth. 92, 9293-9309.

Martin, K. 2016. *https://www.quora.com/Seismology-What-is-the-frequency-in-Hz-of-an-earthquakes-p-wave*.

Mavko, G. 2005. Conceptual overview of rock and fluid factors that impact seismic velocity and impedance.

Maxwell, S.C., 2011. Microseismic hydraulic fracture imaging: The path toward optimizing shale gas production. The Leading Edge, 30, 340-346.

Maxwell, S. 2014. Microseismic Imaging of Hydraulic Fracturing: Improved Engineering of Unconventional Shale Reservoirs, Society of Exploration Geophysicists.

Maxwell, S. C. and Cipolla, C. L. 2011. What does microseismicity tell us about hydraulic fracturing? Presented at SPE Annual Technical Conference and Exhibition, Denver, Colorado, USA, 30 October–2 November. SPE-146932-MS.

Maxwell, S.C., Rutledge, J., Jones, R., and Fehler, M., 2010. Petroleum reservoir characterization using downhole microseismic monitoring. Geophysics, 75, 75A129-175A137.

Maxwell, S.C., Underhill, W., Bennett, L., Woerpel, C., and Martinez, A., 2010. Key criteria for a successful microseismic project. SPE Annual Technical Conference and Exhibition, Society of Petroleum Engineers.

McGillivray, P., 2005. Microseismic and time-lapse seismic monitoring of a heavy oil extraction process at Peace River, Canada. CSEG Recorder, 30(1), 5-9.

Michaud, G., Leaney, S., 2008. Continuous microseismic mapping for real-time event detection and location. SEG Technical Program Expanded Abstracts 2008, Society of Exploration Geophysicists. 1357-1361.

Olson, J. E. and Wu, K. 2012. Sequential vs. simultaneous multizone fracturing in horizontal wells: insights from a non-planar, multifrac numerical model. Presented at SPE Hydraulic Fracturing Technology Conference, The Woodlands, Texas, USA, 6–8 February. SPE-152602-MS.

Oye, V., Langet, N., Hasting, M., Lecomte, I., Messeiller, M., and Reid, P. 2012. Microseismic monitoring of the hydraulic stimulation at the Paralana enhanced geothermal system, South Australia: first break 30, 91-95.

Phillips, W., Fairbanks, T.D., Rutledge, J.T., and Anderson, D.W., 1998. Induced microearthquake patterns and oil-producing fracture systems in the Austin chalk. Tectonophysics, 289(1), 153-169.

Press, F., 2004, Understanding earth: Macmillan.

Puyang, P., 2012. Post-treatment assessment of hydraulic fracturing with integrated modeling of natural fracture distribution. Master thesis. Louisiana State University. US.

Renshaw, C. and Pollard, D. 1995. An experimentally verified criterion for propagation across unbounded frictional interfaces in brittle, linear elastic materials. *International journal of rock mechanics and mining sciences & geomechanics abstracts* 32(3): 237-249.

Reyes-Montes, J. M., Zhao., X., Chu, F., and Young, R. 2014. Analysis of Hydraulic Fracturing-induced Microseismic Event Location Using S-wave Polarization. 76th EAGE Conference and Exhibition 2014.

Roux, P.-F., 2016. Microseismic activity: What does it really say? Insights from Coulomb failure function analysis: Unconventional Resources Technology Conference (URTEC).

Rutledge, J., Downie, R., Maxwell, S., Drew, J., and Fischer, T., 2013. Extension-shear microseismic mechanisms during hydraulic fracturing. SEG Technical Program Expanded Abstracts 2013, Society of Exploration Geophysicists. 2067-2072.

Rutledge, J., Weng, X., Yu, X., Chapman, C., and Leaney, S. 2016, Bedding-plane slip as a microseismic source during hydraulic fracturing, SEG Technical Program Expanded Abstracts, 2555-2559.

Rutledge, J., Yu, X., and Leaney, S., 2015. Microseismic shearing driven by hydraulic-fracture opening: An interpretation of source-mechanism trends. The Leading Edge. 34, 926-934.

Ry, R. V., Septyana, T., Widiyantoro, S., Nugraha, A., and Ardjuna, A. 2017. Improved Location of Microseismic Events in Borehole Monitoring by Inclusion of Particle Motion Analysis: a Case Study at a CBM Field in Indonesia. IOP Conference Series: Earth and Environmental Science, IOP Publishing.

Scholz, C. H., 2002. The mechanics of earthquakes and faulting, Cambridge university press.

Shapiro, S., Dinske, C., and Rohert, E., 2006. Hydraulic-fracturing controlled dynamics of microseismic clouds. Geophysical Research Letters 33(14), 1-5.

Song, F., Kuleli, H. S., Toksoz, M. N., Ay, E., and Zhang, H. 2010. An improved method for hydrofracture-induced microseismic event detection and phase picking. *Geophysics* 75(6): A47-A52.

Stanek, F. and Eisner, L. 2013. New model explaining inverted source mechanisms of microseismic events induced by hydraulic fracturing. SEG Technical Program Expanded Abstracts 2013, Society of Exploration Geophysicists: 2201-2205.

Stanek, F. and Eisner, L. 2017, Seismicity Induced by Hydraulic Fracturing in Shales: A Bedding Plane Slip Model: Journal of Geophysical Research, 122, 7912-7926.

Tan, Y. and Engelder, T. 2016. Further testing of the bedding-plane-slip model for hydraulic-fracture opening using moment-tensor inversions Bedding-plane-slip model. Geophysics 81, KS159-KS168.

Tian, Y., 2010. An Investigation of Regional Variations of Barnett Shale Reservoir Properties, and Resulting Variability of Hydrocarbon Composition and Well Performance, Master thesis. Texas A&M University, College Station, United States.

Urbancic, T.I. and Trifu, C.I., 2000. Recent advances in seismic monitoring technology at Canadian mines. Journal of Applied Geophysics, 45(4), 225-237.

Valko, P., and Economides, M. J. 1995. Hydraulic fracture mechanics, Wiley Chichester.

Verdon, J.P., Kendall, J.M., White, D.J., Angus, D.A., Fisher, Q.J., and Urbancic, T., 2010. Passive seismic monitoring of carbon dioxide storage at Weyburn. The Leading Edge, 29, 200-206.

Vermylen, J.P., 2011. Geomechanical studies of the Barnett shale, Texas, USA, PhD thesis, Stanford University, CA, United States.

Wang, W. 2017. The effect of cemented natural fractures on hydraulic fracture propagation. Ph.D. dissertation, University of Texas at Austion.

Warpinski, N. R., 2000. Analytic crack solutions for tilt fields around hydraulic fractures. Journal of Geophysical Research: Solid Earth, 105(B10), 23463-23478.

Warpinski, N. R., 2009. Microseismic monitoring: Inside and out. Journal of Petroleum Technology, 61(11), 80-85.

Warpinski, N. R., and Teufel L. 1987. Influence of geologic discontinuities on hydraulic fracture propagation (includes associated papers 17011 and 17074). *Journal of Petroleum Technology* 39(02): 209-220.

Warpinski, N. R., Du, J., and Zimmer, U. 2012. Measurements of hydraulic-fracture-induced seismicity in gas shales. *SPE Production & Operations* 27(03): 240-252.

Warpinski, N. R., Mayerhofer, M., Agarwal, K., and Du, J. 2013. Hydraulic-fracture geomechanics and microseismic-source mechanisms. *SPE Journal* 18(04): 766-780.

Warpinski, N.R., Wolhart, S.L., and Wright, C.A., 2001. Analysis and prediction of microseismicity induced by hydraulic fracturing. SPE Annual Technical Conference and Exhibition, Society of Petroleum Engineers.

Wells, D. L. and Coppersmith, K. J. 1994. New empirical relationships among magnitude, rupture length, rupture width, rupture area, and surface displacement. Bulletin of the seismological Society of America 84, 974-1002.

Weng, X., Chuprakov, D., Kresse, O., Prioul, R., and Wang, H. 2018, Hydraulic fracture height containment by permeable weak bedding interfaces: Geophysics 83, 1-61.

Wu, K., and Olson J. E. 2014. Mechanics analysis of interaction between hydraulic and natural fractures in shale reservoirs, Presented at Unconventional Resources Technology Conference (URTEC), Denver, Colorado, USA, 25-27 August. URTec: 1922946.

Yang, X., Burghardt, J., Zhang, H. et al. 2016. Experimental Study of Hydraulic Fracture/Natural Fracture Interaction on a Tight Sandstone Formation, Presented at Unconventional Resources Technology Conference (URTEC), San Antonio, Texas, USA, 1-3 August. URTec: 2460449.

Zeng, X., Zhang, H., Zhang, X. et al. 2014. Surface Microseismic Monitoring of Hydraulic Fracturing of a Shale-Gas Reservoir Using Short-Period and Broadband Seismic Sensors. *Seismological Research Letters* 85(3): 668-677.

Zhang, F., Qiu, K., Yang, X. et al. 2015. A Study of the Interaction Mechanism between Hydraulic Fractures and Natural Fractures in the KS Tight Gas Reservoir. Presented at EUROPEC 2015, Madrid, Spain, 1–4 June. SPE-174384-MS.

Zhang, X. and Jeffrey, R. G. 2006. The role of friction and secondary flaws on deflection and re-initiation of hydraulic fractures at orthogonal pre-existing fractures. *Geophysical Journal International* 166(3): 1454-1465.

Zhang, Z., Rector, J. W., and Nava, M. J. 2015. Microseismic event location using multiple arrivals: Demonstration of uncertainty reduction. Unconventional Resources Technology Conference, San Antonio, Texas, 20-22 July 2015, Society of Exploration Geophysicists, American Association of Petroleum Geologists, Society of Petroleum Engineers.

Zoback, M. D., 2010, Reservoir geomechanics: Cambridge University Press.

APPENDIX

APPLICATION OF PRINCIPAL COMPONENT ANALYSIS/ALGORITHM (PCA) INTO DETERMINING THE STRIKE AND LENGTH OF THE MICROSEISMIC CLOUD ENVELOPE

As mentioned early in the text, PCA is mainly used for dimensionality reduction (high-dimensional data to low-dimensional data) to achieve data compression or data visualization. When 2-dimensional data is reduced to 1-dimensional data with PCA, PCA will find a direction (i.e., a vector $u \in R^2$) onto which to project the data to minimize the projection error. The projection error is defined as the summation of the distance from the 2D data points to a line with a direction. The direction determined from the PCA is used as the strike of the long-axis, and the length of the long-axis is from the line segment between the two most distant projection points. Details about the PCA will not be discussed here.

Here we give two examples about the long axis determined from PCA. Figure A-1 shows the MS cloud envelope when k = -0.7 and the HF propagates to 125 meters. The blue small circles are the data points used to determine the MS cloud envelope. The green dashed line is the line with the direction determined by PCA. The black dashed lines are the distances from the data points to the line. The summation of all these distances are the smallest among all the cases when these data points are projected to lines with different directions. In Figure A-1, we can see the four branches zones (i.e., collections of the activated NFs) are not significantly different in the number of the activated NFs, so the direction (or the strike) of the long axis is almost aligned with the HF strike, only 3-4^{o} difference. In Figure A-2, the MS cloud envelope when k = -0.4 and the HF propagates to 200 meters, the four branches zones are quite different, which causes the direction of the long axis more in ENE-WSW direction. The strike difference could be about 10°.

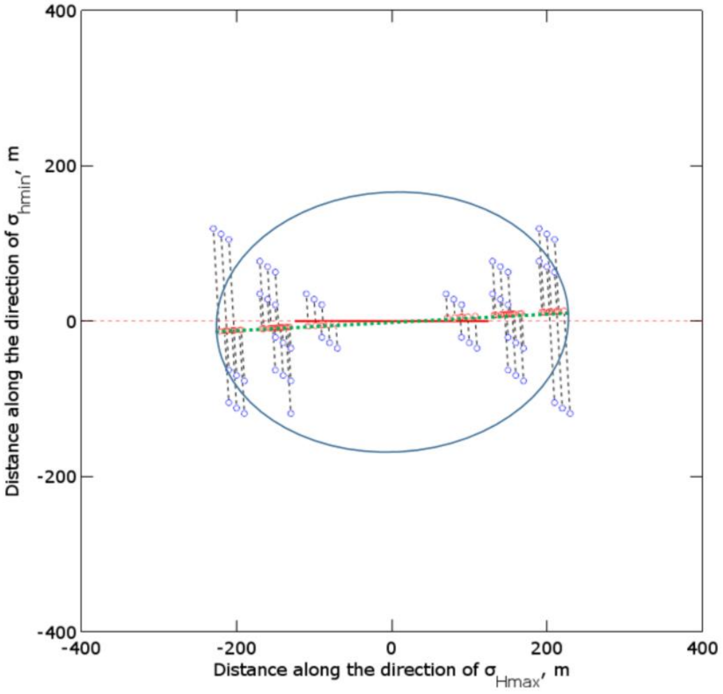

Figure A-1. MS Cloud envelope in the model when k = -0.7 and x_f = 125 meters. k is the slope of the inclined NFs. x_f is the half-length of the HF. The small blue circles are the data points from Figure 6.4. The green dashed line is the calculated long-axis of the MS cloud envelope by PCA. The small red circles (overlapped with the green dashed line) are the projection of the blue data points on the long-axis. The black dashed lines connecting the blue and red circles are the distances from the data points to the long-axis.

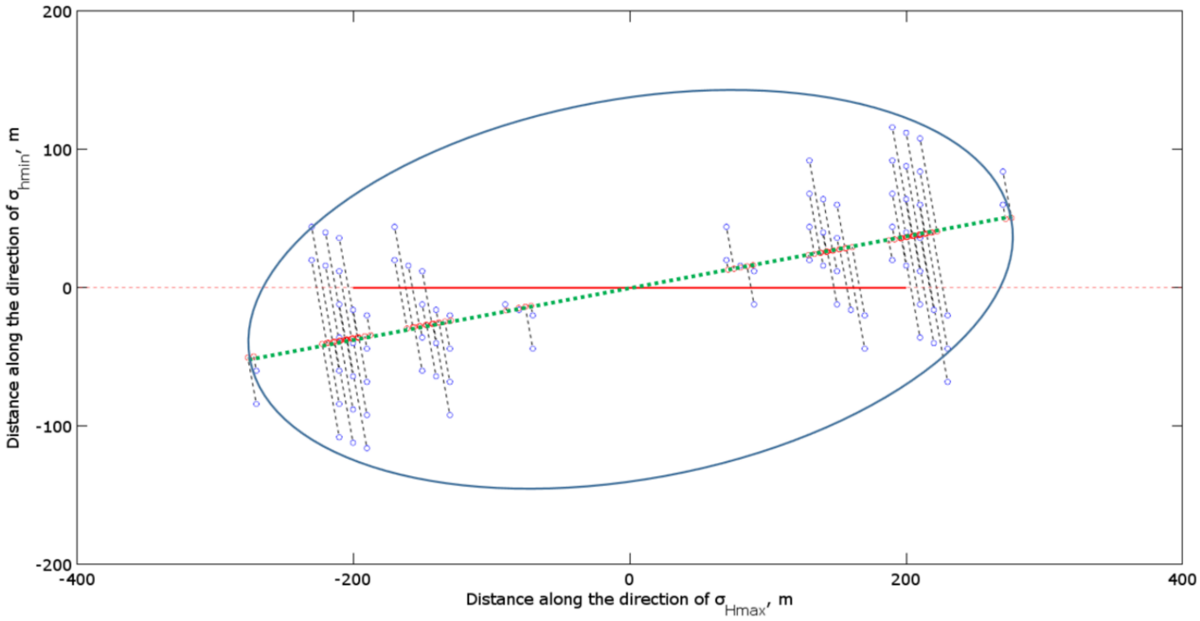

Figure A-2. MS Cloud in the model when k = -0.4 and x_f = 200 meters. k is the slope of the inclined NFs. x_f is the half-length of the HF. The small blue circles are the data points from Figure 6.15. The green dashed line is the calculated long-axis of the MS cloud envelope by PCA. The small red circles (overlapped with the green dashed line) are the projection of the blue data points on the long-axis. The black dashed lines connecting the blue and red circles are the distances from the data points to the long-axis.